

1 LEVERAGING MULTI-MESSENGER ASTROPHYSICS FOR DARK MATTER SEARCHES

By

Daniel Nicholas Salazar-Gallegos

A DISSERTATION

Submitted to  
Michigan State University  
in partial fulfillment of the requirements  
for the degree of

Physics—Doctor of Philosophy  
Computational Mathematics in Science and Engineering—Dual Major

Today

**ABSTRACT**

3 I did Dark Matter with HAWC and IceCube. I also used Graph Neural Networks

<sup>4</sup> Copyright by

<sup>5</sup> DANIEL NICHOLAS SALAZAR-GALLEGOS

<sup>6</sup> Today

## ACKNOWLEDGMENTS

8 I love my friends. Thanks to everyone that helped me figure this out. Amazing thanks to the people  
9 at LANL who supported me. Eames, etc Dinner Parties Jenny and her child Kaydince Kirsten, Pat,  
10 Andrea Family. You're so far but so critical to my formation. Unconditional love. Roommate

## TABLE OF CONTENTS

12	LIST OF TABLES . . . . .	vii
13	LIST OF FIGURES . . . . .	viii
14	LIST OF ABBREVIATIONS . . . . .	xiii
15	CHAPTER 1      INTRODUCTION . . . . .	1
16	CHAPTER 2      DARK MATTER IN THE COSMOS . . . . .	2
17	2.1 Introduction . . . . .	2
18	2.2 Dark Matter Basics . . . . .	3
19	2.3 Evidence for Dark Matter . . . . .	4
20	2.4 Searching for Dark Matter: Particle DM . . . . .	11
21	2.5 Sources for Indirect Dark Matter Searches . . . . .	16
22	2.6 Multi-Messenger Dark Matter . . . . .	18
23	CHAPTER 3      MULTIMESSENGER ASTROPHYSICS: DETECTING HIGH EN-	
24	ERGY NEUTRAL MESSENGERS . . . . .	21
25	3.1 Introduction . . . . .	21
26	3.2 Charged Particles in a Medium . . . . .	21
27	3.3 Photons ( $\gamma$ ) . . . . .	22
28	3.4 Neutrinos ( $\nu$ ) . . . . .	22
29	3.5 Opportunities to Combine for Dark Matter . . . . .	22
30	CHAPTER 4      HIGH ALTITUDE WATER CHERENKOV (HAWC) OBSERVATORY .	24
31	4.1 The Detector . . . . .	24
32	4.2 Events Reconstruction and Data Acquisition . . . . .	24
33	4.3 Remote Monitoring . . . . .	24
34	CHAPTER 5      ICECUBE NEUTRINO OBSERVATORY . . . . .	25
35	5.1 The Detector . . . . .	25
36	5.2 Events Reconstruction and Data Acquisition . . . . .	25
37	5.3 Northern Test Site . . . . .	25
38	CHAPTER 6      COMPUTATIONAL TECHNIQUES IN PARTICLE ASTROPHYSICS .	26
39	6.1 Neural Networks for Gamma/Hadron Separation . . . . .	26
40	6.2 Parallel Computing for Dark Matter Analyses . . . . .	26
41	CHAPTER 7      GLORY DUCK: MULTI-WAVELENGTH SEARCH FOR DARK MATT-	
42	TER ANNIHILATION TOWARDS DWARF SPHEROIDAL GALAX-	
43	IES . . . . .	27
44	7.1 Introduction . . . . .	27
45	7.2 Dataset and Background . . . . .	29
46	7.3 Analysis . . . . .	30

47	7.4	Likelihood Methods . . . . .	35
48	7.5	HAWC Results . . . . .	42
49	7.6	Glory Duck Combined Results . . . . .	42
50	7.7	HAWC Systematics . . . . .	47
51	7.8	<i>J</i> -factor distributions . . . . .	51
52	7.9	Discussion and Conclusions . . . . .	56
53	<b>CHAPTER 8</b>	<b>NU DUCK . . . . .</b>	<b>60</b>
54	<b>CHAPTER 9</b>	<b>MULTITHREADING HAWC ANALYSES FOR DARK MATTER</b>	
55		<b>SEARCHES . . . . .</b>	<b>61</b>
56	<b>APPENDIX A</b>	<b>MULTI-EXPERIMENT SUPPLEMENTARY FIGURES . . . . .</b>	<b>62</b>
57	<b>BIBLIOGRAPHY . . . . .</b>		<b>64</b>

## LIST OF TABLES

<p>59    Table 7.1    Summary of the relevant properties of the dSphs used in the present work.  60    Column 1 lists the dSphs. Columns 2 and 3 present their heliocentric distance  61    and galactic coordinates, respectively. Columns 4 and 5 report the <math>J</math>-factors of  62    each source given from the <math>\mathcal{GS}</math> and <math>\mathcal{B}</math> independent studies and their estimated  63    <math>\pm 1\sigma</math> uncertainties. The values <math>\log_{10} J</math> (<math>\mathcal{GS}</math> set) [44] correspond to the mean  64    <math>J</math>-factor values for a source extension truncated at the outermost observed star.  65    The values <math>\log_{10} J</math> (<math>\mathcal{B}</math> set) [46] are provided for a source extension at the tidal  66    radius of each dSph. <b>Bolded sources are within HAWC's field of view and</b>  67    <b>provided to the Glory Duck analysis.</b></p>	<p style="margin: 0;">. . . . . 35</p>
<p>68    Table 7.2    Summary of dSph observations by each experiment used in this work. A  69    ‘-’ indicates the experiment did not observe the dSph for this study. For  70    Fermi-LAT, the exposure at 1 GeV is given. For HAWC, <math> \Delta\theta </math> is the absolute  71    difference between the source declination and HAWC latitude. HAWC is more  72    sensitive to sources with smaller <math> \Delta\theta </math>. For IACTs, we show the zenith angle  73    range, the total exposure, the energy range, the angular radius <math>\theta</math> of the signal or  74    ON region, the ratio of exposures between the background-control (OFF) and  75    signal (ON) regions (<math>\tau</math>), and the significance of gamma-ray excess in standard  76    deviations, <math>\sigma</math>.</p>	<p style="margin: 0;">. . . . . 36</p>
<p>77    Proof I know how to include</p>	<p style="margin: 0;">. . . . .</p>

## LIST OF FIGURES

79	Figure 2.1	Rotation curve fit to NGC 6503 from [7]. Dashed line is the contribution 80 from visible matter. Dotted curves are from gas. Dash-dot curves are from 81 dark matter (DM). Solid line is the composite contribution from all matter 82 and DM sources. Data are indicated with bold dots with error bars. Data 83 agree strongly with a matter + DM composite prediction. . . . .	5
84	Figure 2.2	Light from distant galaxy is bent in unique ways depending on the distribution 85 of mass between the galaxy and Earth. Yellow dashed lines indicate where 86 the light would have gone if the matter were not present [8]. . . . .	7
87	Figure 2.3	(left) Optical image of galactic cluster 1E0657-558. (right) X-ray image of the 88 cluster with redder meaning hotter and higher baryon density. (both) Green 89 contours are reconstruction of gravity contours from weak lensing. White 90 rings are the best fit mass maxima at 68.3%, 95.5%, and 99.7% confidence. 91 The matter maxima of the clusters are clearly separated from x-ray maxima. [9]	8
92	Figure 2.4	Plank CMB sky. Sky map features small variations in temperature in primor- 93 dial light. These anisotropies are used to make inferences about the universe's 94 energy budget and developmental history. [10] . . . . .	9
95	Figure 2.5	Observed Cosmic Microwave Background power spectrum as a function of 96 multipole moment from Plank [10]. Blue line is best fit model from $\Lambda$ CDM. 97 Red points and lines are data and error, respectively. . . . .	10
98	Figure 2.6	Predicted power spectra of CMB for different $\Omega_m h^2$ values for fixed baryon 99 density from [11]. (left) Low $\Omega_m h^2$ increases the prominence of first and 100 second peaks. (middle) $\Omega_m h^2$ is most similar to the observed power spectrum. 101 The second and third peaks are similar in height. (right) $\Omega_m h^2$ is large which 102 suppresses the first peak and raises the prominence of the third peak. . . . .	10
103	Figure 2.7	The Standard Model (SM) of particle physics. Figure taken from <a href="http://www.quantumdiaries.org/2014/03/14/the-standard-model-a-beautiful-but-flawed-theory/">http://www.quantumdiaries.org/2014/03/14/the-standard-model-a-beautiful-but-flawed-theory/</a> . . . . .	12
106	Figure 2.8	Simplified Feynman diagram demonstrating with different ways DM can 107 interact with SM particles. The 'X's refer to the DM particles whereas the 108 SM refer to fundamental particles in the SM. The large circle in the center 109 indicates the vertex of interaction and is purposely left vague. The colored 110 arrows refer to different directions of time as well as their respective labels. 111 The arrows indicate the initial and final state of the DM -SM interaction in time.	13

112	Figure 2.9 A single jet event in ATLAS detector from 2017 [16]. Jet momentum was 113 observed to be 1.9 TeV. Missing transverse momentum was observed to be 114 1.9 TeV compared to the initial transverse momentum of the event was 0. 115 Implied MET is traced by a red dashed line in event display. . . . .	14
116	Figure 2.10 More detailed pseudo-Feynman diagram of particle cascade from dark matter 117 annihilation into 2 quarks. The quarks hadronize and down to stable particles 118 like $\gamma$ or the anti-proton ( $p^-$ ). Diagram pulled from ICRC 2021 presentation 119 on DM annihilation search [17]. . . . .	15
120	Figure 2.11 Dark Matter (DM) decay spectrum for $b\bar{b}$ initial state and $\gamma$ final state. Redder 121 spectra are for larger DM masses. Bluer spectra are light DM masses. $x$ is a 122 unitless factor defined as the ratio of the mass of DM, $m_\chi$ , and the final state 123 particle energy $E_\gamma$ . Figure from [19]. . . . .	17
124	Figure 2.12 Different dark matter density profiles compared. Some models produce ex- 125 ceptionally large densities at small r [20]. . . . .	18
126	Figure 2.13 The Milky Way Galaxy in photons ( $\gamma$ ) and neutrinos ( $\nu$ ) [22]. The Galactic 127 center is at $l=0^\circ$ and is the brightest region in all panels. (top) An Optical 128 color image of the Milky Way galaxy seen from Earth. Clouds of gas and dust 129 obscure some light from stars. (2nd down) Integrated flux of $\gamma$ -rays observed 130 by the Fermi-LAT telescope [23]. (middle) Expected neutrino emission 131 that corresponds with Fermi-LAT observations. (2nd up) Expected neutrino 132 emission profile after considering detector systematics of IceCube. (bottom) 133 Observed neutrino emission from region of the galactic plane. Substantial 134 neutrino emission was detected. . . . .	19
135	Figure 2.14 Dark Matter annihilation spectra for different final state particle and standard 136 model annihilation channels [24]. Photons (red), $e^\pm$ (green), $\bar{p}$ (blue), $\nu$ (black). . . . .	20
137	Figure 3.1 TODO: Show a nuclear reactor with cherenkov radiation[NEEDS A SOURCE][FACT 138 CHECK THIS] . . . . .	22
139	Figure 3.2 TODO: absorption spectrum of liquid and solid water[NEEDS A SOURCE][FACT 140 CHECK THIS] . . . . .	23

141	Figure 7.1 [NEEDS A SOURCE] Sensitivities of five gamma-ray experiments compared 142 to percentages of the Crab nebula's emission and dark matter annihilation. 143 Solid lines present estimated sensitivities to power law spectra [FACT CHECK 144 THIS] for each experiment. Green lines are Fermi-LAT sensitivities where 145 lighter green is the sensitivity to the galactic center and dark green is its 146 sensitivity to higher declinations. Orange, red, and purple solid lines rep- 147 resent the MAGIC, HESS, and VERITAS 50 hour sensitivities respectively. 148 The maroon and brown lines are the HAWC 1 year and 5 year sensitivities. 149 Across four decades of gamma-ray energy, these experiments have similar 150 sensitivities on the order $10^{-12} \text{ erg cm}^{-2}\text{s}^{-1}$ . The dotted lines are estimated 151 dark matter fluxes assuming $m_\chi = 5 \text{ TeV}$ DM annihilating to bottom quarks 152 (red), tau leptons (blue), and W bosons (green). Faded gray lines outline 153 percentage flux of the Crab nebula. . . . .	28
154	Figure 7.2 Effect of Electro-Weak (EW) corrections on expected DM annihilation spec- 155 trum for $\chi\chi \rightarrow W^-W^+$ . Solid lines are spectral models that consider EW 156 corrections. Dash-dot lines are spectral models without EW corrections. Red 157 lines are models for $M_\chi = 1 \text{ TeV}$ . Blue lines represent models for $M_\chi = 100$ 158 TeV. All models are sourced from the PPPC4DMID [43]. . . . .	32
159	Figure 7.3 $\frac{dJ}{d\Omega}$ maps for Segue1 (top) and Coma Berenices (bottom). Origin is centered 160 on the specific dwarf spheroidal galaxies (dSph). X and Y axes are the 161 angular separation from the center of the dwarf. Plots of the remaining 11 162 dSph HAWC studied are linked in Fig. A.1. . . . .	34
163	Figure 7.4 Illustration of the combination technique showing a comparison between 164 $-2 \ln \lambda$ provided by four instruments (colored lines) from the observation 165 of the same dSph without any $J$ nuisance and their sum, <i>i.e.</i> the result- 166 ing combined likelihood (thin black line). According to the test statistics 167 of Equation (7.18), the intersection of the likelihood profiles with the line 168 $-2 \ln \lambda = 2.71$ indicates the 95% C.L. upper limit on $\langle \sigma v \rangle$ . The combined 169 likelihood (thin black line) shows a smaller value of upper limit on $\langle \sigma v \rangle$ than 170 those derived by individual instruments. We also show the uncertainties on 171 the $J$ -factor affects the combined likelihood and degrade the upper limit on 172 $\langle \sigma v \rangle$ (thick black line). All likelihood profiles are normalized so that the 173 global minimum $\widehat{\langle \sigma v \rangle}$ is 0. We note that each profile depends on the observa- 174 tional conditions in which a target object was observed. The sensitivity of a 175 given instrument can be degraded and the upper limits less constraining if the 176 observations are performed in non optimal conditions such as a high zenith 177 angle or a short exposure time. . . . .	39
178	Figure 7.5 HAWC upper limits at 95% confidence level on $\langle \sigma v \rangle$ versus DM mass for 179 seven annihilation channels, using the set of $J$ -factors from Ref. [49] The 180 solid line represents the observed combined limit. Dashed lines represent 181 limits from individual dSphs. . . . .	43

182	Figure 7.6 HAWC Brazil bands at 95% confidence level on $\langle\sigma v\rangle$ versus DM mass for	44
183	seven annihilation channels with $J$ -factors from $\mathcal{GS}$ [49]. The solid line	
184	represents the combined limit from 13 dSphs. The dashed line is the expected	
185	limit. The green band is the 68% containment. The yellow band is the 95%	
186	containment. . . . .	
187	Figure 7.7 Upper limits at 95% confidence level on $\langle\sigma v\rangle$ in function of the DM mass for	46
188	eight annihilation channels, using the set of $J$ factors from Ref. [49] ( $\mathcal{GS}$ set	
189	in Table 7.1). The black solid line represents the observed combined limit,	
190	the black dashed line is the median of the null hypothesis corresponding	
191	to the expected limit, while the green and yellow bands show the 68% and	
192	95% containment bands. Combined upper limits for each individual detector	
193	are also indicated as solid, colored lines. The value of the thermal relic	
194	cross-section in function of the DM mass is given as the red dotted-dashed	
195	line [53]. . . . .	
196	Figure 7.8 Same as Fig. 7.7, using the set of $J$ factors from Ref. [46, 52] ( $\mathcal{B}$ set in Table 7.1). 47	
197	Figure 7.9 Comparisons of the combined limits at 95% confidence level for each of the	48
198	eight annihilation channels when using the $J$ factors from Ref. [49] ( $\mathcal{GS}$ set in	
199	Table 7.1), plain lines, and the $J$ factor from Ref. [46, 52] ( $\mathcal{B}$ set in Table 7.1),	
200	dashed lines. The cross-section given by the thermal relic is also indicated [53].	
201	Figure 7.10 Comparisons of the combined limits at 95% confidence level for a point source	49
202	analysis and extended source using [49] $\mathcal{GS}$ J-factor distributions and PPPC	
203	[43] annihilation spectra. Shown are the limits for Segue1 which will have	
204	the most significant impact on the combined limit. 6 of the 7 DM annihilation	
205	channels are shown. Solid lines are extended source studies. Dashed lines	
206	are point source studies. Overall, the extended source analysis improves the	
207	limit by a factor of 2. . . . .	
208	Figure 7.11 Same as Fig. 7.10 on Coma Berenices. This dSph also contributes signifi-	50
209	cantly to the limit. The limits are identical in this case. . . . .	
210	Figure 7.12 Comparison of combined limits when correcting for HAWC's pointing sys-	51
211	tematic. All DM annihilation channels are shown. The solid black line is the	
212	ratio between published limit to the declination corrected limit. The blue solid	
213	line or "Combined_og" represented the limits computed for Glory Duck. The	
214	solid orange line or "Combined_ad" represented the limits computed after	
215	correcting for the pointing systematic. . . . .	
216	Figure 7.13 Differential map of $dJ/\Omega$ from model built in Section 7.8.1 and profiles	53
217	provided directly from authors. (Top) Differential from Segue1. (bottom)	
218	Differential from Coma Berenices. Note that their scales are not the same.	
219	Segue1 shows the deepest discrepancies which is congruent with its large	
220	uncertainties. Both models show anuli where unique models become apparent. .	

221	Figure 7.14 HAWC limits for Coma Berenices (top) and Segue1 (bottom) for two different 222 map sets. Blue lines are limits calculated on maps with poor model repre- 223 sentation. Orange lines are limits calculated on spatial profiles provided by 224 the authors of [44]. Black line is the ratio of the poor spatial model limits to 225 the corrected spatial models. The left y-axis measures $\langle\sigma v\rangle$ for the blue and 226 orange lines. The right y-axis measures the ratio and is unitless. . . . .	54
227	Figure 7.15 Comparisons between the $J$ -factors versus the angular radius for the com- 228 putation of $J$ factors from Ref. [49] ( $\mathcal{GS}$ set in Table 7.1) in blue and for 229 the computation from Ref. [46, 52] ( $\mathcal{B}$ set in Tab. 7.1) in orange. The solid 230 lines represent the central value of the $J$ -factors while the shaded regions 231 correspond to the $1\sigma$ standard deviation. . . . .	56
232	Figure 7.16 Comparisons between the $J$ -factors versus the angular radius for the computa- 233 tion of $J$ factors from Ref. [49] ( $\mathcal{GS}$ set in Tab. 7.1) in blue and for the 234 computation from Ref. [46, 52] ( $\mathcal{B}$ set in Tab. 7.1) in orange. The solid 235 lines represent the central value of the $J$ -factors while the shaded regions 236 correspond to the $1\sigma$ standard deviation. . . . .	57
237	Figure A.1 Sister figure to Figure 7.3. Sources in the first row from left to right: Boötes 238 I, Canes Venatici I, II. In second row: Draco, Hercules, Leo I. In the first row: 239 Leo II, Leo IV, Sextans. In the final row: Ursa Major I, Ursa Major II. . . . .	63

**LIST OF ABBREVIATIONS**

- 241 **MSU** Michigan State University  
242 **LANL** Los Alamos National Laboratory  
243 **DM** Dark Matter  
244 **SM** Standard Model  
245 **HAWC** High Altitude Water Cherenkov Observatory

246

## **CHAPTER 1**

### **INTRODUCTION**

247 Is the text not rendering right? Ah ok it knows im basically drafting the doc still

## CHAPTER 2

248

### DARK MATTER IN THE COSMOS

249 **2.1 Introduction**

250 The dark matter problem can be summarized in part by the following thought experiment.

251 Let us say you are the teacher for an elementary school classroom. You take them on a field  
252 trip to your local science museum and among the exhibits is one for mass and weight. The exhibit  
253 has a gigantic scale, and you come up with a fun problem for your class.

254 You ask your class, "What is the total weight of the classroom? Give your best estimation to  
255 me in 30 minutes, and then we'll check your guess on the scale. If your guess is within 10% of the  
256 right answer, we will stop for ice cream on the way back."

257 The students are ecstatic to hear this, and they get to work. The solution is some variation of  
258 the following strategy. The students should give each other their weight or best guess if they do  
259 not know. Then, all they must do is add each student's weight and get a grand total for the class.  
260 The measurement on the giant scale should show the true weight of the class. When comparing  
261 the measured weight to your estimation, multiply the measurement by  $1.0 \pm 0.1$  to get the  $\pm 10\%$   
262 tolerances for your estimation.

263 Two of your students, Sandra and Mario, return to you with a solution.

264 They say, "We weren't sure of everyone's weight. We used 65 lbs. for the people we didn't  
265 know and added everyone who does know. There are 30 of us, and we got 2,000 lbs.! That's a ton!"

266 You estimated 1,900 lbs. assuming the average weight of a student in your class was 60 lbs.  
267 So, you are pleased with Sandra's and Mario's answer. You instruct your students to all gather on  
268 the giant scale and read off the weight together. To all your surprise, the scale reads *10,000 lbs.*!  
269 10,000 is significantly more than a 10% error from 2,000. In fact, it is approximately 5 times more  
270 massive than either your or your students' estimates. You think to yourself and conclude there  
271 must be something wrong with the scale. You ask an employee to check the scale and verify it is  
272 well calibrated. They confirm that the scale is in working order. You weigh a couple of students  
273 individually to assess that the scale is well calibrated. Sandra weighs 59 lbs., and Mario weighs

274 62 lbs., typical weights for their age. You then weigh each student individually and see that their  
275 weights individually do not deviate greatly from 60 lbs. So, where does all the extra weight come  
276 from?

277 This thought experiment serves as an analogy to the Dark Matter problem. The important  
278 substitution to make however is to replace the students with stars and the classroom with a galaxy,  
279 say the Milky Way. Individually the mass of stars is well measured and defined with the Sun as our  
280 nearest test case. However, when we set out to measure the mass of a collection of stars as large as  
281 galaxies, our well-motivated estimation is wildly incorrect. There simply is no way to account for  
282 this discrepancy except without some unseen, or dark, contribution to mass and matter in galaxies.  
283 I set out in my thesis to narrow the possibilities of what this Dark Matter could be.

284 This chapter is organized like the following... **TODO: Text should look like ... Chapter x has**  
285 **blah blah blah.**

## 286 2.2 Dark Matter Basics

287 Presently, a more compelling theory of cosmology that includes Dark Matter (DM) in order  
288 to explain a variety of observations is  $\Lambda$  Cold Dark Matter, or  $\Lambda$ CDM. I present the evidence  
289 supporting  $\Lambda$ CDM in Section 2.3 yet discuss the conclusions of the  $\Lambda$ CDM model here. According  
290 to  $\Lambda$ CDM fit to observations on the Cosmic Microwave Background (CMB), DM is 26.8% of the  
291 universe's current energy budget. Baryonic matter, stuff like atoms, gas, and stars, contributes to  
292 4.9% of the universe's current energy budget [1, 2, 3].

293 DM is dark; it does not interact readily with light at any wavelength. DM also does not interact  
294 noticeably with the other standard model forces (Strong and Weak) at a rate that is readily observed  
295 [3]. DM is cold, which is to say that the average velocity of DM is below relativistic speeds [1].  
296 'Hot' DM would not likely manifest the dense structures we observe like galaxies, and instead  
297 would produce much more diffuse galaxies than what is observed [3, 1]. DM is old; it played a  
298 critical role in the formation of the universe and the structures within it [1, 2].

299 Observations of DM have so far been only gravitational. The parameter space available to what  
300 DM could be therefore is extremely broad. The broad DM parameter space is iteratively tested in

301 DM searches by supposing a hypothesis that has not yet been ruled out and performing observations  
302 to test them. When the observations yield a null result, the parameter space is constrained further.  
303 I present some approaches for DM searches in Section 2.4.

304 **2.3 Evidence for Dark Matter**

305 Dark Matter (DM) has been a looming problem in physics for almost 100 years. Anomalies  
306 have been observed by astrophysicists in galactic dynamics as early as 1933 when Fritz Zwicky  
307 noticed unusually large velocity dispersion in the Coma cluster. Zwicky's measurement was the  
308 first recorded to use the Virial theorem to measure the mass fraction of visible and invisible matter  
309 in celestial bodies [4]. From Zwicky in [5], "*If this would be confirmed, we would get the surprising*  
310 *result that dark matter is present in much greater amount than luminous matter.*" Zwicky's and  
311 others' observation did not instigate a crisis in astrophysics because the measurements did not  
312 entirely conflict with their understanding of galaxies [4]. In 1978, Rubin, Ford, and Norbert  
313 measured rotation curves for ten spiral galaxies [6]. Rubin et al.'s 1978 publication presented a  
314 major challenge to the conventional understanding of galaxies that could no longer be dismissed by  
315 measurement uncertainties. Evidence has been mounting ever since for this exotic form of matter.  
316 The following subsections provide three compelling pieces of evidence in support of the existence  
317 of DM.

318 **2.3.1 First Clues: Stellar Velocities**

319 Zwicky, and later Rubin, measured the stellar velocities of various galaxies to estimate their  
320 virial mass. The Virial Theorem upon which these observations are interpreted is written as

$$2T + V = 0. \quad (2.1)$$

321 Where  $T$  is the kinetic energy and  $V$  is the potential energy in a self-gravitating system. The  
322 classical Newton's law of gravity from stars and gas was used for gravitational potential modeled in  
323 the observed galaxies:

$$V = -\frac{1}{2} \sum_i \sum_{j \neq i} \frac{m_i m_j}{r_{ij}}. \quad (2.2)$$

324 Zwicky et al. measured just the velocities of stars apparent in optical wavelengths [5]. Rubin et al.  
 325 added by measuring the velocity of the hydrogen gas via the 21 cm emission line of Hydrogen [6].  
 326 The velocities of the stars and gas are used to infer the total mass of galaxies and galaxy clusters  
 327 via Equation (2.1). An inferred mass is obtained from the luminosity of the selected sources. The  
 328 two inferences are compared to each other as a luminosity to mass ratio which typically yielded [1]

$$\frac{M}{L} \sim 400 \frac{M_{\odot}}{L_{\odot}} \quad (2.3)$$

329  $M_{\odot}$  and  $L_{\odot}$  referring to stellar mass and stellar luminosity, respectively. These ratios clearly indicate  
 330 a discrepancy in apparent light and mass from stars and gas and their velocities.

331 Rubin et al. [6] demonstrated that the discrepancy was unlikely to be an underestimation of  
 332 the mass of the stars and gas. The inferred "dark" mass was up to 5 times more than the luminous  
 333 mass. This dark mass also needed to extend well beyond the extent of the luminous matter.

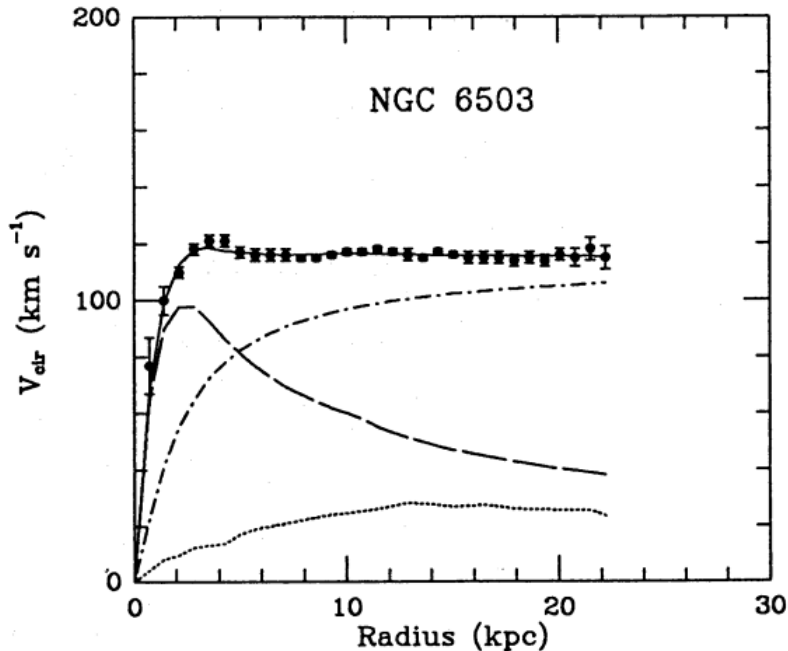


Figure 2.1 Rotation curve fit to NGC 6503 from [7]. Dashed line is the contribution from visible matter. Dotted curves are from gas. Dash-dot curves are from dark matter (DM). Solid line is the composite contribution from all matter and DM sources. Data are indicated with bold dots with error bars. Data agree strongly with a matter + DM composite prediction.

334 Figure 2.1 features one of many rotation curves plotted from the stellar velocities within galaxies.

335 The measured rotation curves mostly feature a flattening of velocities at higher radius which is not  
336 expected if the gravity was only coming from gas and luminous matter. The extension of the  
337 flat velocity region also indicates that the DM is distributed far from the center of the galaxy.  
338 Modern velocity measurements include significantly larger objects, galactic clusters, and smaller  
339 objects, dwarf galaxies. Yet, measurements along this regime are leveraging the Virial theorem  
340 with Newtonian potential energies. We know Newtonian gravity is not a comprehensive description  
341 of gravity. New observational techniques have been developed since 1978, and those are discussed  
342 in the following sections.

343 **2.3.2 Evidence for Dark Matter: Gravitational Lensing**

344 Modern evidence for dark matter comes from new avenues beyond stellar velocities. Grav-  
345 itational lensing from DM is a new channel from general relativity. General relativity predicts  
346 aberrations in light caused by massive objects. In recent decades we have been able to measure the  
347 lensing effects from compact objects and DM halos. Figure 2.2 shows how different massive ob-  
348 jects change the final image of a faraway galaxy resulting from gravitational lensing. Gravitational  
349 lensing developed our understanding of dark matter in two important ways.

350 Gravitational lensing provides additional compelling evidence for DM. The observation of two  
351 merging galactic clusters in 2006, shown in Figure 2.3, provided a compelling argument for DM  
352 outside the Standard Model. These clusters merged recently in astrophysical time scales. Galaxies  
353 and star cluster have mostly passed by each other as the likelihood of their collision is low. Therefore,  
354 these massive objects will mostly track the highest mass, dark and/or baryonic, density. Yet, the  
355 intergalactic gas is responsible for the majority of the baryonic mass in the systems [4]. These gas  
356 bodies will not phase through and will heat up as they collide together. The hot gas is located via  
357 x-ray emission from the cluster. Two observations of the clusters were performed independently of  
358 each other.

359 The first was the lensing of light around the galaxies due to their gravitational influences.  
360 When celestial bodies are large enough, the gravity they exert bends space and time itself. The  
361 warped space-time lenses light and will deflect in an analogous way to how glass lenses will bend

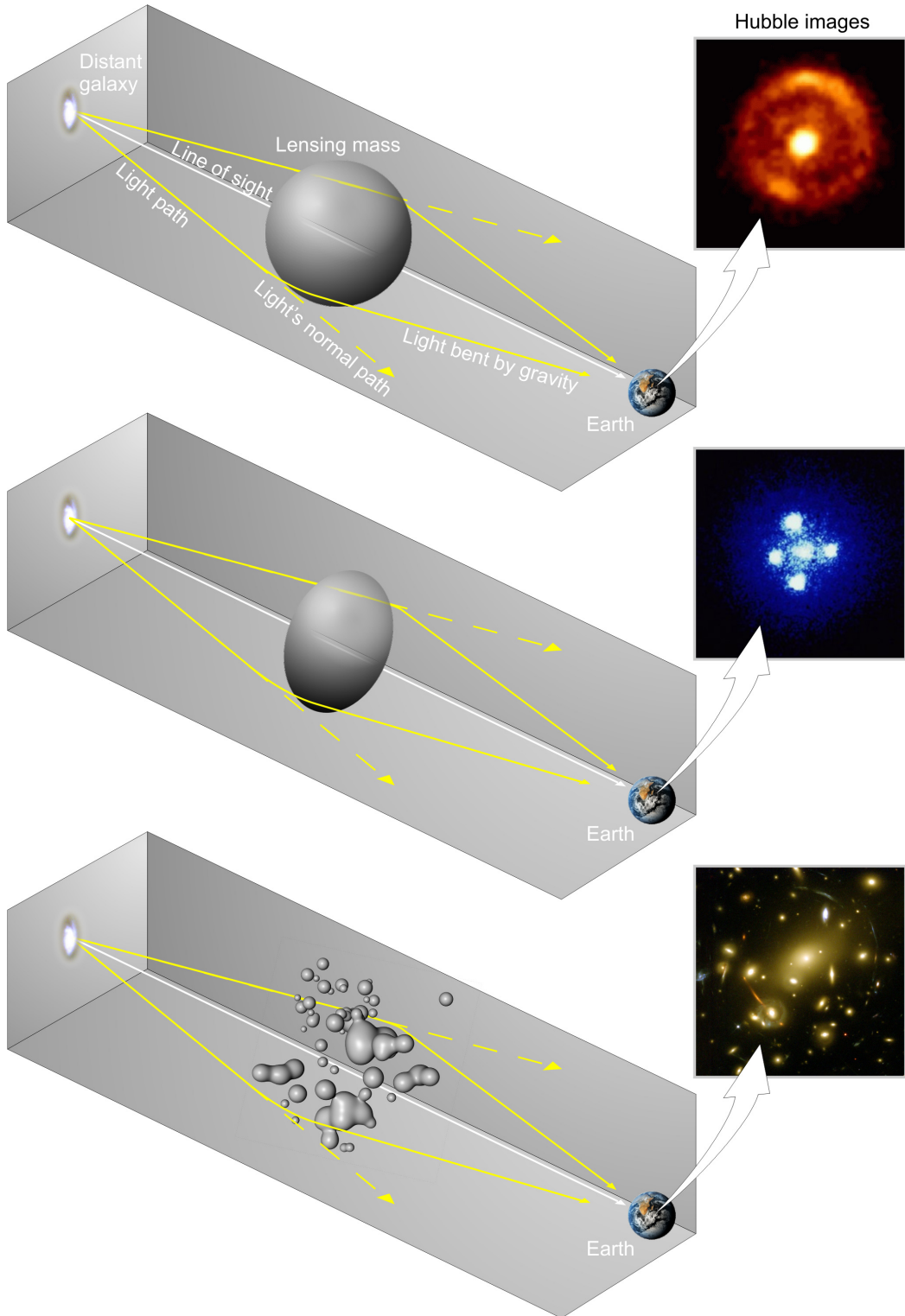


Figure 2.2 Light from distant galaxy is bent in unique ways depending on the distribution of mass between the galaxy and Earth. Yellow dashed lines indicate where the light would have gone if the matter were not present [8].

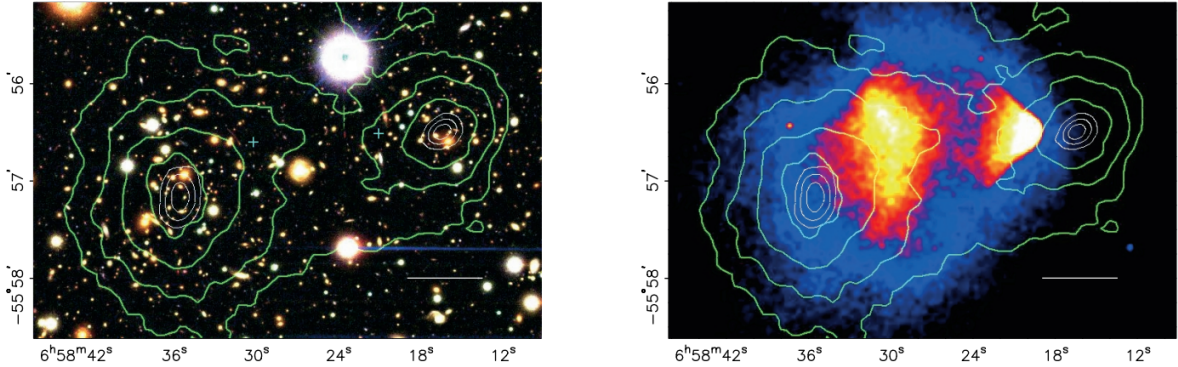


Figure 2.3 (left) Optical image of galactic cluster 1E0657-558. (right) X-ray image of the cluster with redder meaning hotter and higher baryon density. (both) Green contours are reconstruction of gravity contours from weak lensing. White rings are the best fit mass maxima at 68.3%, 95.5%, and 99.7% confidence. The matter maxima of the clusters are clearly separated from x-ray maxima. [9]

362 light, see Figure 2.2. With a sufficient understanding of light sources behind a massive object, we  
 363 can reconstruct the contours of the gravitational lenses. The gradient of the contours shown in  
 364 Figure 2.3 then indicates how dense the matter is and where it is.

365 The x-ray emission can then be observed from the clusters. Since these galaxies are mostly gas  
 366 and are merging, then the gas should be getting hotter. If they are merging, the x-ray emissions  
 367 should be the strongest where the gas is mostly moving through each other. Hence, X-ray emission  
 368 maps out where the gas is in the merging galaxy cluster.

369 The lensing and x-ray observations were done on the Bullet cluster featured on Figure 2.3.  
 370 The x-ray emissions do not align with the gravitational contours from lensing. The incongruence  
 371 in mass density and baryon density suggests that there is a lot of matter somewhere that does  
 372 not interact with light. Moreover, this dark matter cannot be baryonic [9]. The Bullet Cluster  
 373 measurement did not really tell us what DM is exactly, but it did give the clue that DM also does  
 374 not interact with itself very strongly. If DM did interact strongly with itself, then it would have been  
 375 more aligned with the x-ray emission [9]. There have been follow-up studies of galaxy clusters with  
 376 similar results. The Bullet Cluster and others like it provide a persuasive case against something  
 377 possibly amiss in our gravitational theories.

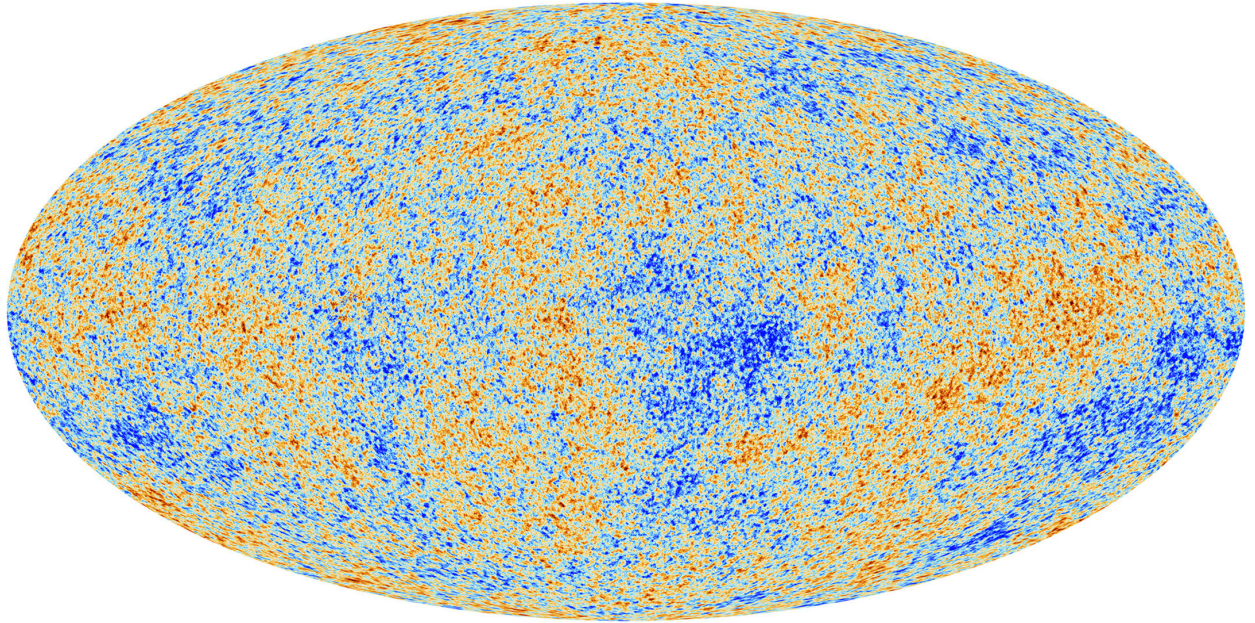


Figure 2.4 Plank CMB sky. Sky map features small variations in temperature in primordial light. These anisotropies are used to make inferences about the universe's energy budget and developmental history. [10]

378     **2.3.3 Evidence for Dark Matter: Cosmic Microwave Background**

379       The Cosmic Microwave Background (CMB) is the primordial light from the early universe  
380       when Hydrogen atoms formed from the free electron and proton soup in the early universe. The  
381       CMB is the earliest light we can observe; released when the universe was about 380,000 years old.  
382       Then we look at how the simulated universes look like compared to what we see. Figure 2.4 is the  
383       most recent CMB image from the Plank satellite after subtracting the average value and masking the  
384       galactic plane [10]. Redder regions indicate a slightly hotter region in the CMB, and blue indicates  
385       colder. The intensity variations are on the order of 1 in 1000 with respect to the average value.

386       The Cosmic Microwave Background shows that the universe had DM in it from an incredibly  
387       early stage. To measure the DM, Dark Energy, and matter fractions of the universe from the CMB,  
388       the image is analyzed into a power spectrum, which shows the amplitude of the fluctuations as  
389       a function of spherical multipole moments.  $\Lambda$ CDM provides the best fit to the power spectra of  
390       the CMB as shown in Figure 2.5. The CMB power spectrum is quite sensitive to the fraction  
391       of each energy contribution in the early universe. Low  $l$  modes are dominated by variations  
392       in gravitational potential. Intermediate  $l$  emerge from oscillations in photon-baryon fluid from

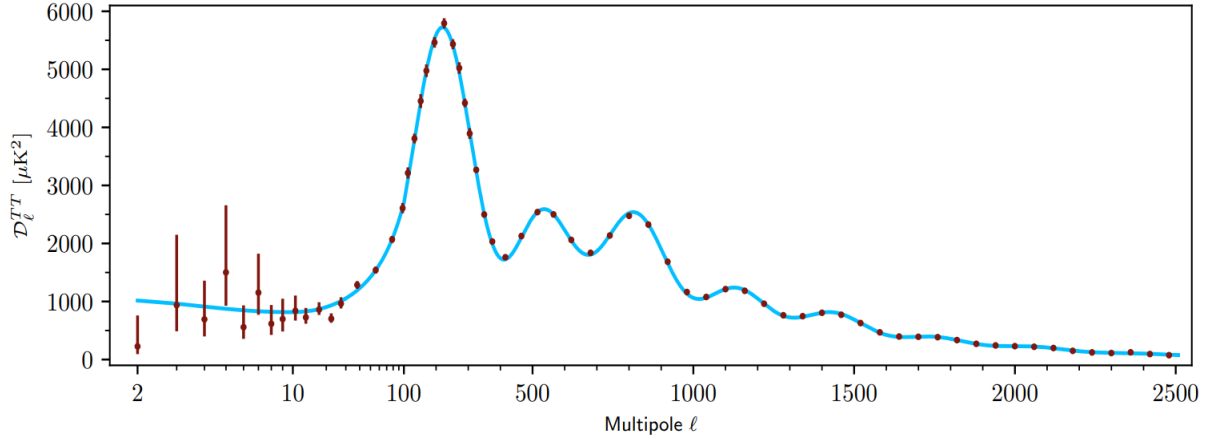


Figure 2.5 Observed Cosmic Microwave Background power spectrum as a function of multipole moment from Plank [10]. Blue line is best fit model from  $\Lambda$ CDM. Red points and lines are data and error, respectively.

393 competing baryon pressures and gravity. High  $l$  is a damped region from the diffusion of photons  
 394 during electron-proton recombination. [1]

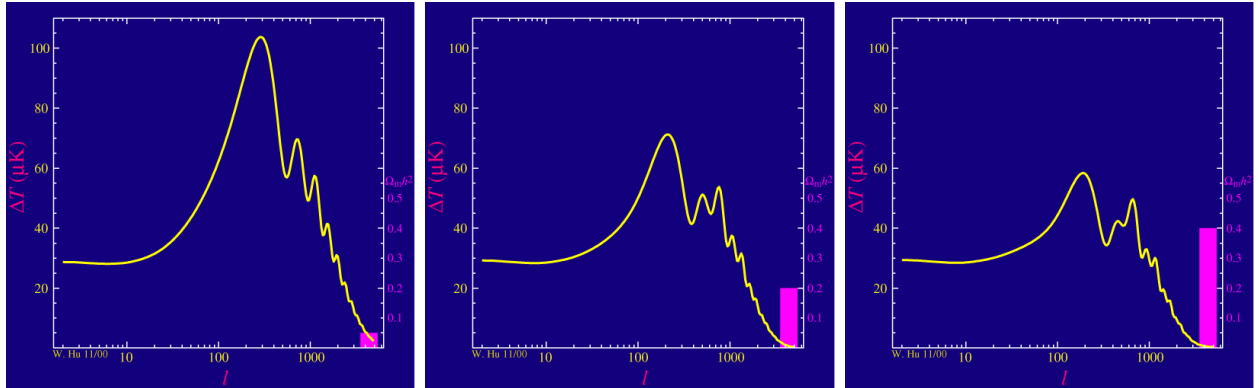


Figure 2.6 Predicted power spectra of CMB for different  $\Omega_m h^2$  values for fixed baryon density from [11]. (left) Low  $\Omega_m h^2$  increases the prominence of first and second peaks. (middle)  $\Omega_m h^2$  is most similar to the observed power spectrum. The second and third peaks are similar in height. (right)  $\Omega_m h^2$  is large which suppresses the first peak and raises the prominence of the third peak.

395 The harmonics would look quite different for a universe with less DM. Figure 2.6 demonstrates  
 396 the effect  $\Omega_m h^2$  has on the expected power spectrum for fixed baryon matter density. [11] Sweeping  
 397  $\Omega_m h^2$  in this way clearly shows the effect dark matter has on the CMB power spectrum. The  
 398 observations fit well with the  $\Lambda$ CDM model, and the derived fractions are as follows. The matter  
 399 fraction:  $\Omega_m = 0.3153$ ; and the baryon fraction:  $\Omega_b = 0.04936$  [10]. Plank's observations also  
 400 provide a measure of the Hubble constant,  $H_0$ .  $H_0$  especially has seen a growing tension in the

401 past decade that continues to deepened with observations from instruments like the James Webb  
402 Telescope [12, 13]. As Hubble tensions deepen, we may find that perhaps  $\Lambda$ **CDM**, despite its  
403 successes, is missing some critical physics.

404 Overall, the Newtonian motion of stars in galaxies, weak lensing from galactic clusters, and  
405 power spectra from primordial light form a compelling body of research in favor of dark matter.  
406 It takes another leap of theory and experimentation to make observations of DM that are non-  
407 gravitational in nature. In Section 2.3, the evidence for DM implies strongly that the DM is matter  
408 and not a lost parameter in the gravitational fields between massive objects. Finally, if we take one  
409 axiom: that this matter has quantum behavior, such as being described by some Bohr wavelength  
410 and abiding by some fermion or boson statistics; then we arrive at particle dark matter. One particle  
411 DM hypothesis is the Weakly Interacting Massive Particle (WIMP). This DM candidate theory is  
412 discussed further in the next section and is the focus of this thesis.

413 **2.4 Searching for Dark Matter: Particle DM**

414 Section 2.4 shows the Standard Model of particle physics and is currently the most accurate  
415 model for the dynamics of fundamental particles like electrons and photons. The current status  
416 of the SM does not have a viable DM candidate. When looking at the standard model, we can  
417 immediately exclude any charged particle because charged particles interact strongly with light.  
418 Specifically, this will rule out the following charged, fundamental particles:  $e, \mu, \tau, W, u, d, s, c, t, b$   
419 and their corresponding antiparticles. Recalling from Section 2.2 that DM must be long-lived and  
420 stable over the age of the universe which excludes all SM particles with decay half-lives at or shorter  
421 than the age of the universe. The lifetime constraint additionally eliminates the  $Z$  and  $H$  bosons.  
422 Finally, the candidate DM needs to be somewhat massive. Recall from Section 2.2 that DM is cold  
423 or not relativistic through the universe. This eliminates the remaining SM particles:  $\nu_{e,\mu,\tau}, g, \gamma$  as  
424 DM candidates. Because there are no DM candidates within the SM, the DM problem strongly  
425 hints to physics beyond the SM (BSM).

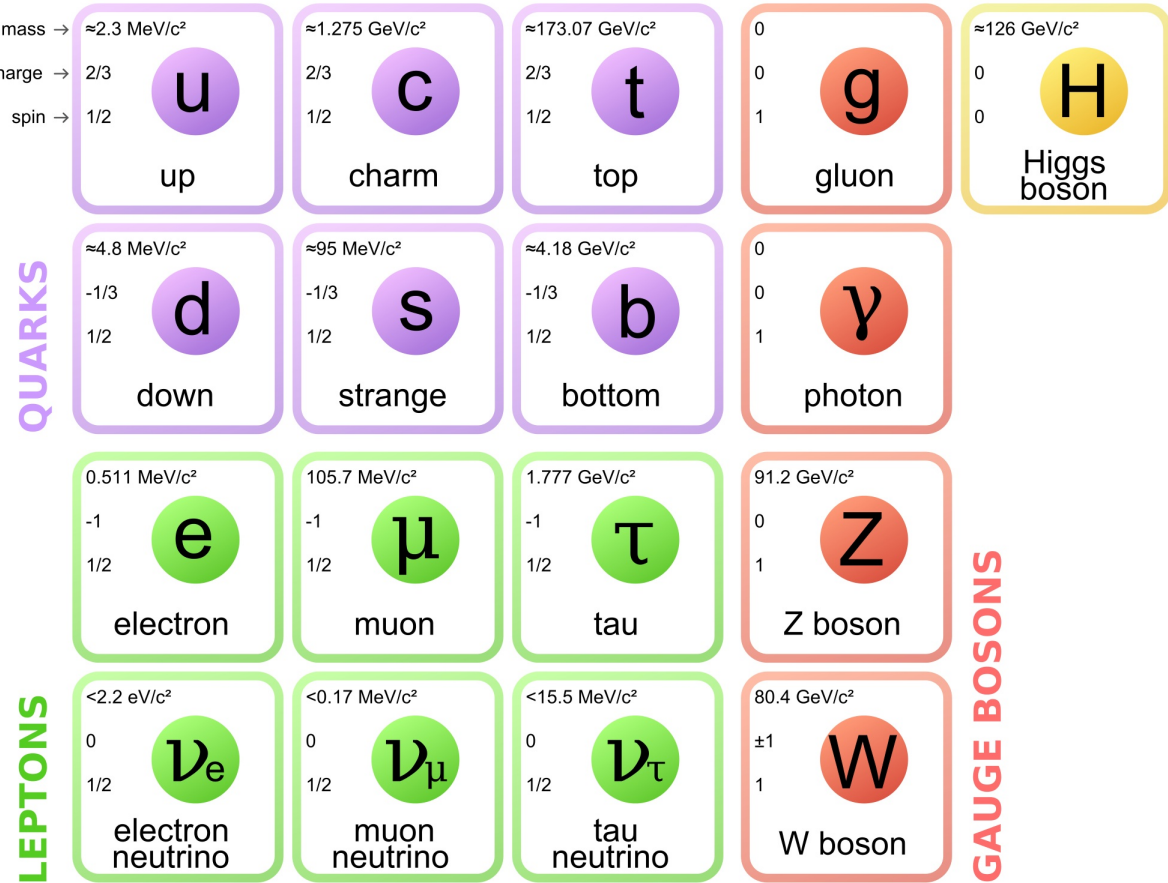


Figure 2.7 The Standard Model (SM) of particle physics. Figure taken from <http://www.quantumdiaries.org/2014/03/14/the-standard-model-a-beautiful-but-flawed-theory/>

#### 426 2.4.1 Shake it, Break it, Make it

427 When considering DM that couples in some way with the SM, the interactions are roughly  
 428 demonstrated by interaction demonstrated in Figure 2.8. The figure is a simplified Feynman  
 429 diagram where the arrow of time represents the interaction modes of: **Shake it, Break it, Make it**.

430 **Shake it** refers to the direct detection of dark matter. Direct detection interactions start with  
 431 a free DM particle and an SM particle. The DM and SM interact via elastic or inelastic collision  
 432 and recoil away from each other. The DM remains in the dark sector and imparts some momentum  
 433 onto the SM particle. The hope is that the momentum imparted onto the SM particle is sufficiently  
 434 high enough to pick up with extremely sensitive instruments. Because we cannot create the DM in  
 435 the lab, a direct detection experiment must wait until DM is incident on the detector. Most direct  
 436 detection experiments are therefore placed in low-background environments with inert detection

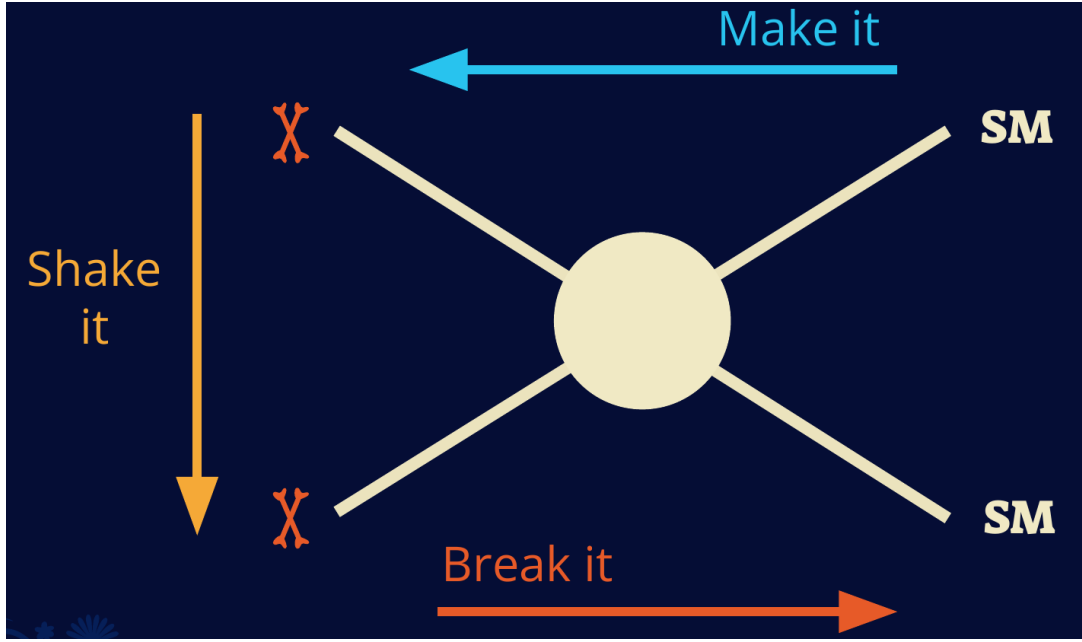


Figure 2.8 Simplified Feynman diagram demonstrating different ways DM can interact with SM particles. The 'X's refer to the DM particles whereas the SM refer to fundamental particles in the SM. The large circle in the center indicates the vertex of interaction and is purposely left vague. The colored arrows refer to different directions of time as well as their respective labels. The arrows indicate the initial and final state of the DM -SM interaction in time.

<sup>437</sup> media like the noble gas Xenon. [14]

<sup>438</sup> **Make it** refers to the production of DM from SM initial states. The experiment starts with  
<sup>439</sup> particles in the SM. These SM particles are accelerated to incredibly high energies and then collide  
<sup>440</sup> with each other. In the confluence of energy, DM hopefully emerges as a byproduct of the SM  
<sup>441</sup> annihilation. Often it is the collider experiments that are energetic enough to hypothetically produce  
<sup>442</sup> DM. These experiments include the world-wide collaborations ATLAS and CMS at CERN where  
<sup>443</sup> proton collide together at extreme energies. The DM searches, however, are complex. DM likely  
<sup>444</sup> does not interact with the detectors and lives long enough to escape the detection apparatus of  
<sup>445</sup> CERN's colliders. This means any DM production experiment searches for an excess of events  
<sup>446</sup> with missing momentum or energy in the events. An example event with missing transverse  
<sup>447</sup> momentum is shown in Figure 2.9. The missing momentum with no particle tracks implies a  
<sup>448</sup> neutral particle carried the energy out of the detector. However, there are other neutral particles  
<sup>449</sup> in the SM, like neutrons or neutrinos, so any analysis has to account for SM signatures of missing

450 momentum. [15]

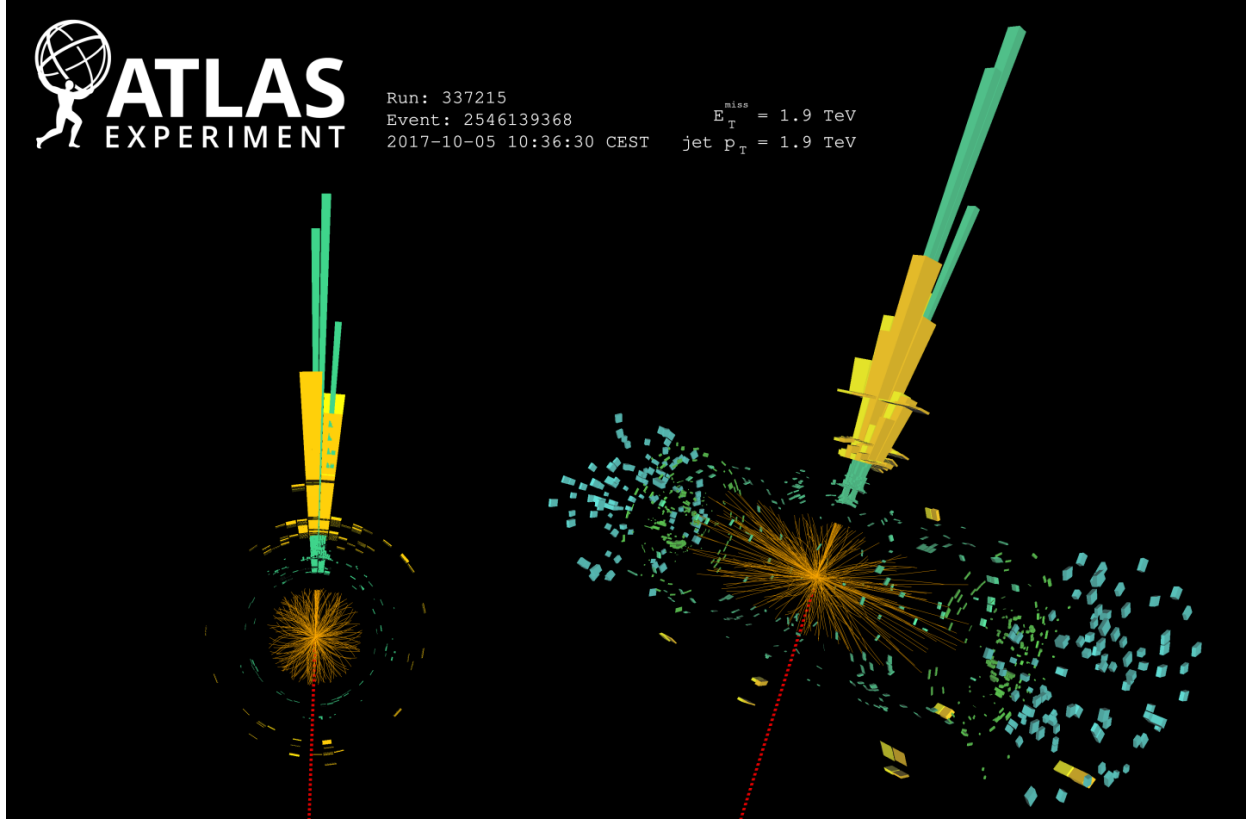


Figure 2.9 A single jet event in ATLAS detector from 2017 [16]. Jet momentum was observed to be 1.9 TeV. Missing transverse momentum was observed to be 1.9 TeV compared to the initial transverse momentum of the event was 0. Implied MET is traced by a red dashed line in event display.

#### 451 2.4.2 Break it: Standard Model Signatures of Dark Matter through Indirect Searches

452 **Break it** refers to the creation of SM particles from the dark sector, and it is the primary focus  
453 of this thesis. The interaction begins with DM or in the dark sector. The hypothesis is that this  
454 DM will either annihilate with itself or decay and produce an SM byproduct. This method is  
455 often referred to as the Indirect Detection of DM because we have no lab to directly control or  
456 manipulate the DM. Therefore, most indirect DM searches are performed using observations of  
457 known DM densities among the astrophysical sources. The strength is that we have the whole of the  
458 universe and its 13.6-billion-year lifespan to use as a detector and particle accelerator. Additionally,  
459 locations of dark matter are well cataloged since it was astrophysical observations that presented

460 the problem of DM in the first place.

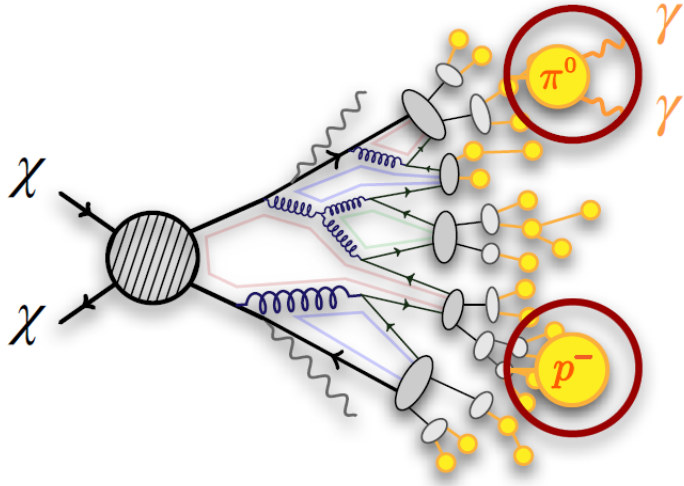


Figure 2.10 More detailed pseudo-Feynman diagram of particle cascade from dark matter annihilation into 2 quarks. The quarks hadronize and down to stable particles like  $\gamma$  or the anti-proton ( $p^-$ ). Diagram pulled from ICRC 2021 presentation on DM annihilation search [17].

461 However, anything can happen in the universe. There are many difficult to deconvolve back-  
462 grounds when searching for DM. One prominent example is the galactic center. We know the  
463 galactic center has a large DM content because of stellar kinematics in our Milky Way and DM halo  
464 simulations. Yet, any signal from the galactic center is challenging to parse apart from the extreme  
465 environment of our supermassive black hole, unresolved sources, and diffuse emission from the  
466 interstellar medium [18]. Despite the challenges, any DM model that yields evidence in the other  
467 two observation methods, **Shake it or Make it** must be corroborated with indirect observations of  
468 the known DM sources. Without corroborating evidence, DM observation in the lab is hard-pressed  
469 to demonstrate that it is the model contributing to the DM seen at the universal scale.

470 In the case of WIMP DM, signals are described in terms of primary SM particles produced  
471 from DM decay or annihilation. The SM initial state particles are then simulated down to stable  
472 final states such as the  $\gamma$ ,  $\nu$ ,  $p$ , or  $e$  which can traverse galactic lengths to reach Earth.

473 Figure 2.10 shows the quagmire of SM particles that emerges from SM initial states that are not  
474 stable [17]. There are many SM particles with varying energies that can be produced in such an

475 interaction. For any arbitrary DM source and stable SM particle, the SM flux from DM annihilating  
 476 to a neutral particle in the SM,  $\phi$ , from a region in the sky is described by the following.

$$\frac{d\Phi_\phi}{dE_\phi} = \frac{\langle\sigma v\rangle}{8\pi m_\chi^2} \frac{dN_\phi}{dE_\phi} \times \int_{\text{source}} d\Omega \int_{l.o.s} \rho_\chi^2 dl(r, \theta') \quad (2.4)$$

477 In Equation (7.1),  $\langle\sigma v\rangle$  is the velocity-weighted annihilation cross-section of DM to the SM.  $m_\chi$   
 478 refers to the mass of DM, noted with Greek letter  $\chi$ .  $\frac{dN_\phi}{dE_\phi}$  is the N particle flux weighted by the  
 479 particle energy. An example is provided in Figure 2.11 for the  $\gamma$  final state. The integrated terms  
 480 are performed over the solid angle,  $d\Omega$ , and line of sight, l.o.s.  $\rho$  is the density of DM for a  
 481 location  $(r, \theta')$  in the sky. The terms left of the ' $\times$ ' are often referred to as the particle physics  
 482 component. The terms on the right are referred to as the astrophysical component. For decaying  
 483 DM, the equation changes to...

$$\frac{d\Phi_\phi}{dE_\phi} = \frac{1}{4\pi\tau m_\chi} \frac{dN_\phi}{dE_\phi} \times \int_{\text{source}} d\Omega \int_{l.o.s} \rho_\chi dl(r, \theta') \quad (2.5)$$

484 In Equation (2.5),  $\tau$  is the decay lifetime of the DM. Just as in Equation (7.1), the left and  
 485 right terms are the particle physics and the astrophysical components respectively. The integrated  
 486 astrophysical component of Equation (7.1) is often called the J-Factor. Whereas the integrated  
 487 astrophysical component of Equation (2.5) is often called the D-Factor.

488 Exact DM  $\text{DM} \rightarrow \text{SM SM}$  branching ratios are not known, so it is usually assumed to go 100%  
 489 into an SM particle/anti-particle. Additionally, when a DM annihilation or decay produces one of  
 490 the neutral, long-lived SM particles ( $\nu$  or  $\gamma$ ), the particle is traced back to a DM source. For DM  
 491 above GeV energies, there are very few SM processes that can produce particles with such a high  
 492 energy. Seeing such a signal would almost certainly be an indication of the presence of dark matter.  
 493 Fortunately, the universe provides us with the largest volume and lifetime ever for a particle physics  
 494 experiment.

## 495 2.5 Sources for Indirect Dark Matter Searches

496 The first detection of DM relied on optical observations. Since then, we have developed new  
 497 techniques to find DM dense regions. As described in Section 2.3.1, many DM dense regions were  
 498 through observing galactic rotation curves. Our Milky Way galaxy is among DM dense regions

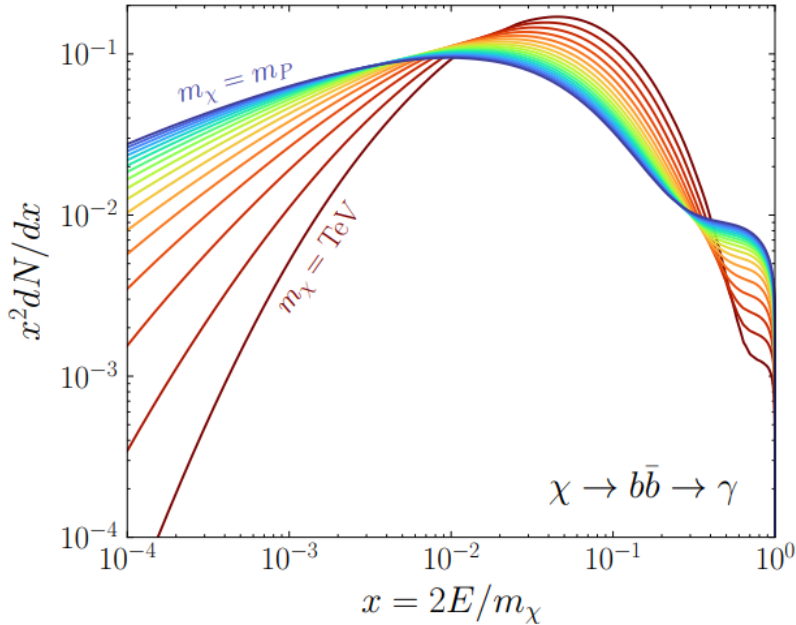


Figure 2.11 Dark Matter (DM) decay spectrum for  $b\bar{b}$  initial state and  $\gamma$  final state. Redder spectra are for larger DM masses. Bluer spectra are light DM masses.  $x$  is a unitless factor defined as the ratio of the mass of DM,  $m_\chi$ , and the final state particle energy  $E_\gamma$ . Figure from [19].

499 discovered, and it is the largest nearby DM dense region to look at. Additionally, the DM halo  
 500 surrounding the Milky Way is clumpy [18]. There are regions in the DM halo of the Milky Way that  
 501 have more DM than others that have captured gas over time. These sub-halos were dense enough  
 502 collapse gas and form stars. These apparent sub galaxies are known as dwarf spheroidal galaxies  
 503 and are the main sources studied in this thesis. Each source type comes with different trade-offs.  
 504 Galactic Center studies will be very sensitive to the assumed distribution of DM. The central DM  
 505 density can vary substantially as demonstrated in Figure 2.12. At distances close to the center of  
 506 the galaxy, or small  $r$ , the differences in DM densities can be 3-4 orders of magnitude. Searches  
 507 toward the galactic center will therefore be quite sensitive to the assumed DM distribution.

508     Searches toward Dwarf Spheroidal Galaxies (dSph's) suffer from uncertainties in the DM  
 509 density less than the galactic center studies. This is mostly from their diminutive size being smaller  
 510 than the angular resolution of most  $\gamma$ -ray observatories [18]. The DM content dSph's are typically  
 511 determined with the Virial theorem, Equation (2.1), and are usually majority DM [18] in mass.  
 512 DSph's tend to be ideal sources to look at for DM searches. Their environments are quiet with little

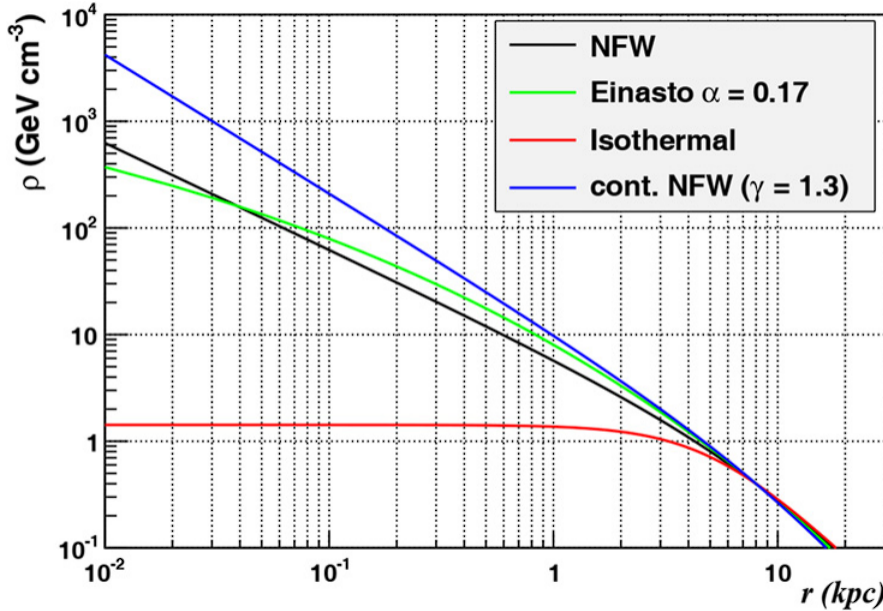


Figure 2.12 Different dark matter density profiles compared. Some models produce exceptionally large densities at small  $r$  [20].

513 astrophysical background. Unlike the galactic center, the most active components of dSph's are the  
 514 stars within them versus a violent accretion disc around a black hole. All this together means that  
 515 dSph's are among the best sources to look at for indirect DM searches. dSph's are the targets of  
 516 focus for this thesis.

## 517 2.6 Multi-Messenger Dark Matter

518 Astrophysics entered a new phase in the past few decades that leverages our increasing sensitivity  
 519 to SM channels and general relativity (GR). Up until the 21st century, astrophysical observations  
 520 were performed with photons ( $\gamma$ ) only. Astrophysics with this 'messenger' is fairly mature now.  
 521 Novel observations of the universe have since only adjusted the sensitivity of the wavelength of  
 522 light that is observed except at MeV energies. Gems like the CMB [10], and more have ultimately  
 523 been observations of different wavelengths of light. Multi-messenger astrophysics proposes using  
 524 other SM particles such the  $p^{+-}$ , or  $\nu$  or gravitation waves predicted by general relativity.

525 The experiment LIGO had a revolutionary discovery in 2016 with the first detection of a binary  
 526 black hole merger [21]. This opened the collective imagination to observing the universe through  
 527 gravitational waves. There has also been a surge of interest in the neutrino ( $\nu$ ) sector. IceCube

528 demonstrated that we are sensitive to neutrinos in regions that correlate with significant photon  
 529 emission like the galactic plane [22]. Neutrinos, like gravitational waves and light, travel mostly  
 530 unimpeded from their source to our observatories. This makes pointing to the originating source  
 531 of these messengers much easier than it is for cosmic rays which are deflected from their source by  
 532 magnetic fields.

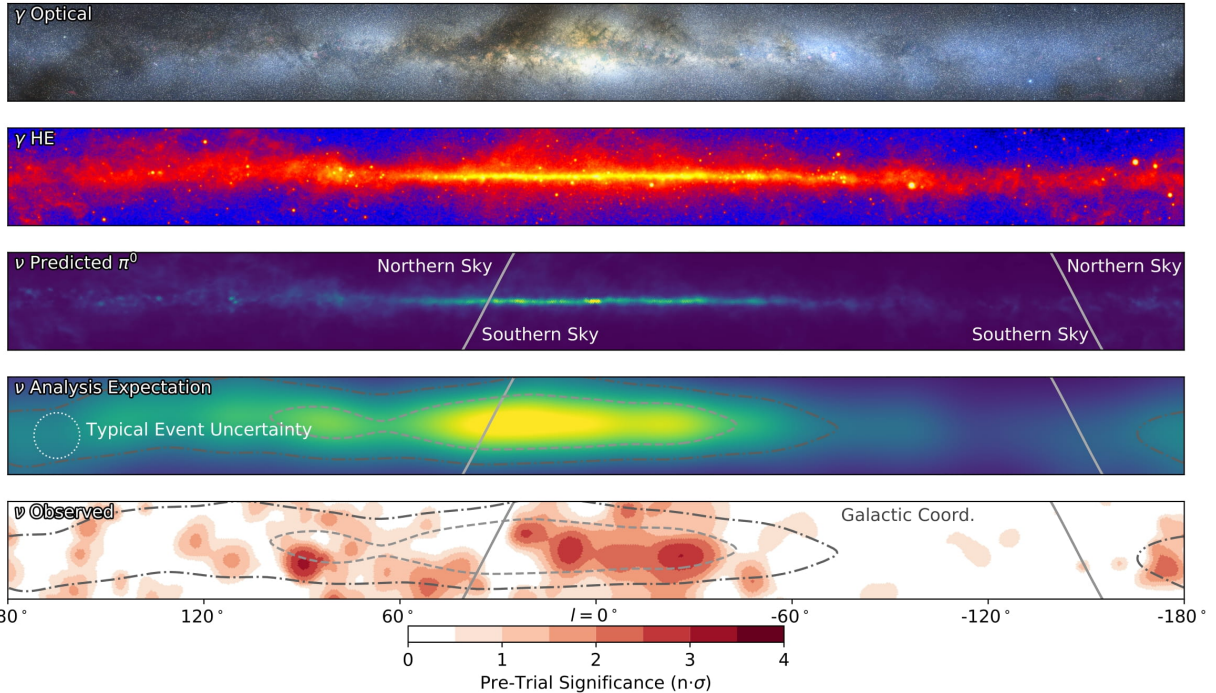


Figure 2.13 The Milky Way Galaxy in photons ( $\gamma$ ) and neutrinos ( $\nu$ ) [22]. The Galactic center is at  $l=0^\circ$  and is the brightest region in all panels. (top) An Optical color image of the Milky Way galaxy seen from Earth. Clouds of gas and dust obscure some light from stars. (2nd down) Integrated flux of  $\gamma$ -rays observed by the Fermi-LAT telescope [23]. (middle) Expected neutrino emission that corresponds with Fermi-LAT observations. (2nd up) Expected neutrino emission profile after considering detector systematics of IceCube. (bottom) Observed neutrino emission from region of the galactic plane. Substantial neutrino emission was detected.

533 The IceCube collaboration recently published a groundbreaking result of the Milky Way in  
 534 neutrinos. The recent result from IceCube, shown in Figure 2.13, proves that we can make  
 535 observations under different messenger regimes. The top two panels show the appearance of the  
 536 galactic plane to different wavelengths of light. Some sources are more apparent in some panels,  
 537 while others are not. This new channel is powerful because neutrinos are readily able to penetrate  
 538 through gas and dust in the Milky Way. This new image also refines our understanding of how high

539 energy particles are produced. For example, the fit to IceCube data prefers neutrino production  
 540 from the decay of  $\pi^0$  [22].

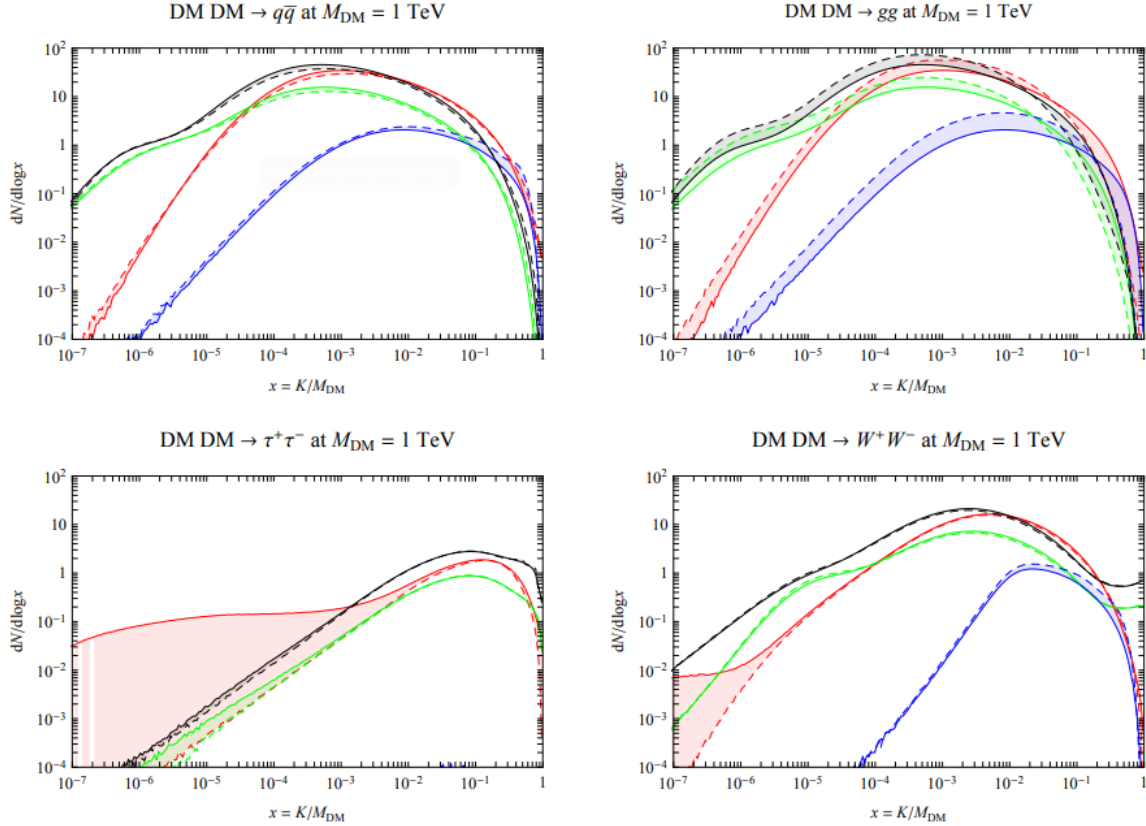


Figure 2.14 Dark Matter annihilation spectra for different final state particle and standard model annihilation channels [24]. Photons (red),  $e^\pm$  (green),  $\bar{p}$  (blue),  $\nu$  (black).

541 Exposing our observations to more cosmic messengers greatly increases our sensitivity to  
 542 rare processes. In the case of DM, Figure 2.14, there are many SM particles produced in DM  
 543 annihilation. Among the final state fluxes are gammas and neutrinos. Charged particles are also  
 544 produced however they would not likely make it to Earth since they will be deflected by magnetic  
 545 fields between the source and Earth. This means observatories that can see the neutral messengers  
 546 are especially good for DM searches and for combining data for a multi-messenger DM search.

## CHAPTER 3

### 547 MULTIMESSENGER ASTROPHYSICS: DETECTING HIGH ENERGY NEUTRAL 548 MESSENGERS

#### 549 3.1 Introduction

550 Before the 20th century, all asttrophysics observations were optical in nature. We litterly only  
551 saw things with highly magnified optical observations. Then we discovered cosmic rays. cosmic  
552 rays are charged particles, typically naked protons or H+. This was seen by Victor Hess in 19??.  
553 Around the same time we discovered neutrinos from beta decay. Sometime around 1950 we started  
554 to build neutrino detectors which were mostly sensitive to neutrinos from the sun. Finally, it was  
555 theorized that compact objects like black holes and neutron stars would create waves in space-time  
556 when they experience mergers or collisions.

557 In the 21st century, we have developed new observation techniques and detectors that are no only  
558 sensitive to these four messengers - photons ( TODO: photon), neutrinos ( TODO: nu), Cosmic  
559 Rays (CR), and Gravitational Wave (WV) - we're collect high energy versions of these events.  
560 For the standad model particles, we're now sensitive to all messengers above the MeV eneryg  
561 range. Additionally, the GW's were sensitive to are in the stellar mass black hole region and above  
562 within our galactic neighborhood. This means were becoming sensitive to the fundamental physics  
563 occuring within the universe and we can rely on the universe as a TeV+ particle accelerator. We  
564 also have the abaility to correlate high energy events across messengers and gain new insights on  
565 the processes that occur in our universe.

566 This thesis focuses on very high energy (VHE) gamma rays and neutrinos. These can both be  
567 observed through the water cherenkov detection technique altho not exclusively. Methods on how  
568 to detect and observe these neutral messengers are discussed Section 3.3 and Section 3.4

#### 569 3.2 Charged Particles in a Medium

570 For high enery gamma-rays and neutrinos, we can exploit the same effect that charged particles  
571 have with water. This effect is known as Cherenkov radiation. Cherenkov Radiation occurs when a  
572 charged particle, usually electrons ( $e$ ) or muons ( $\mu$ ), traverse a medium, like water, faster than the

573 speed of light in that medium. This is similar to sonic boom where an object moves through air  
574 faster than the speed of sound in air. Cherenkov radiation can therefore be thought of as an 'optic  
575 boom'. Many astro-particle physics experiments will use water as the medium as because water  
576 has a unique set of properties ideal for charged particle tracking.



Figure 3.1 TODO: Show a nuclear reactor with cherenkov radiation[NEEDS A SOURCE][FACT CHECK THIS]

577 The frequency of light emitted due to cherenkov radiation follows the equation:

$$INSERT\ Cherenkov\ wavelength\ calc\ HERE. \quad (3.1)$$

578 The absorption spectra is shown in the following figure:

579 **3.3 Photons ( $\gamma$ )**

580 **3.4 Neutrinos ( $\nu$ )**

581 **3.5 Opportunities to Combine for Dark Matter**



Figure 3.2 TODO: absorption spectrum of liquid and solid water[NEEDS A SOURCE][FACT CHECK THIS]

## CHAPTER 4

582                   **HIGH ALTITUDE WATER CHERENKOV (HAWC) OBSERVATORY**

583   **4.1 The Detector**

584   **4.2 Events Reconstruction and Data Acquisition**

585    **4.2.1 G/H Discrimination**

586    **4.2.2 Angle**

587    **4.2.3 Energy**

588   **4.3 Remote Monitoring**

589    **4.3.1 ATHENA Database**

590    **4.3.2 HOMER**

591

## CHAPTER 5

### ICECUBE NEUTRINO OBSERVATORY

592 **5.1 The Detector**

593 **5.2 Events Reconstruction and Data Acquisition**

594 **5.2.1 Angle**

595 **5.2.2 Energy**

596 **5.3 Northern Test Site**

597 **5.3.1 PIgeon remote dark rate testing**

598 **5.3.2 Bulkhead Construction**

## CHAPTER 6

### COMPUTATIONAL TECHNIQUES IN PARTICLE ASTROPHYSICS

600 **6.1 Neural Networks for Gamma/Hadron Separation**

601 **6.2 Parallel Computing for Dark Matter Analyses**

## CHAPTER 7

### GLORY DUCK: MULTI-WAVELENGTH SEARCH FOR DARK MATTTER ANNIHILATION TOWARDS DWARF SPHEROIDAL GALAXIES

#### 7.1 Introduction

The field of astrophysics now has several instruments and observatories sensitive to high energy gamma-rays. The energy sensitivity for the modern gamma-ray program spans many orders of magnitude. Figure 7.1 demonstrates these similar sensitivities across energies for the five experiments: Fermi-LAT, HAWC, HESS, MAGIC, and VERITAS.

Each of the five experiments featured in Figure 7.1 have independently searched for DM annihilation from dwarf spheroidal galaxies (dSph) and set limits. Intriguingly, there are regions of substantial overlap in their energy sensitivities. This clearly motivates an analysis that combines data from these five. Each experiment has unique gamma-ray detection methods and their weaknesses and strengths can be leveraged with each other. The HAWC gamma-ray observatory is extensively introduced in chapter 4, so it is not introduced here. A brief description of the remaining experiments are in the following paragraphs.

The Large Area Telescope (LAT) is a pair conversion telescope mounted on the NASA Fermi satellite in orbit  $\sim$ 550 km above the Earth [25]. LAT's field of view covers about 20% of the whole sky, and it sweeps the whole sky approximately every 3 hours. LAT's gamma-ray energy sensitivity ranges from 20 MeV up to 1 TeV. Previous DM searches towards dSphs using Fermi-LAT are published in [26] and [27]

The High Energy Spectroscopic System (HESS), Major Atmospheric Gamma Imaging Cherenkov (MAGIC), and Very Energetic Radiation Imaging Telescope Array System (VERITAS) are arrays of Imaging Atmospheric Cherenkov Telescopes (IACT). These telescopes observe the Cherenkov light emitted from gamma-ray showers in the Earth's atmosphere. The field of view for these telescopes is no larger than  $5^\circ$  with energy sensitivities ranging from 30 GeV up to 100 TeV [28, 29, 30]. IACTs are able to make precise observations in selected regions of the sky, however can only be operated in ideal dark conditions. HESS's observations of the dwarves

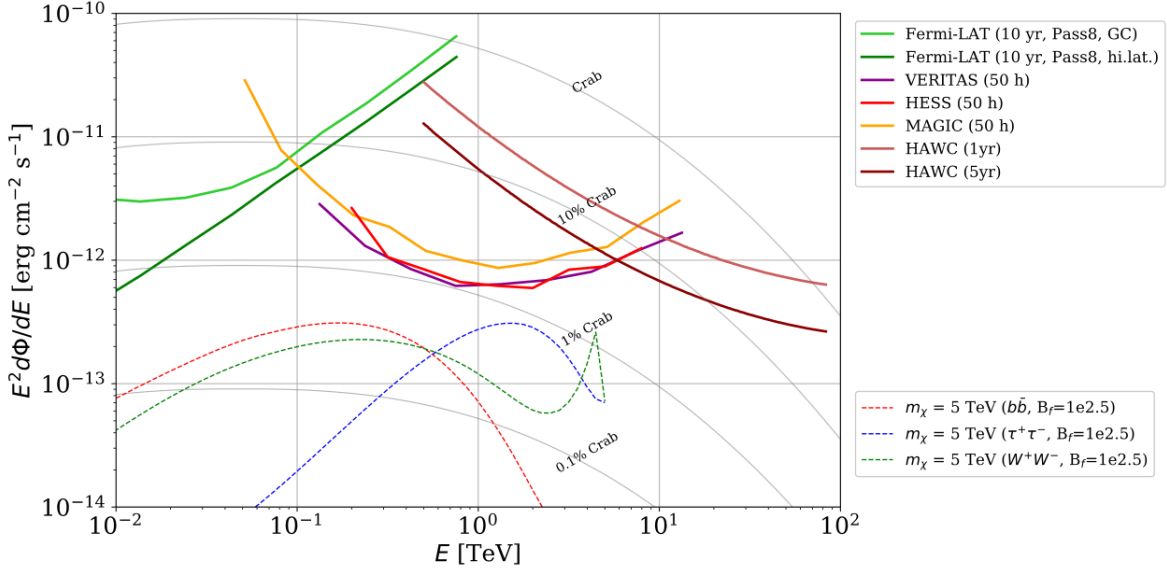


Figure 7.1 [NEEDS A SOURCE] Sensitivities of five gamma-ray experiments compared to percentages of the Crab nebula’s emission and dark matter annihilation. Solid lines present estimated sensitivities to power law spectra [FACT CHECK THIS] for each experiment. Green lines are Fermi-LAT sensitivities where lighter green is the sensitivity to the galactic center and dark green is its sensitivity to higher declinations. Orange, red, and purple solid lines represent the MAGIC, HESS, and VERITAS 50 hour sensitivities respectively. The maroon and brown lines are the HAWC 1 year and 5 year sensitivities. Across four decades of gamma-ray energy, these experiments have similar sensitivities on the order  $10^{-12}$  erg cm $^{-2}$ s $^{-1}$ . The dotted lines are estimated dark matter fluxes assuming  $m_\chi = 5$  TeV DM annihilating to bottom quarks (red), tau leptons (blue), and W bosons (green). Faded gray lines outline percentage flux of the Crab nebula.

628 Sculptor and Carina were between January 2008 and December 2009. HESS’s observations of  
 629 Coma Berenices were from 2010 to 2013, and Fornax was observed in 2010 [31, 32, 33]. MAGIC  
 630 provided deep observations of Segue1 between 2011 and 2013 [34]. MAGIC also provides data  
 631 for three dwarves: Coma Berenices, Draco, and Ursa Major II where observations were made  
 632 in: January - June 2019 [35], March - September 2018 [35], and 2014 - 2016 [36] respectively.  
 633 VERITAS provided data for Boötes I, Draco, Segue 1, and Ursa Minor from 2009 to 2016 [37].

634 This chapter presents the Glory Duck analysis, the name given for the search for dark matter  
 635 annihilation from dSph by combining data from the five gamma-ray observatories: Fermi-LAT,  
 636 HAWC, HESS, MAGIC, and VERITAS. Specifically, the methods in analysis and modeling are  
 637 presented for the HAWC gamma-ray observatory. This work was published to the Journal of  
 638 Cosmology and Astroparticle Physics and presented at the International Cosmic Ray Conference

639 in 2019, 2021, and 2023 [38, 39, 40] and others.

640 **7.2 Dataset and Background**

641 This section enumerates the data and background methods used for HAWC’s study of dSphs.  
642 Section 7.2.1 and Section 7.2.2 are most useful for fellow HAWC collaborators looking to replicate  
643 the Glory Duck analysis.

644 **7.2.1 Itemized HAWC files**

- 645 • Detector Resolution: `response_aerie_svn_27754_systematics_best_mc_test_no`  
646 `broadpulse\_10pctlogchargesmearing_0.63qe_25kHzNoise_run5481_curvatu`  
647 `re0_index3.root`
- 648 • Data Map: `maps-20180119/liff/maptree_1024.root`
- 649 • Spectral Dictionary: `DM_CirrelliSpectrum_dict_gammas.npy`
- 650 • Analysis wiki: [https://private.hawc-observatory.org/wiki/index.php/Glory\\_Duck\\_Multi-Experiment\\_Dark\\_Matter\\_Search](https://private.hawc-observatory.org/wiki/index.php/Glory_Duck_Multi-Experiment_Dark_Matter_Search)

652 **7.2.2 Software Tools and Development**

653 This analysis was performed using HAL and 3ML [41, 42] in Python version 2. I built software  
654 to implement the *A Poor Particle Physicist Cookbook for Dark Matter Indirect Detection* (PPPC)  
655 [43] DM spectral model and dSphs spatial model from [44] for HAWC analysis. A NumPy version  
656 of this dictionary was made for both Py2 and Py3. The code base for creating this dictionary is  
657 linked on my GitLab sandbox:

- 658 • Py2: [Dictionary Generator \(Deprecated\)](#)
- 659 • Py3: [PPPC2Dict](#)

660 The analysis was performed using the  $f_{\text{hit}}$  framework performed in the HAWC Crab paper  
661 [41]. The Python2 NumPy dictionary file for gamma-ray final states is `dmCirSpecDict.npy`. The  
662 corresponding Python3 file is `DM_CirrelliSpectrum_dict_gammas.npy`. These files can also

663 be used for decay channels and the PPPC describes how [43]. All other software used for data  
664 analysis, DM profile generation, and job submission to SLURM are also kept in my sandbox for  
665 [the Glory Duck](#) project.

666 **7.2.3 Data Set and Background Description**

667 The HAWC data maps used for this analysis contain 1017 days of data between runs 2104  
668 (2014-11-26) and 7476 (2017-12-20). They were generated from pass 4.0 reconstruction. The  
669 analysis is performed using the  $f_{hit}$  energy binning scheme with bins (1-9) similar to what was done  
670 for the Crab and previous HAWC dSph analysis [41, 45]. Bin 0 was excluded as it has substantial  
671 hadronic contamination and poor angular resolution.

672 This analysis was done on dSphs because of their large DM mass content relative to baryonic  
673 mass. We consider the following to estimate the background to this study.

- 674 • The dSphs are small in HAWC’s field of view, so the analysis is not sensitive to large or small  
675 scale anisotropies.
- 676 • The dSphs used in this analysis are off the galactic plane.
- 677 • The dSphs are baryonically faint relative to their expected dark matter content and are not  
678 expected to contain high energy gamma-ray sources.

679 Therefor we make no additional assumptions on the background from our sources and use  
680 HAWC’s standard direct integration method for background estimation [41]. It is possible for  
681 gamma rays from DM annihilation to scatter in transit to HAWC via Inverse Compton Scattering  
682 (ICS). This was investigated and its impact on the flux is basically zero. Supporting information  
683 on this is in Section 7.7.1

684 **7.3 Analysis**

685 The expected differential photon flux from DM-DM annihilation to standard model particles,  
686  $d\Phi_\gamma/dE_\gamma$ , over solid angle,  $\Omega$  is described by the familiar equation.

$$\frac{d\Phi_\gamma}{dE_\gamma} = \frac{\langle\sigma v\rangle}{8\pi m_\chi^2} \frac{dN_\gamma}{dE_\gamma} \times \int_{\text{source}} d\Omega \int_{l.o.s} \rho_\chi^2 dl(r, \theta') \quad (7.1)$$

687 Where  $\langle \sigma v \rangle$  is the velocity weighted annihilation cross-section.  $\frac{dN}{dE}$  is the expected differential  
 688 number of photons produced at each energy per annihilation.  $m_\chi$  is the rest mass of the supposed  
 689 DM particle.  $\rho_\chi$  is the DM density.  $J$  is the astrophysical J-factor and is defined as

$$J = \int d\Omega \int_{l.o.s} dl \rho_\chi^2(r, \theta') \quad (7.2)$$

690  $l$  is the distance to the source from Earth.  $r$  is the radial distance from the center of the source.  $\theta'$  is  
 691 the half angle defining a cone containing the DM source. How each component is synthesized and  
 692 considered for HAWC's analysis is presented in the following sections. Section 7.3.1 presents the  
 693 particle physics model for DM annihilation. Section 7.3.2 presents the spatial distributions built  
 694 for each dSph.

### 695 7.3.1 $\frac{dN_\gamma}{dE_\gamma}$ - Particle Physics Component

696 For these spectra, we import the PPPC with Electroweak (EW) corrections [43]. The spectrum  
 697 is implemented as a model script in astromodels for 3ML. The EW corrections were previously not  
 698 considered for HAWC and are significant for DM annihilating to EW coupled SM particles such  
 699 as all leptons, and the  $\gamma$ ,  $Z$ , and  $W$  bosons [45]. Figure 7.2 demonstrates the significance of EW  
 700 corrections for W boson annihilation. Across EW SM channels, the gamma-ray spectra become  
 701 harder than spectra without EW corrections. Tables from the PPPC were reformatted into Python  
 702 NumPy dictionaries for collaboration-wide use. A class in astromodels was developed to include  
 703 the EW correction from the PPPC and is aptly named `PPPCSpectra` within `DM_models.py`.

### 704 7.3.2 $J$ - Astrophysical Component

705 The J-factor profiles for each source are imported from Geringer-Sameth (referred to with  $\mathcal{GS}$ )  
 706 [44]. These were pulled from the publication as  $J(\theta)$ , where  $\theta$  is the angular separation from the  
 707 center of the source. HAWC requires maps in terms of  $\frac{dJ}{d\Omega}$ , so the conversion from the maps was  
 708 done in the following way...

709 First, convert the angular distances to solid angles

$$\Omega = 2 \cdot \pi(1 - \cos(\theta)) \quad (7.3)$$

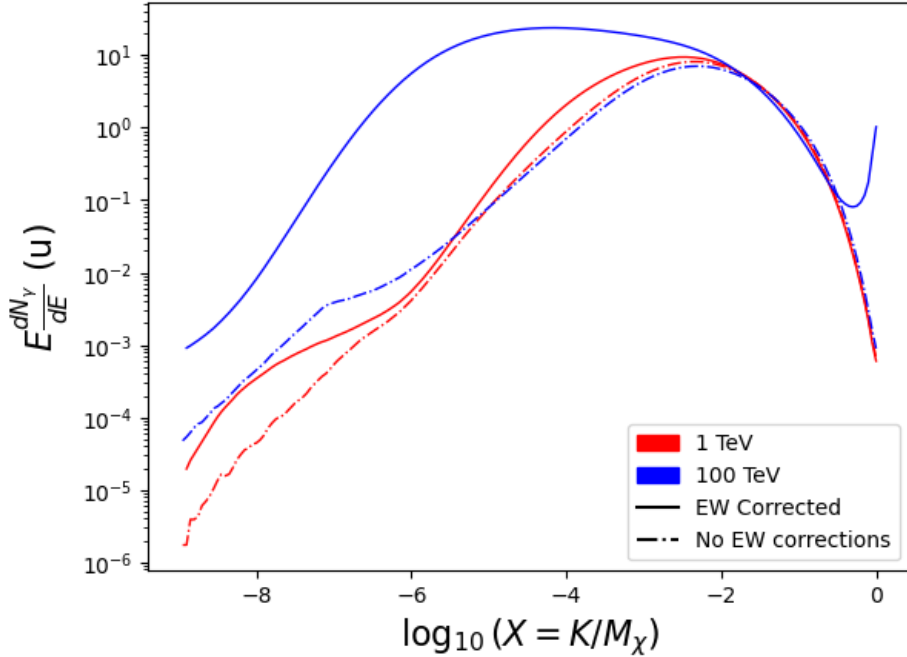


Figure 7.2 Effect of Electro-Weak (EW) corrections on expected DM annihilation spectrum for  $\chi\chi \rightarrow W^-W^+$ . Solid lines are spectral models that consider EW corrections. Dash-dot lines are spectral models without EW corrections. Red lines are models for  $M_\chi = 1$  TeV. Blue lines represent models for  $M_\chi = 100$  TeV. All models are sourced from the PPPC4DMID [43].

710 which reduces with a small angle approximation to  $\pi\theta^2$ . Next, the central difference for both the  
 711  $\Delta J$  and  $\Delta\Omega$  value were calculated from the discretized  $J(\theta)$  with the central difference stencil:

$$\Delta\phi_i = \phi_{i+1} - \phi_{i-1} \quad (7.4)$$

712 Where  $\phi$  is either  $\Omega$  or  $J$ . These were done separately in case the grid spacing in  $\theta$  was not uniform.  
 713 Finally, these lists are divided so that we are left with an approximation of the  $dJ/d\Omega$  profile that  
 714 is a function of  $\theta$ . Admittedly, this is an approximation method for the map which introduces small  
 715 errors compared to the true profile estimate. This was checked as a systematic against the author's  
 716 profiling of the spatial distribution and is documented in Section 7.8.1.

717 With  $\frac{dJ}{d\Omega}(\theta)$ , a map is generated, first by filling in the north-east quadrant of the map. This  
 718 quadrant is then reflected twice, vertically then horizontally, to fill the full map. Maps are then  
 719 normalized by dividing the discrete 2D integral of the map. The 2D integral was a simple height

720 of bins, Newton’s integral:

$$p^2 \cdot \sum_{i,j=0}^{N,M} \frac{dJ}{d\Omega}(\theta_{i,j}) \quad (7.5)$$

721 These maps are HEALpix maps with NSIDE 16384 and saved in the `.fits` format.

722 Another DM spatial distribution model from Bonnivard ( $\mathcal{B}$ ) [46] was used for the Glory Duck  
723 study. However, to save computational time, limits from  $\mathcal{GS}$  were scaled to  $\mathcal{B}$  instead of each  
724 experiment performing a full study a second time. How these models compare is demonstrated  
725 for each dSph in Figure 7.15 and Figure 7.16 Plots of these maps are provided for each source  
726 in chapter A Examples of the two most impactful dSphs derived from  $\mathcal{GS}$ , Segue1 and Coma  
727 Berenices are featured in Figure 7.3

### 728 7.3.3 Source Selection and Annihilation Channels

729 We use many of the dSphs presented in HAWC’s previous dSph DM search [45]. HAWC’s  
730 sources for Glory Duck include Boötes I, Coma Berenices, Canes Venatici I + II, Draco, Hercules,  
731 Leo I, II, + IV, Segue 1, Sextans, and Ursa Major I + II. A full description of all sources used  
732 in Glory Duck is found in Table 7.1. Triangulum II was excluded from the Glory Duck analysis  
733 because of large uncertainties in its  $J$  factor. Ursa Minor was excluded from HAWC’s contribution  
734 to the combination because the source extension model extended Ursa Minor beyond HAWC’s field  
735 of view. Ursa Minor was not expected to contribute significantly to the combined limit, so work  
736 was not invested in a solution to include Ursa Minor.

737 This analysis improves on the previous HAWC dSph paper [45] in the following ways. Pre-  
738 viously, the dSphs were treated and implemented as point sources. For this analysis, dSphs are  
739 modeled and treated as extended source. The impact of this change with respect to the upper limit  
740 is source dependant and is explored in Section 7.7.2. Previously, the particle physics model used for  
741 gamma-ray spectra from DM annihilation did not have EW corrections where the PPPC includes  
742 them. Finally, the gamma-ray dataset is much larger. The study performed here analyzes over  
743 1000 days of data compared to 507.

744 The SM annihilation channels probed for the Glory Duck combination include  $b\bar{b}$ ,  $e\bar{e}$ ,  $\mu\bar{\mu}$ ,  $\tau\bar{\tau}$ ,  
745  $t\bar{t}$ ,  $W^+W^-$ , and  $ZZ$ . A summary of all sources, with a description of each experiments’ sensitivity

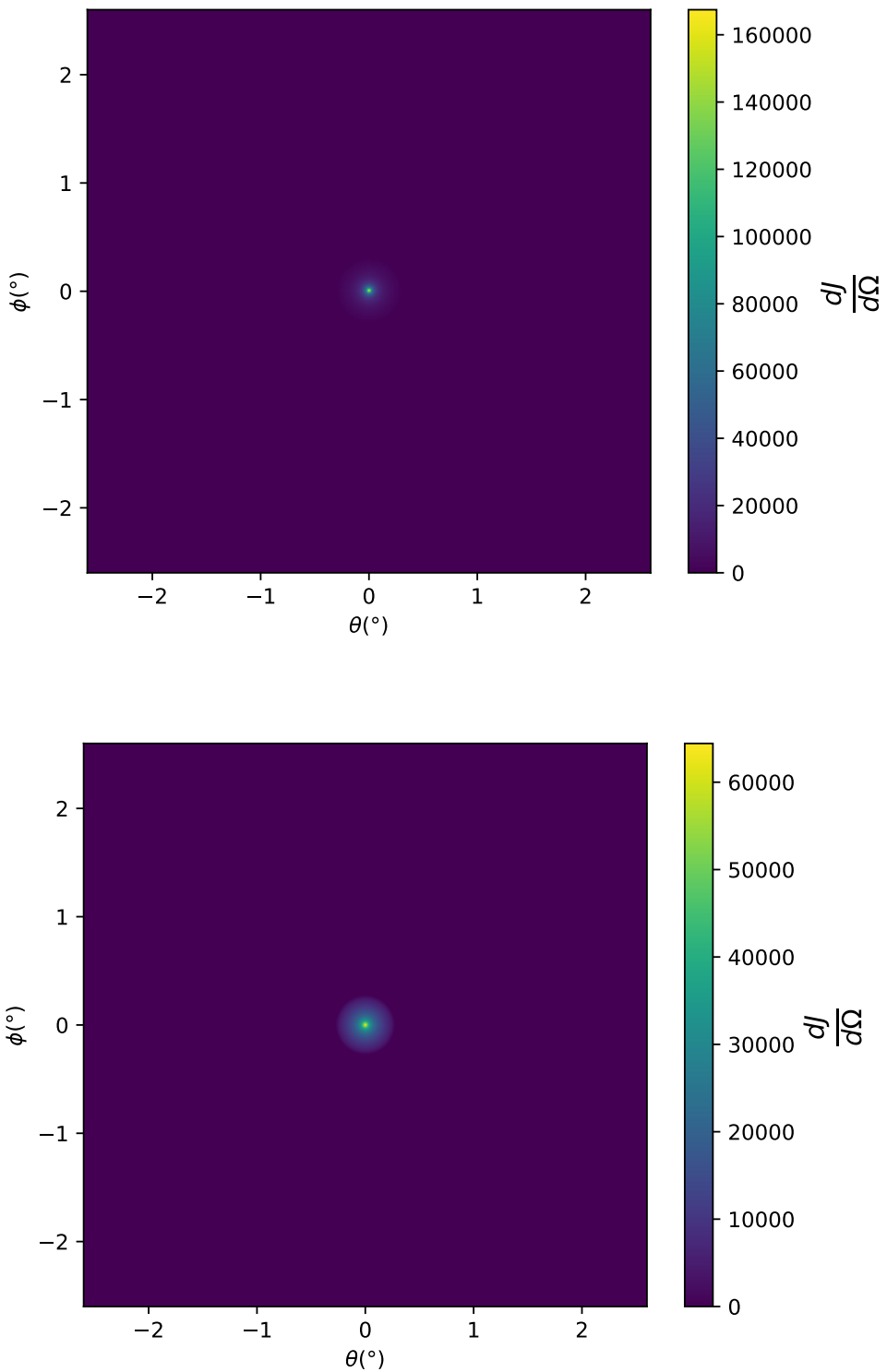


Figure 7.3  $\frac{dJ}{d\Omega}$  maps for Segue1 (top) and Coma Berenices (bottom). Origin is centered on the specific dwarf spheroidal galaxies (dSph). X and Y axes are the angular separation from the center of the dwarf. Plots of the remaining 11 dSph HAWC studied are linked in Fig. A.1.

Table 7.1 Summary of the relevant properties of the dSphs used in the present work. Column 1 lists the dSphs. Columns 2 and 3 present their heliocentric distance and galactic coordinates, respectively. Columns 4 and 5 report the  $J$ -factors of each source given from the  $\mathcal{GS}$  and  $\mathcal{B}$  independent studies and their estimated  $\pm 1\sigma$  uncertainties. The values  $\log_{10} J$  ( $\mathcal{GS}$  set) [44] correspond to the mean  $J$ -factor values for a source extension truncated at the outermost observed star. The values  $\log_{10} J$  ( $\mathcal{B}$  set) [46] are provided for a source extension at the tidal radius of each dSph. **Bolded sources are within HAWC's field of view and provided to the Glory Duck analysis.**

Name	Distance (kpc)	$l, b$ ( $^{\circ}$ )	$\log_{10} J$ ( $\mathcal{GS}$ set) $\log_{10}(\text{GeV}^2 \text{cm}^{-5} \text{sr})$	$\log_{10} J$ ( $\mathcal{B}$ set) $\log_{10}(\text{GeV}^2 \text{cm}^{-5} \text{sr})$
<b>Boötes I</b>	66	358.08, 69.62	$18.24^{+0.40}_{-0.37}$	$18.85^{+1.10}_{-0.61}$
<b>Canes Venatici I</b>	218	74.31, 79.82	$17.44^{+0.37}_{-0.28}$	$17.63^{+0.50}_{-0.20}$
<b>Canes Venatici II</b>	160	113.58, 82.70	$17.65^{+0.45}_{-0.43}$	$18.67^{+1.54}_{-0.97}$
Carina	105	260.11, -22.22	$17.92^{+0.19}_{-0.11}$	$18.02^{+0.36}_{-0.15}$
<b>Coma Berenices</b>	44	241.89, 83.61	$19.02^{+0.37}_{-0.41}$	$20.13^{+1.56}_{-1.08}$
<b>Draco</b>	76	86.37, 34.72	$19.05^{+0.22}_{-0.21}$	$19.42^{+0.92}_{-0.47}$
Fornax	147	237.10, -65.65	$17.84^{+0.11}_{-0.06}$	$17.85^{+0.11}_{-0.08}$
<b>Hercules</b>	132	28.73, 36.87	$16.86^{+0.74}_{-0.68}$	$17.70^{+1.08}_{-0.73}$
<b>Leo I</b>	254	225.99, 49.11	$17.84^{+0.20}_{-0.16}$	$17.93^{+0.65}_{-0.25}$
<b>Leo II</b>	233	220.17, 67.23	$17.97^{+0.20}_{-0.18}$	$18.11^{+0.71}_{-0.25}$
<b>Leo IV</b>	154	265.44, 56.51	$16.32^{+1.06}_{-1.70}$	$16.36^{+1.44}_{-1.65}$
Leo V	178	261.86, 58.54	$16.37^{+0.94}_{-0.87}$	$16.30^{+1.33}_{-1.16}$
Leo T	417	214.85, 43.66	$17.11^{+0.44}_{-0.39}$	$17.67^{+1.01}_{-0.56}$
Sculptor	86	287.53, -83.16	$18.57^{+0.07}_{-0.05}$	$18.63^{+0.14}_{-0.08}$
<b>Segue I</b>	23	220.48, 50.43	$19.36^{+0.32}_{-0.35}$	$17.52^{+2.54}_{-2.65}$
Segue II	35	149.43, -38.14	$16.21^{+1.06}_{-0.98}$	$19.50^{+1.82}_{-1.48}$
<b>Sextans</b>	86	243.50, 42.27	$17.92^{+0.35}_{-0.29}$	$18.04^{+0.50}_{-0.28}$
<b>Ursa Major I</b>	97	159.43, 54.41	$17.87^{+0.56}_{-0.33}$	$18.84^{+0.97}_{-0.43}$
<b>Ursa Major II</b>	32	152.46, 37.44	$19.42^{+0.44}_{-0.42}$	$20.60^{+1.46}_{-0.95}$
Ursa Minor	76	104.97, 44.80	$18.95^{+0.26}_{-0.18}$	$19.08^{+0.21}_{-0.13}$

746 to the source, is provided in Table 7.2.

## 747 7.4 Likelihood Methods

### 748 7.4.1 HAWC Likelihoods

749 For every analysis bin in energy,  $f_{hit}$  bins (1-9), and location, we can expect  $N$  signal events and  
 750  $B$  background events. The expected number of excess signal events from dark matter annihilation,

Table 7.2 Summary of dSph observations by each experiment used in this work. A ‘-’ indicates the experiment did not observe the dSph for this study. For Fermi-LAT, the exposure at 1 GeV is given. For HAWC,  $|\Delta\theta|$  is the absolute difference between the source declination and HAWC latitude. HAWC is more sensitive to sources with smaller  $|\Delta\theta|$ . For IACTs, we show the zenith angle range, the total exposure, the energy range, the angular radius  $\theta$  of the signal or ON region, the ratio of exposures between the background-control (OFF) and signal (ON) regions ( $\tau$ ), and the significance of gamma-ray excess in standard deviations,  $\sigma$ .

Source name	Fermi-LAT	HAWC	H.E.S.S, MAGIC, VERITAS						
	Exposure ( $10^{11}$ s m $^2$ )	$ \Delta\theta $ ( $^\circ$ )	IACT	Zenith ( $^\circ$ )	Exposure (h)	Energy range (GeV)	$\theta$ ( $^\circ$ )	$\tau$	$S$ ( $\sigma$ )
Boötes I	2.6	4.5	VERITAS	15 – 30	14.0	100–41000	0.10	8.6	-1.0
Canes Venatici I	2.9	14.6	–	–	–	–	–	–	–
Canes Venatici II	2.9	15.3	–	–	–	–	–	–	–
Carina	3.1	–	H.E.S.S.	27 – 46	23.7	310 – 70000	0.10	18.0	-0.3
Coma Berenices	2.7	4.9	H.E.S.S.	47 – 49	11.4	550 – 70000	0.10	14.4	-0.4
Draco	3.8	38.1	MAGIC	5 – 37	49.5	60 – 10000	0.17	1.0	–
			MAGIC	29 – 45	52.1	70 – 10000	0.22	1.0	–
			VERITAS	25 – 40	49.8	120 – 70000	0.10	9.0	-1.0
Fornax	2.7	–	H.E.S.S.	11 – 25	6.8	230 – 70000	0.10	45.5	-1.5
Hercules	2.8	6.3	–	–	–	–	–	–	–
Leo I	2.5	6.7	–	–	–	–	–	–	–
Leo II	2.6	3.1	–	–	–	–	–	–	–
Leo IV	2.4	19.5	–	–	–	–	–	–	–
Leo V	2.4	–	–	–	–	–	–	–	–
Leo T	2.6	–	–	–	–	–	–	–	–
Sculptor	2.7	–	H.E.S.S.	10 – 46	11.8	200 – 70000	0.10	19.8	-2.2
Segue I	2.5	2.9	MAGIC	13 – 37	158.0	60 – 10000	0.12	1.0	-0.5
			VERITAS	15 – 35	92.0	80 – 50000	0.10	7.6	0.7
Segue II	2.7	–	–	–	–	–	–	–	–
Sextans	2.4	20.6	–	–	–	–	–	–	–
Ursa Major I	3.4	32.9	–	–	–	–	–	–	–
Ursa Major II	4.0	44.1	MAGIC	35 – 45	94.8	120 – 10000	0.30	1.0	-2.1
Ursa Minor	4.1	–	VERITAS	35 – 45	60.4	160 – 93000	0.10	8.4	-0.1

751  $S$ , is estimated by convolving Equation (7.1) with HAWC's energy response and pixel point spread  
 752 functions. I then compute the test statistic (TS) with the log-likelihood ratio test,

$$\text{TS} = -2 \ln \left( \frac{\mathcal{L}_0}{\mathcal{L}^{\max}} \right) \quad (7.6)$$

754 where  $\mathcal{L}_0$  is the null hypothesis, or no DM emission, likelihood.  $\mathcal{L}^{\max}$  is the best fit signal  
 755 hypothesis where  $\langle \sigma v \rangle$  maximizes the likelihood. We calculate the likelihood of each source and  
 756 model, assuming events are Poisson distributed, with

$$\mathcal{L} = \prod_i \frac{(B_i + S_i)^{N_i} e^{-(B_i + S_i)}}{N_i!} \quad (7.7)$$

757 where  $S_i$  is the sum of expected number of signal counts.  $B_i$  is the number of background counts  
 758 observed.  $N_i$  is the total number of counts.

759 I also calculate an upper limit on  $\langle \sigma v \rangle$  by calculating the 95% confidence level (CL). For the  
 760 CL, we define a parameter,  $TS_{95}$ , as

$$TS_{95} \equiv \sum_{\text{bins}} \left[ 2N \ln \left( 1 + \frac{\epsilon S_{\text{ref}}}{B} \right) - 2\epsilon S_{\text{ref}} \right] \quad (7.8)$$

761 where the expected signal counts from a dSph is scaled by  $\epsilon$ .  $S_{\text{ref}}$  is the expected number of excess  
 762 counts in a bin from DM emission from a dSph with a corresponding annihilation cross-section,  
 763  $\langle \sigma v \rangle$ . We scan  $\epsilon$  such that

$$2.71 = TS_{\max} - TS_{95} \quad (7.9)$$

#### 764 7.4.2 Glory Duck Joint Likelihood

765 The joint likelihood for the 5-experiment combination was done similarly as Section 7.4.1.  
 766 We calculate upper limits on  $\langle \sigma v \rangle$  from the TS, Eq. (7.18), and define the likelihood ratio more  
 767 generally

$$\lambda(\langle \sigma v \rangle | \mathcal{D}_{\text{dSphs}}) = \frac{\mathcal{L}(\langle \sigma v \rangle; \hat{\nu} | \mathcal{D}_{\text{dSphs}})}{\mathcal{L}(\widehat{\langle \sigma v \rangle}; \hat{\nu} | \mathcal{D}_{\text{dSphs}})} \quad (7.10)$$

768  $\mathcal{D}_{\text{dSphs}}$  is the totality of observations across experiments and dSphs.  $\nu$  are the nuisance parameters  
 769 which are the  $J$  factors in this study.  $\widehat{\langle \sigma v \rangle}$  and  $\hat{\nu}$  are the respective estimate that maximize  $\mathcal{L}$   
 770 globally. Finally,  $\hat{\nu}$  is the set of nuisance parameters that maximize  $\mathcal{L}$  for a fixed value of  $\langle \sigma v \rangle$ .

771 The *complete* joint likelihood,  $\mathcal{L}$  that encompasses all observations from all instruments and  
 772 dSphs can be factorized into *partial* functions for each dSph  $l$  (with  $\mathcal{L}_{\text{dSph},l}$ ) and its  $J$  factor ( $\mathcal{J}_l$ ):

$$\mathcal{L}(\langle\sigma v\rangle; \nu | \mathcal{D}_{\text{dSphs}}) = \prod_{l=1}^{N_{\text{dSphs}}} \mathcal{L}_{\text{dSph},l}(\langle\sigma v\rangle; J_l, \nu_l | \mathcal{D}_l) \times \mathcal{J}_l(J_l | J_{l,\text{obs}}, \sigma_{\log J_l}). \quad (7.11)$$

773 For this study,  $N_{\text{dSphs}} = 20$  is the number of dSphs studied.  $\mathcal{D}_l$  are the gamm-ray observations  
 774 of dSph,  $l$ .  $\nu_l$  are the nuisance parameters modifying the gamma-ray observations of dSph,  $l$ ,  
 775 but excludes  $\mathcal{J}_l$ .  $\mathcal{J}_l$  is the  $J$  factor for dSph,  $l$ , as defined in Equation (7.2), and it is a nuisance  
 776 parameter whose value is unknown.  $\log_{10} J_{l,\text{obs}}$  and  $\sigma_{\log J_l}$  are obtained from fitting a log-normal  
 777 function of  $J_{l,\text{obs}}$  to the posterior distribution of  $J_l$  [47].  $\log_{10} J_{l,\text{obs}}$  and  $\sigma_{\log J_l}$  values are provided  
 778 in Table 7.1. The term  $\mathcal{J}_l$  constraining  $J_l$  is written as:

$$\mathcal{J}_l(J_l | J_{l,\text{obs}}, \sigma_{\log J_l}) = \frac{1}{\ln(10)J_{l,\text{obs}}\sqrt{2\pi}\sigma_{\log J_l}} \exp\left(-\frac{(\log_{10} J_l - \log_{10} J_{l,\text{obs}})^2}{2\sigma_{\log J_l}^2}\right). \quad (7.12)$$

779 Both the  $\mathcal{GS}$  and  $\mathcal{B}$ , displayed in Table 7.1, sets of  $J$  factors are used in this analysis. Equation (7.12)  
 780 is also normalized, so it can also be interpreted as a probability density function (PDF) for  $J_{l,\text{obs}}$ .  
 781 From Equation (7.1), we can also see that  $\langle\sigma v\rangle$  and  $J_l$  are degenerate when computing  $\mathcal{L}_{\text{dSph},l}$ .  
 782 Therefore, as noted in [48], it is sufficient to compute  $\mathcal{L}_{\text{dSph},l}$  versus  $\langle\sigma v\rangle$  for a fixed value of  $J_l$ .  
 783 We used  $J_{l,\text{obs}}(\mathcal{GS})$  reported in Tab. 7.1, in order to perform the profile of  $\mathcal{L}$  with respect to  $J_l$ .  
 784 The degeneracy implies that for any  $J'_l \neq J_{l,\text{obs}}$  (in practice in our case we used  $J'_l = J_{l,\text{obs}}(\mathcal{B})$  to  
 785 compute results from a different set of  $J$  factors):

$$\mathcal{L}_{\text{dSph},l}(\langle\sigma v\rangle; J'_l, \nu_l | \mathcal{D}_l) = \mathcal{L}_{\text{dSph},l}\left(\frac{J'_l}{J_{l,\text{obs}}}\langle\sigma v\rangle; J_{l,\text{obs}}, \nu_l | \mathcal{D}_l\right), \quad (7.13)$$

786 which is a straightforward rescaling operation that reduces the computational needs of the profiling  
 787 operation since:

$$\mathcal{L}(\langle\sigma v\rangle; \hat{\nu} | \mathcal{D}_{\text{dSphs}}) = \prod_{l=1}^{N_{\text{dSphs}}} \max_{J_l} \left[ \mathcal{L}_{\text{dSph},l}(\langle\sigma v\rangle; J_l, \hat{\nu}_l | \mathcal{D}_l) \times \mathcal{J}_l(J_l | J_{l,\text{obs}}, \sigma_{\log J_l}) \right]. \quad (7.14)$$

788 In addition, Eq. (7.13) enables the combination of data from different gamma-ray instruments and  
 789 observed dSphs via tabulated values of  $\mathcal{L}_{\text{dSph},l}$ , or equivalently of  $\lambda$  from Eq. (7.10) as was done in

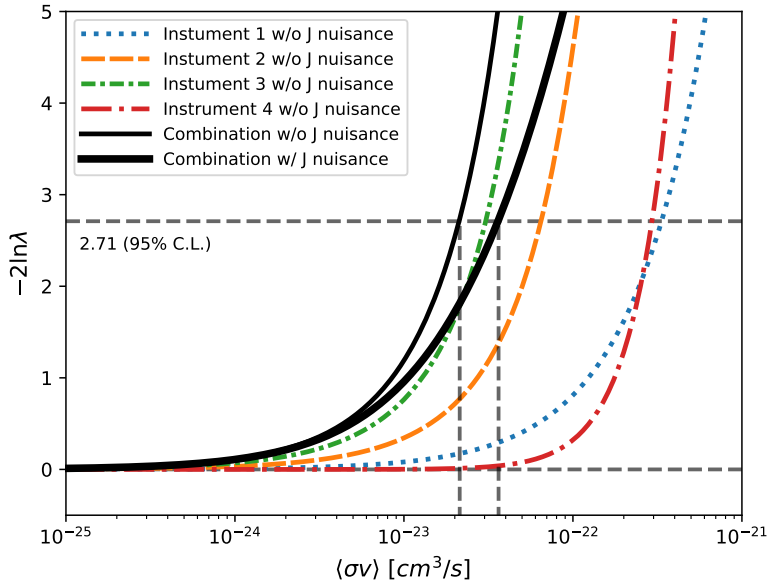


Figure 7.4 Illustration of the combination technique showing a comparison between  $-2 \ln \lambda$  provided by four instruments (colored lines) from the observation of the same dSph without any  $J$  nuisance and their sum, *i.e.* the resulting combined likelihood (thin black line). According to the test statistics of Equation (7.18), the intersection of the likelihood profiles with the line  $-2 \ln \lambda = 2.71$  indicates the 95% C.L. upper limit on  $\langle \sigma v \rangle$ . The combined likelihood (thin black line) shows a smaller value of upper limit on  $\langle \sigma v \rangle$  than those derived by individual instruments. We also show the uncertainties on the  $J$ -factor affects the combined likelihood and degrade the upper limit on  $\langle \sigma v \rangle$  (thick black line). All likelihood profiles are normalized so that the global minimum  $\widehat{\langle \sigma v \rangle}$  is 0. We note that each profile depends on the observational conditions in which a target object was observed. The sensitivity of a given instrument can be degraded and the upper limits less constraining if the observations are performed in non optimal conditions such as a high zenith angle or a short exposure time.

790 this work, versus  $\langle \sigma v \rangle$ .  $\mathcal{L}_{dSph,l}$  is computed for a fixed value of  $J_l$  and profiled with respect to all  
 791 instrumental nuisance parameters  $\nu_l$ , these nuisance parameters are discussed in more detail below.  
 792 These values are produced by each detector independently and therefore there is no need to share  
 793 sensitive low-level information used to produce them, such as event lists. Figure 7.4 illustrates the  
 794 multi-instrument combination technique used in this study with a comparison of the upper limit  
 795 on  $\langle \sigma v \rangle$  obtained from the combination of the observations of four experiments towards one dSph  
 796 versus the upper limit from individual instruments. It also shows graphically the effect of the  
 797  $J$ -factor uncertainty on the combined observations.

798 The *partial* joint likelihood function for gamma-ray observations of each dSph ( $\mathcal{L}_{dSph,l}$ ) is

written as the product of the likelihood terms describing the  $N_{\text{exp},l}$  observations performed with any of our observatories:

$$\mathcal{L}_{\text{dSph},l} (\langle \sigma v \rangle; J_l, \nu_l | \mathcal{D}_l) = \prod_{k=1}^{N_{\text{exp},l}} \mathcal{L}_{lk} (\langle \sigma v \rangle; J_l, \nu_{lk} | \mathcal{D}_{lk}), \quad (7.15)$$

where each  $\mathcal{L}_{lk}$  term refers to an observation of the  $l$ -th dSph with associated  $k$ -th instrument responses.  $N_{\text{exp},l}$  varies from dSph to dSph and can be inferred from Table 7.2.

Each collaboration separately analyzes their data for  $\mathcal{D}_{lk}$  corresponding to dSph  $l$  and gamma-ray detector  $k$ , using as many common assumptions as possible in the analysis. HAWC's treatment was described earlier in Section 7.4.1 whereas the specifics of the remaining experiments is left to the publication. We compute the values for the likelihood functions  $\mathcal{L}_{lk}$  (see Eq. (7.15)) for a fixed value of  $J_l$  and profile over the rest of the nuisance parameters  $\nu_{lk}$ . Then, values of  $\lambda$  from ?? are computed as a function of  $\langle \sigma v \rangle$ , and shared using a common format. Results are computed for seven annihilation channels,  $W^+W^-$ ,  $ZZ$ ,  $b\bar{b}$ ,  $t\bar{t}$ ,  $e^+e^-$ ,  $\mu^+\mu^-$ , and  $\tau^+\tau^-$  over 62  $m_\chi$  values between 5 GeV and 100 TeV provided in [43]. The  $\langle \sigma v \rangle$  range is defined between  $10^{-28}$  and  $10^{-18} \text{cm}^3 \cdot \text{s}^{-1}$ , with 1001 logarithmically spaced values.

The  $i$ th bin is iterated over spatial and  $f_{\text{hit}}$ . Then we combine the profiles across all five experiments. The profile likelihood ratio  $\lambda$  as a function of annihilation cross-section  $\langle \sigma v \rangle$  is computed with: for a considered annihilation channel and DM mass.

**TODO: Section pasted from paper. Rephrase cause plagiarism is a thing.** As mentioned previously, each experiment computes the  $\mathcal{L}_{lk}$  from Equation (7.10) differently. The remainder of this section highlights the differences in this calculation across the experiments. Four experiments, namely *Fermi*-LAT, H.E.S.S., HAWC and MAGIC, use a binned likelihood to compute the  $\mathcal{L}_{lk}$ . For these experiments, for each observation  $\mathcal{D}_{lk}$  of a given dSph  $l$  carried out using a given gamma-ray detector  $k$ , the binned likelihood function is:

$$\mathcal{L}_{lk} (\langle \sigma v \rangle; J_l, \nu_{lk} | \mathcal{D}_{lk}) = \prod_{i=1}^{N_E} \prod_{j=1}^{N_P} \left[ \mathcal{P}(s_{lk,ij}(\langle \sigma v \rangle, J_l, \nu_{lk}) + b_{lk,ij}(\nu_{lk}) | N_{lk,ij}) \right] \times \mathcal{L}_{lk,\nu} (\nu_{lk} | \mathcal{D}_{\nu_{lk}}) \quad (7.16)$$

where  $N_E$  and  $N_P$  are the number of considered bins in reconstructed energy and arrival direction, respectively;  $\mathcal{P}$  represents a Poisson PDF for the number of gamma-ray candidate events observed in the  $i$ -th bin in energy and  $j$ -th bin in arrival direction, when the expected number is the sum of the expected mean number of signal events  $s_{ij}$  (produced by DM annihilation) and of background events  $b_{ij}$ ;  $\mathcal{L}_{lk,\nu}$  is the likelihood term for the extra  $\nu_{lk}$  nuisance parameters that vary from one instrument  $k$  to another. The expected counts for signal events  $s_{ij}$  for a given dSph  $l$  and detector  $k$  is given by:

$$s_{ij}(\langle\sigma\nu\rangle, J) = \int_{E'_{\min,i}}^{E'_{\max,i}} dE' \int_{P'_{\min,j}}^{P'_{\max,j}} d\Omega' \int_0^\infty dE \int_{\Delta\Omega_{tot}} d\Omega \int_0^{T_{\text{obs}}} dt \frac{d^2\Phi(\langle\sigma\nu\rangle, J)}{dEd\Omega} \text{IRF}(E', P' | E, P, t) \quad (7.17)$$

where  $E'$  and  $E$  are the reconstructed and true energies,  $P'$  and  $P$  the reconstructed and true arrival directions;  $E'_{\min,i}$ ,  $P'_{\min,j}$ ,  $E'_{\max,i}$ , and  $P'_{\max,j}$  are their lower and upper limits of the  $i$ -th energy bin and the  $j$ -th arrival direction bin;  $T_{\text{obs}}$  is the (dead-time corrected) total observation time;  $t$  is the time along the observations;  $d^2\Phi/dEd\Omega$  is the DM flux in the source region (see Equation (7.1)); and  $\text{IRF}(E', P' | E, P, t)$  is the IRF, which can be factorized as the product of the effective collection area of the detector  $A_{\text{eff}}(E, P, t)$ , the PDFs for the energy estimator  $f_E(E' | E, t)$ , and arrival direction  $f_P(P' | E, P, t)$  estimators. Note that for Fermi-LAT, HAWC, MAGIC, and VERITAS the effect of the finite angular resolution is taken into account through the convolution of  $d\Phi/dEd\Omega$  with  $f_P$  in Equation (7.17), whereas in the cases of H.E.S.S.  $f_P$  is approximated by a delta function. This approximation has been made in order to maintain compatibility of the result with what has been previously published. The difference introduced by this approximation is  $< 5\%$  for all considered dSphs. **TODO: End of paper section**

From Equation (7.10), we can compute the test statistic (TS) with the ratio test:

$$\text{TS} = -2 \ln \left( \frac{\mathcal{L}_0}{\mathcal{L}^{\text{max}}} \right) \quad (7.18)$$

$\mathcal{L}^{\text{max}}$  here is equivalent to  $\mathcal{L}(N_i, B_i, S_i = 0)$  or no signal counts.

842 **7.5 HAWC Results**

843 13 of the 20 dSphs considered for the Glory Duck analysis are within HAWC's field of view.  
844 These dSph are analyzed for emission from DM annihilation according to the likelihood method  
845 described in Section 7.4. The 13 likelihood profiles are then combined to create a combined limit  
846 on the dark matter cross-section. This combination is done for the 7 annihilation channels used in  
847 the Glory Duck analysis. Figure 7.5 shows the combined limit for all annihilation channels with  
848 HAWC only observations. We also perform 300 studies of Poisson trials on the background. These  
849 trials are used to produce HAWC Brazil bands which were shared with the other collaborators for  
850 combined Brazil Bands. The results on fitting to HAWC's poisson trials of the DM hypothesis is  
851 shown in Figure 7.6 for seven of the DM annihilation channels.

852 No DM was found in HAWC observations. The limits are dominated by the dSph Segue1 and  
853 Coma Berenices. The remaining 11 dSphs do not contribute significantly to the limit. Even though  
854 some of the remaining dSphs have large J-factors, they are towards the edge of HAWC's field of  
855 view where this analysis is less sensitive.

856 **7.6 Glory Duck Combined Results**

857 The crux of this analysis is that HAWC's results are combined with 4 other gamma-ray obser-  
858 vatories: Fermi-LAT, H.E.S.S., MAGIC, and VERITAS. The complete joint likelihood for the  $l$ -th  
859 dSph is the product of likelihood functions of the 5 experiments.

860 **TODO: place holder for results**

861 No significant DM emission was observed by any of the five telescopes. We present upper  
862 limits on  $\langle\sigma v\rangle$  using the test statistics, Eq. (7.18).

$$TS = -2 \ln \lambda(\langle\sigma v\rangle), \quad (7.19)$$

863 No significant DM emission was observed by any of the five instruments. We present the upper  
864 limits on  $\langle\sigma v\rangle$  assuming seven independent DM self annihilation channels, namely  $W^+W^-$ ,  $Z^+Z^-$ ,  
865  $b\bar{b}$ ,  $t\bar{t}$ ,  $e^+e^-$ ,  $\mu^+\mu^-$ , and  $\tau^+\tau^-$ . The 68% and 95% containment bands are produced from 300  
866 Poisson realizations of the null hypothesis corresponding to each of the combined datasets. These

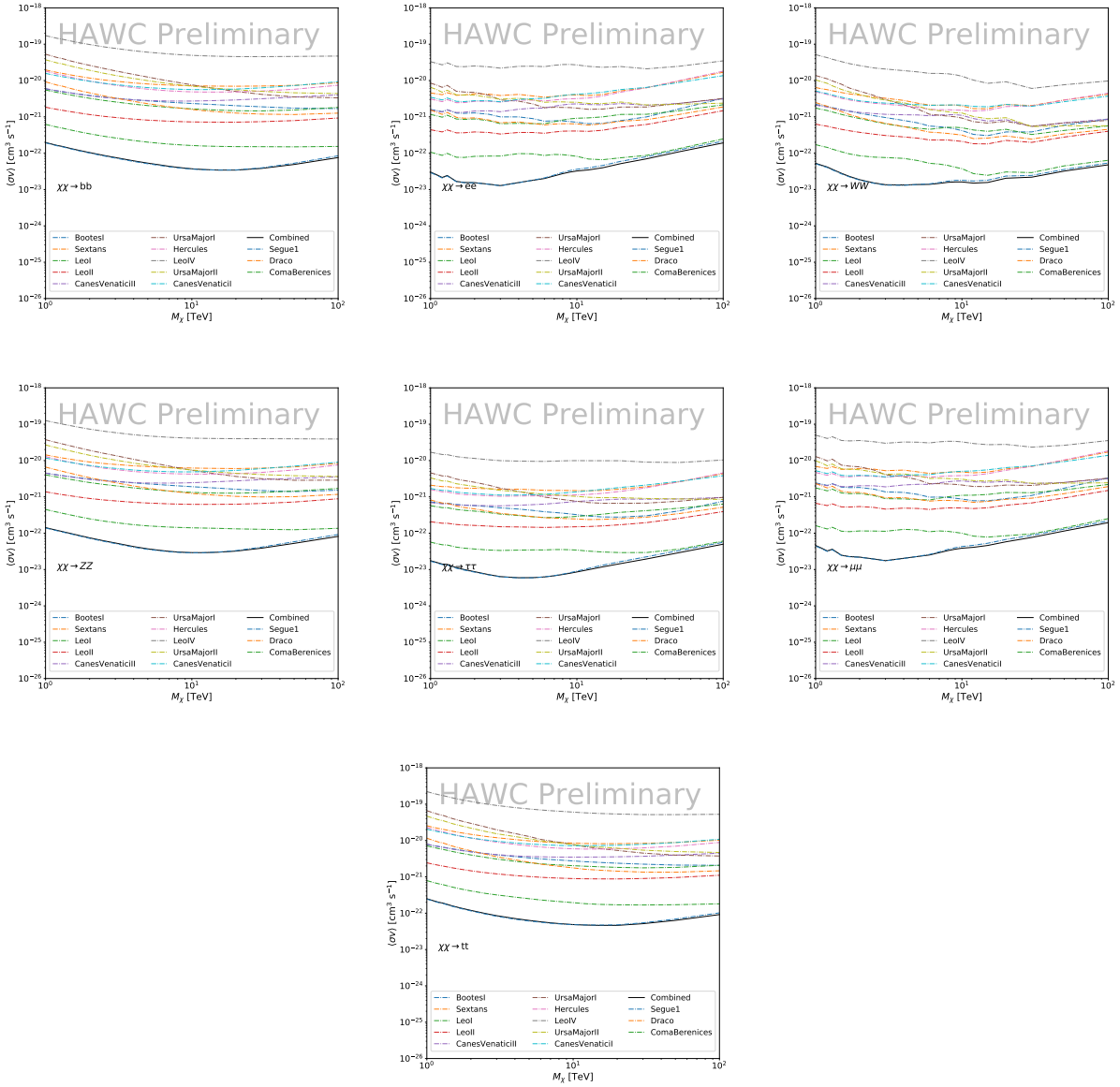


Figure 7.5 HAWC upper limits at 95% confidence level on  $\langle\sigma v\rangle$  versus DM mass for seven annihilation channels, using the set of  $J$ -factors from Ref. [49]. The solid line represents the observed combined limit. Dashed lines represent limits from individual dSphs.

867 300 realizations are combined identically to dSph observations. The containment bands and the  
 868 median are extracted from the distribution of resulting limits on the null hypothesis. These 300  
 869 realizations are obtained either by fast simulations of the OFF observations, for H.E.S.S., MAGIC,  
 870 VERITAS, and HAWC, or taken from real observations of empty fields of view in the case of  
 871 Fermi-LAT [47, 50, 51].

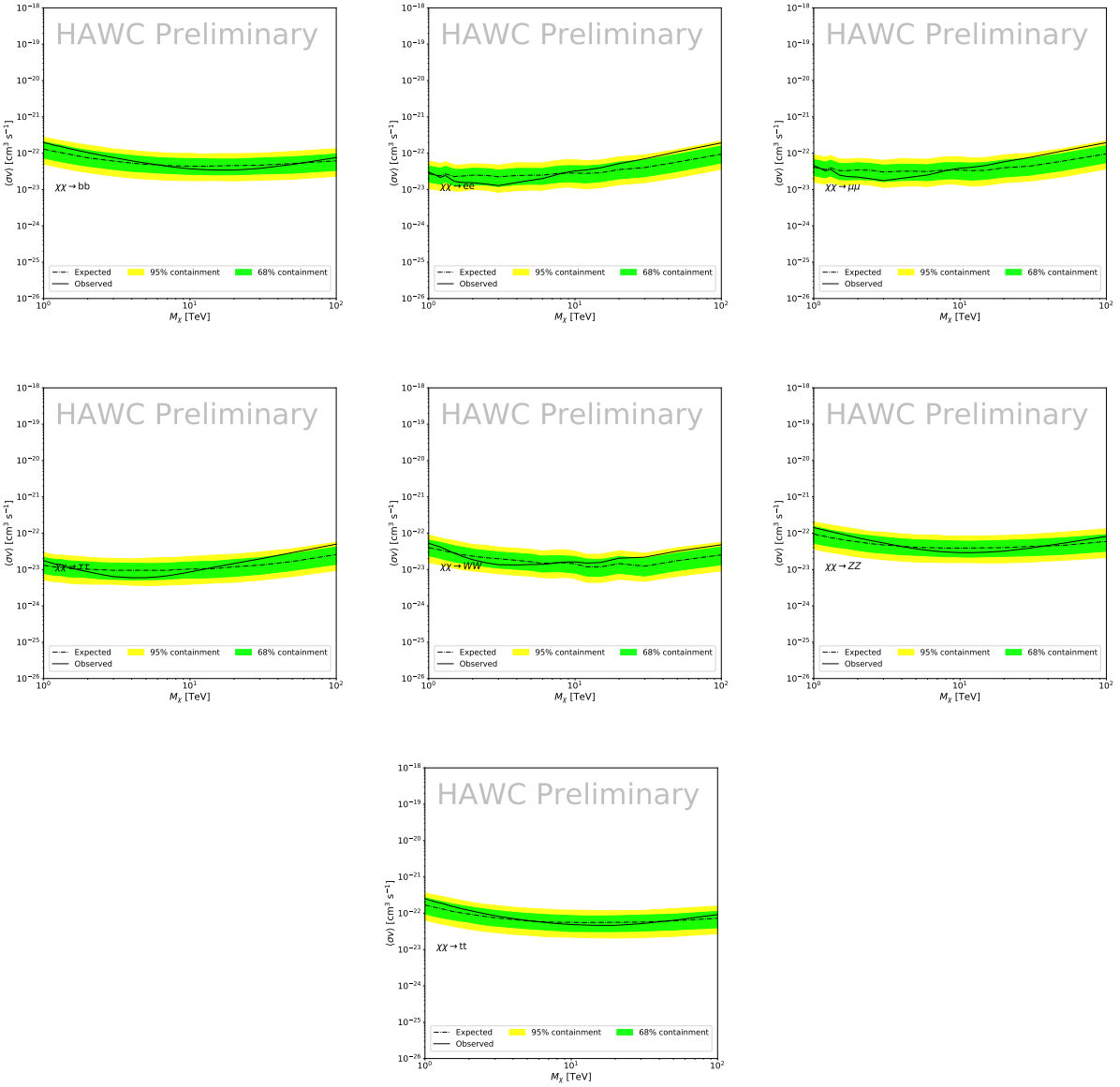


Figure 7.6 HAWC Brazil bands at 95% confidence level on  $\langle\sigma v\rangle$  versus DM mass for seven annihilation channels with  $J$ -factors from  $\mathcal{GS}$  [49]. The solid line represents the combined limit from 13 dSphs. The dashed line is the expected limit. The green band is the 68% containment. The yellow band is the 95% containment.

872     The obtained limits are shown in Figure 7.7 for the  $\mathcal{GS}$  set of  $J$ -factors [49] and in Figure 7.8  
 873    for the  $\mathcal{B}$  set of  $J$ -factors [46, 52]. The combined limits are presented with their 68% and 95%  
 874    containment bands, and are expected to be close to the median limit when no signal is present.  
 875    We observe agreement with the null hypothesis for all channels, within  $2\sigma$  standard deviations,  
 876    between the observed limits and the expectations given by the median limits. Limits obtained from

877 each detector are also indicated in the figures, where limits for all dSphs observed by the specific  
878 instrument have been combined.

879 Below  $\sim$ 300 GeV, the *Fermi*-LAT dominates the DM limits for all annihilation channels. From  
880  $\sim$ 300 GeV to  $\sim$ 2 TeV, *Fermi*-LAT continues to dominate for the hadronic and bosonic DM channels,  
881 yet the IACTs (H.E.S.S., MAGIC, and VERITAS) and *Fermi*-LAT all contribute to the limit for  
882 leptonic DM channels. For DM masses between  $\sim$ 2 TeV to  $\sim$ 10 TeV, the IACTs dominate leptonic  
883 DM annihilation channels, whereas both the *Fermi*-LAT and the IACTs dominate bosonic and  
884 hadronic DM annihilation channels. From  $\sim$ 10 TeV to  $\sim$ 100 TeV, both the IACTs and HAWC  
885 contribute significantly to the leptonic DM limit. For hadronic and bosonic DM, the IACTs and  
886 *Fermi*-LAT both contribute strongly.

887 We notice that the limits computed using the  $\mathcal{B}$  set of  $J$ -factor are always better compared to the  
888 ones calculated with the  $\mathcal{GS}$  set. For the  $W^+W^-$ ,  $Z^+Z^-$ ,  $b\bar{b}$ , and  $t\bar{t}$  channels, the ratio between the  
889 limits computed with the two sets of  $J$ -factor is varying between a factor of  $\sim$ 3 and  $\sim$ 5 depending  
890 on the energy, with the largest ratio around 10 TeV. For the channels  $e^+e^-$ ,  $\mu^+\mu^-$ , and  $\tau^+\tau^-$ , the  
891 ratio lies between  $\sim$ 2 to  $\sim$ 6, being maximum around 1 TeV. Examining Figure 7.15 and Figure 7.16  
892 in Section 7.8, these differences are explained by the fact that the  $\mathcal{B}$  set provides higher  $J$ -factors  
893 for the majority of the studied dSphs, with the notable exception of Segue I. The variation on the  
894 ratio of the limits for the two sets is due to different dSph dominating the limits depending on the  
895 energy. This pushes the range of thermal cross-section which can be excluded to higher mass. This  
896 comparison demonstrates the magnitude of systematic uncertainties associated with the choice of  
897 the  $J$ -factor

898 This comparison demonstrates the magnitude of systematic uncertainties associated with the  
899 choice of the  $J$ -factor calculation. The  $\mathcal{GS}$  and  $\mathcal{B}$  sets present a difference in the limits for all  
900 channels of about This difference is explained, see Figure 7.15 and Figure 7.16 in Appendix, by the  
901 fact that the  $\mathcal{B}$  set provides higher  $J$  factors for all dSph except for Segue I. This pushes the range  
902 of thermal cross-section which can be excluded to higher mass.

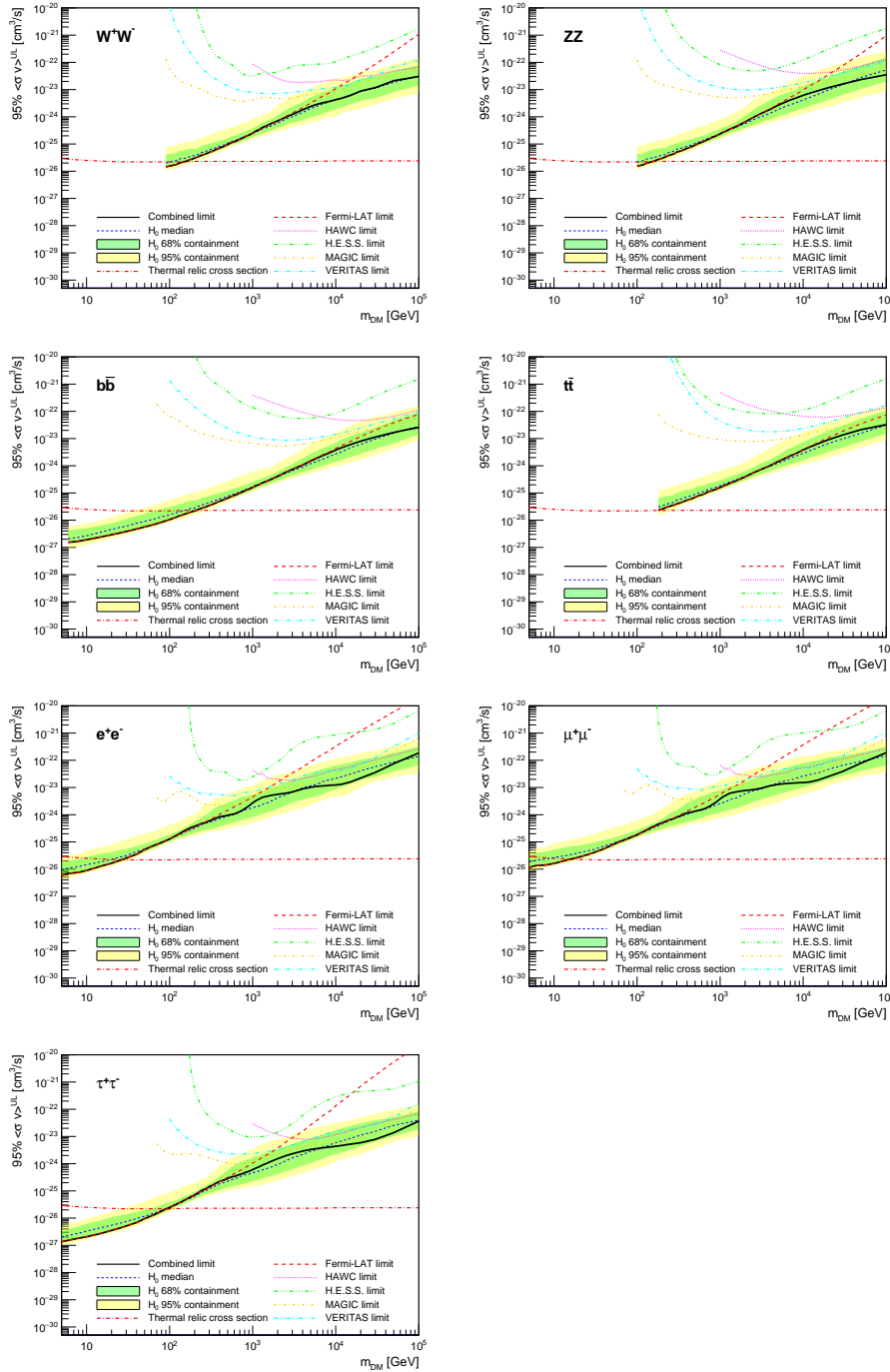


Figure 7.7 Upper limits at 95% confidence level on  $\langle\sigma v\rangle$  in function of the DM mass for eight annihilation channels, using the set of  $J$  factors from Ref. [49] ( $\mathcal{GS}$  set in Table 7.1). The black solid line represents the observed combined limit, the black dashed line is the median of the null hypothesis corresponding to the expected limit, while the green and yellow bands show the 68% and 95% containment bands. Combined upper limits for each individual detector are also indicated as solid, colored lines. The value of the thermal relic cross-section in function of the DM mass is given as the red dotted-dashed line [53].

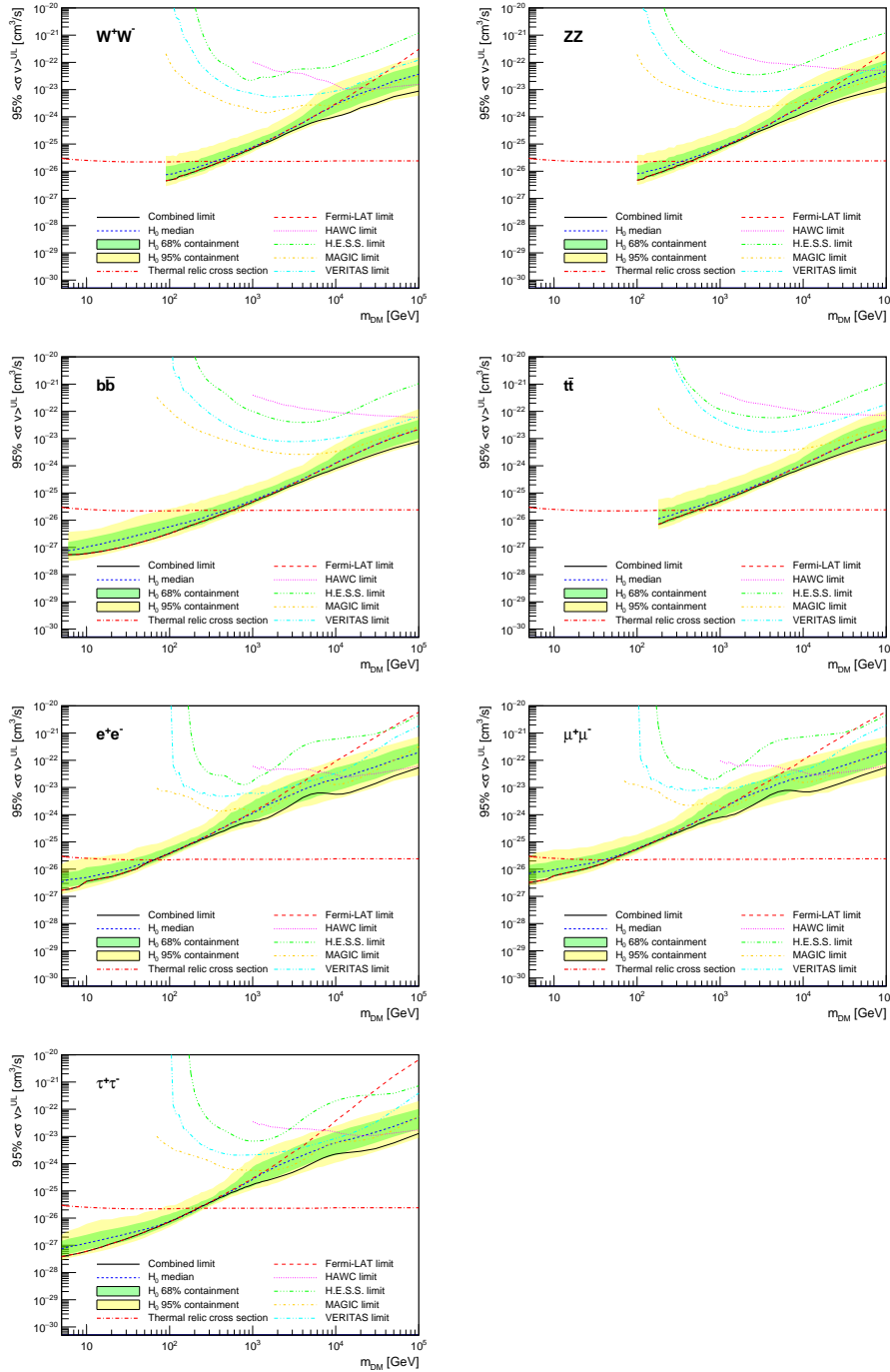


Figure 7.8 Same as Fig. 7.7, using the set of  $J$  factors from Ref. [46, 52] ( $\mathcal{B}$  set in Table 7.1).

## 903 7.7 HAWC Systematics

### 904 7.7.1 Inverse Compton Scattering

905 The DM-DM annihilation channels produce many high energy electrons regardless of the  
 906 primary annihilation channel. These high energy electrons can produce high energy gamma-rays

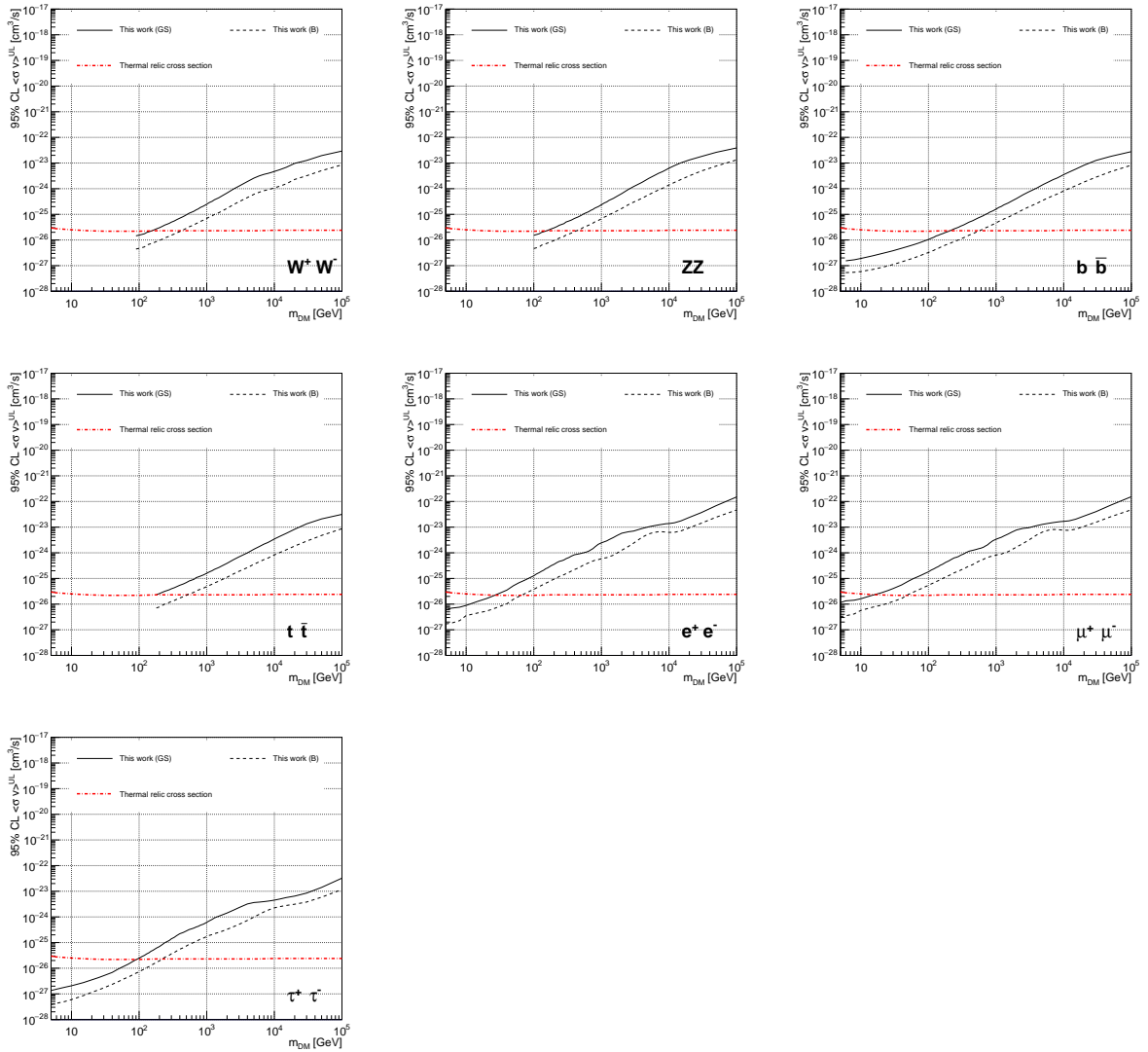


Figure 7.9 Comparisons of the combined limits at 95% confidence level for each of the eight annihilation channels when using the  $J$  factors from Ref. [49] ( $\mathcal{GS}$  set in Table 7.1), plain lines, and the  $J$  factor from Ref. [46, 52] ( $\mathcal{B}$  set in Table 7.1), dashed lines. The cross-section given by the thermal relic is also indicated [53].

through Inverse Compton Scattering (ICS). If this effect is strong, it would change the morphology of the source and increase the total expected gamma-ray counts from any source. The PPPC [43] provides tools in Mathematica for calculating the impact of ICS for an arbitrary location in the sky for a specified annihilation channel. We calculated the change in gamma-ray counts for DM annihilation to primary  $e\bar{e}$  for RA and Dec corresponding to Segue1 and Coma Berenices. These dSphs were chosen because they are the strongest contributors to the limit.  $e\bar{e}$  was selected because

it would have the largest number of high energy electrons. The effect was found to be on the order of  $10^{-7}$  on the gamma-ray spectrum. As a result, this systematic is not considered in our analysis.

## 7.7.2 Point Source Versus Extended Source Limits

The previous DM search toward dSph approximated the dSphs as point sources [45]. In this analysis, the dSphs are implemented as extended with J-factor distributions following those produced by [49]. The resolution of the cited map is much finer than HAWC's angular resolution. The vast majority of the J-factor distribution is represented on the central HAWC pixel of the dSph spatial map. However, the neighboring 8 pixels are not negligible and contribute to our limit.

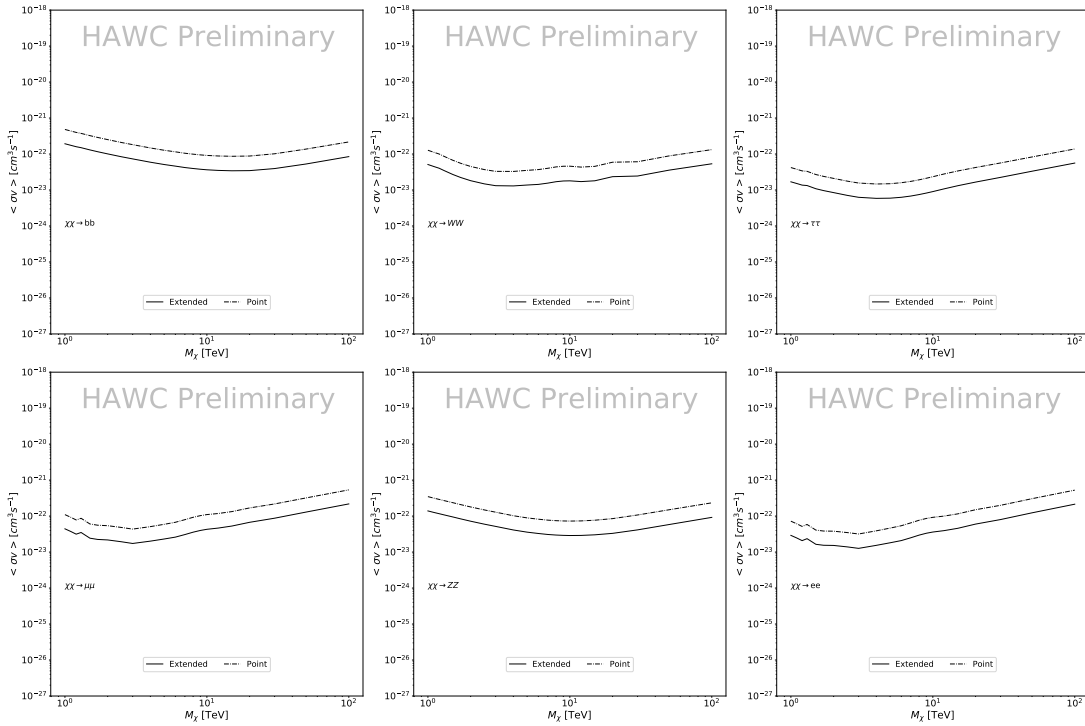


Figure 7.10 Comparisons of the combined limits at 95% confidence level for a point source analysis and extended source using [49] *GS* J-factor distributions and PPPC [43] annihilation spectra. Shown are the limits for Segue1 which will have the most significant impact on the combined limit. 6 of the 7 DM annihilation channels are shown. Solid lines are extended source studies. Dashed lines are point source studies. Overall, the extended source analysis improves the limit by a factor of 2.

Figure 7.10 shows a substantial improvement to the limit for Segue1. Fig. 7.11 however showed identical limits. These disparities are best explained by the relative difference in their J-Factors. Both dSphs pass almost overhead the HAWC detector, however Segue1 has the larger J-Factor

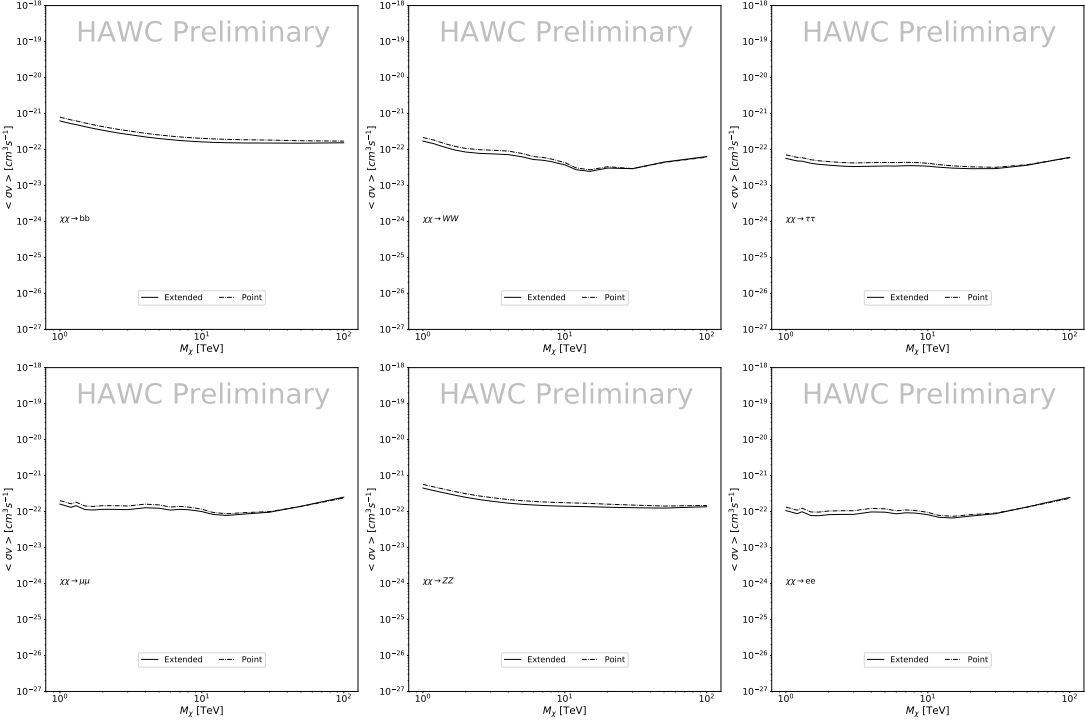


Figure 7.11 Same as Fig. 7.10 on Coma Berenices. This dSph also contributes significantly to the limit. The limits are identical in this case.

924 between the two. Adjacent pixels to the central pixel will therefore contribute to the limits. This is  
 925 the case for other dSph that are closer to overhead the HAWC detector.

926 Comparison plots for all sources and the combined limit can be found in the sandbox for the  
 927 Glory Duck project.

### 928 7.7.3 Impact of Pointing Systematic

929 During the analysis it was discovered that reconstruction of gamma-rays. Slides describing this  
 930 systematic can be found [here](#). Shown on the presentation is dependence on the pointing systematic  
 931 on declination. New spatial profiles were generated for every dSph and limits were computed for  
 932 the adjusted declination.

933 Section 7.7.3 demonstrates the impact of this systematic for all DM annihilation channels  
 934 studied by HAWC. The impact is a tiny improvement, yet mostly identical, to the combined limits.

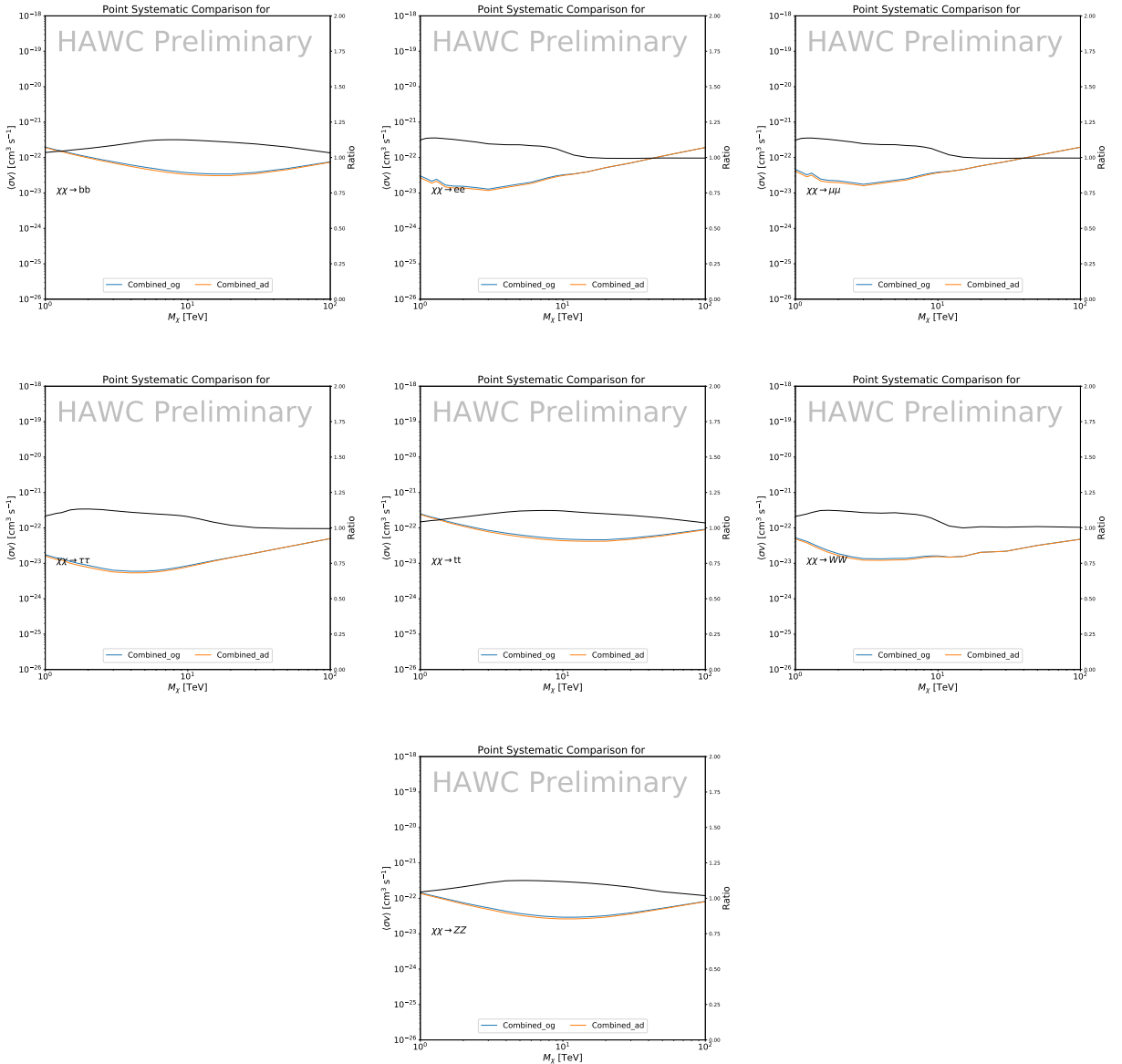


Figure 7.12 Comparison of combined limits when correcting for HAWC's pointing systematic. All DM annihilation channels are shown. The solid black line is the ratio between published limit to the declination corrected limit. The blue solid line or "Combined\_og" represented the limits computed for Glory Duck. The solid orange line or "Combined\_ad" represented the limits computed after correcting for the pointing systematic.

## 935 7.8 J-factor distributions

### 936 7.8.1 Numerical integration of $\mathcal{GS}$ maps

937 It was discovered well after the HAWC analysis was completed that the published tables from

938  $\mathcal{GS}$  [44] quoted median  $J$ -factors were computed in a non-trivial manner. The assumption myself

and collaborators had was that the published tables represented the  $J$ -factor as a function of  $\theta$  for the best global fit model on a per source basis. However, this is not the case. Instead, what is published are the best fit model for each dwarf that only considers stars up to the angular separation  $\theta$ . Therefore, the model is changing for each value of  $\theta$  for each dwarf. Yet, the introduced features from unique models at each  $\theta$  are much smaller than the angular resolution of HAWC. It is not expected for these effects to impact the limits and TS greatly as a result.

Median  $J$ -factor model profiles were provided by the authors. New maps were generated and analyzed for Segue1 and Coma Berenices. Figure 7.13 shows the differential between maps generated with the method from Section 7.8.1 and from the authors of [44]. These maps were reanalyzed for all SM DM annihilation channels. Upper limits for these channels are shown in Figure 7.14

From Figure 7.14, we can see that the impact of these model difference was no substantial. The observed impact was a fractional effect which is much smaller than the impact from selecting another DM spatial distribution model as was shown in Figure 7.9.

### 7.8.2 $\mathcal{GS}$ versus $\mathcal{B}$ spatial models

We show in this appendix a comparison between the  $J$ -factors computed by Geringer-Sameth *et al.* [49] (the  $\mathcal{GS}$  set) and the ones computed by Bonnivard *et al.* [46, 52] (the  $\mathcal{B}$  set). The  $\mathcal{GS}$   $J$ -factors are computed through a Jeans analysis of the kinematic stellar data of the selected dSphs, assuming a dynamic equilibrium and a spherical symmetry for the dSphs. They adopted the generalized DM density distribution, known as Zhao-Hernquist, introduced by [54], carrying three additional index parameters to describe the inner and outer slopes, and the break of the density profile. Such a profile parametrization allows the reduction of the theoretical bias from the choice of a specific radial dependency on the kinematic data. In other words, the increase of free parameters with the use of the Zhao-Hernquist profile allows a better description of the mass density distribution of dark matter.

In addition, a constant velocity anisotropy profile and a Plummer light profile [55] for the stellar distribution were assumed. The velocity anisotropy profile depends on the radial and tangential

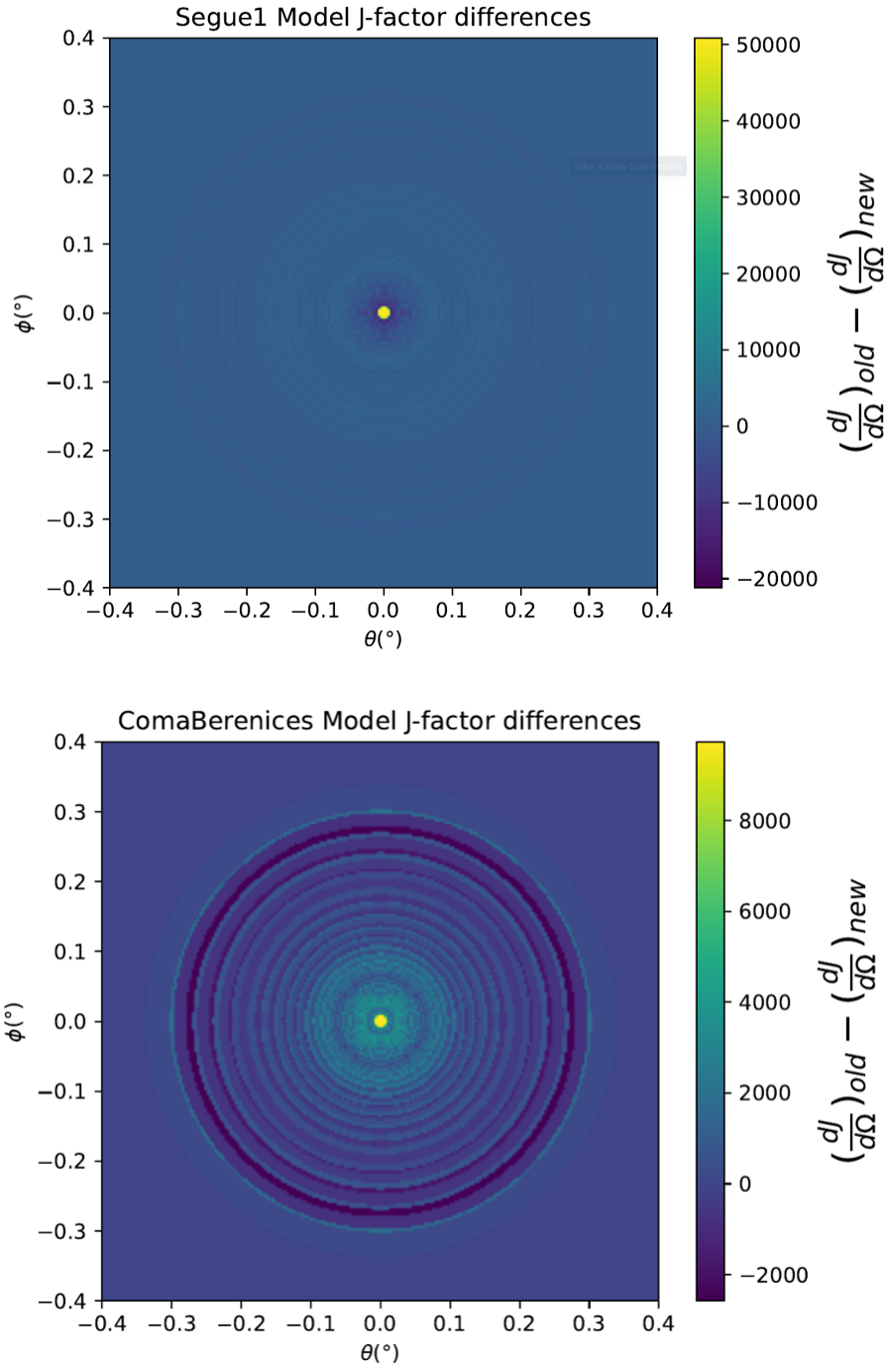


Figure 7.13 Differential map of  $dJ/\Omega$  from model built in Section 7.8.1 and profiles provided directly from authors. (Top) Differential from Segue1. (bottom) Differential from Coma Berenices. Note that their scales are not the same. Segue1 shows the deepest discrepancies which is congruent with its large uncertainties. Both models show anuli where unique models become apparent.

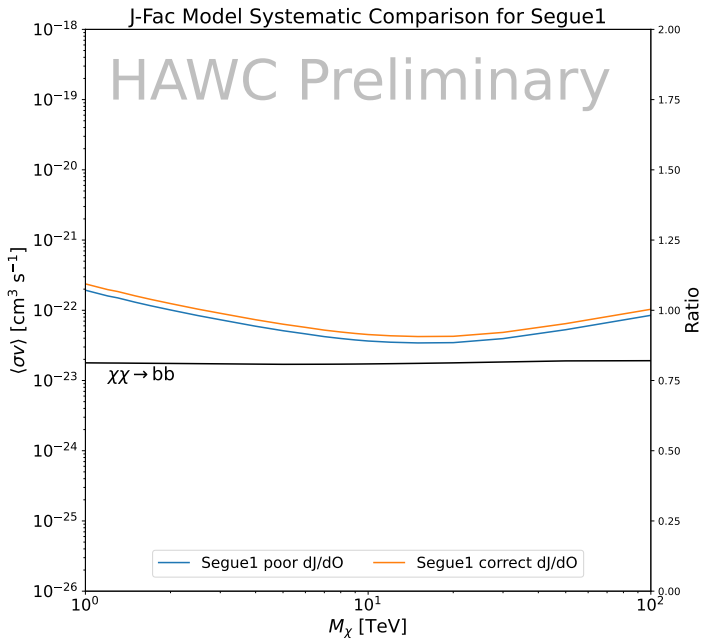
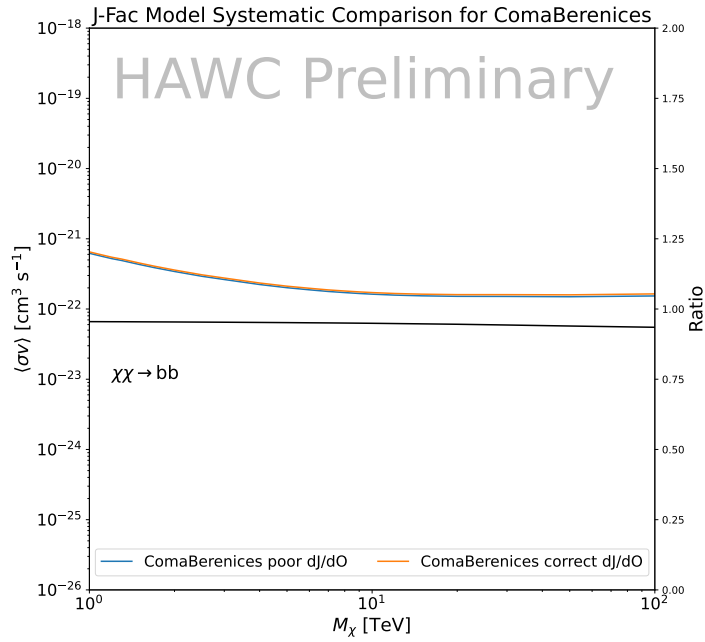


Figure 7.14 HAWC limits for Coma Berenices (top) and Segue1 (bottom) for two different map sets. Blue lines are limits calculated on maps with poor model representation. Orange lines are limits calculated on spatial profiles provided by the authors of [44]. Black line is the ratio of the poor spatial model limits to the corrected spatial models. The left y-axis measures  $\langle \sigma v \rangle$  for the blue and orange lines. The right y-axis measures the ratio and is unitless.

velocity dispersions. However, its determination remains challenging since only the line-of-sight velocity dispersion can be derived from velocity measurements. Therefore, the parametrization of the anisotropy profile is obtained from simulated halos (see [56] for more details). They provide the values of the  $J$ -factors of regions extending to various angular radius up to the outermost member star.

The  $\mathcal{B}$   $J$ -factors were computed through a Jeans analysis taking into account the systematic uncertainties induced by the DM profile parametrization, the radial velocity anisotropy profile, and the triaxiality of the halo of the dwarf galaxies. They performed a more complete study of the dSph kinematics and dynamics than  $\mathcal{GS}$  for the determination of the  $J$ -factor. Conservative values of the  $J$ -factors where obtained using an Einasto DM density profile [57], a realistic anisotropy profile known as the Baes & Van Hese profile [58] which takes into account that the inner regions can be significantly non-isotropic, and a Zhao-Hernquist light profile [54].

For both sets,  $J$ -factor values are provided for all dSphs as a function of the radius of the integration region [49, 46, 52]. Table 7.1 shows the heliocentric distance and Galactic coordinates of the twenty dSphs, together with the two sets of  $J$ -factor values integrated up to the outermost observed star for  $\mathcal{GS}$  and the tidal radius for  $\mathcal{B}$ . Both  $J$ -factor sets were derived through a Jeans analysis based on the same kinematic data, except for Draco where the measurements of [59] have been adopted in the computation of the  $\mathcal{B}$  value. The computations for producing the  $\mathcal{GS}$  and  $\mathcal{B}$  samples differ in the choice of the DM density, velocity anisotropy, and light profiles, for which the set  $\mathcal{B}$  takes into account some sources of systematic uncertainties.

Figure 7.15 and Figure 7.16 show the comparisons for the  $J$ -factor versus the angular radius for each of the 20 dSphs used in this study. The uncertainties provided by the authors are also indicated in the figures. For the  $\mathcal{GS}$  set, the computation stops at the angular radius corresponding to the outermost observed star, while for the  $\mathcal{B}$  set, the computation stops at the angular radius corresponding to the tidal radius.

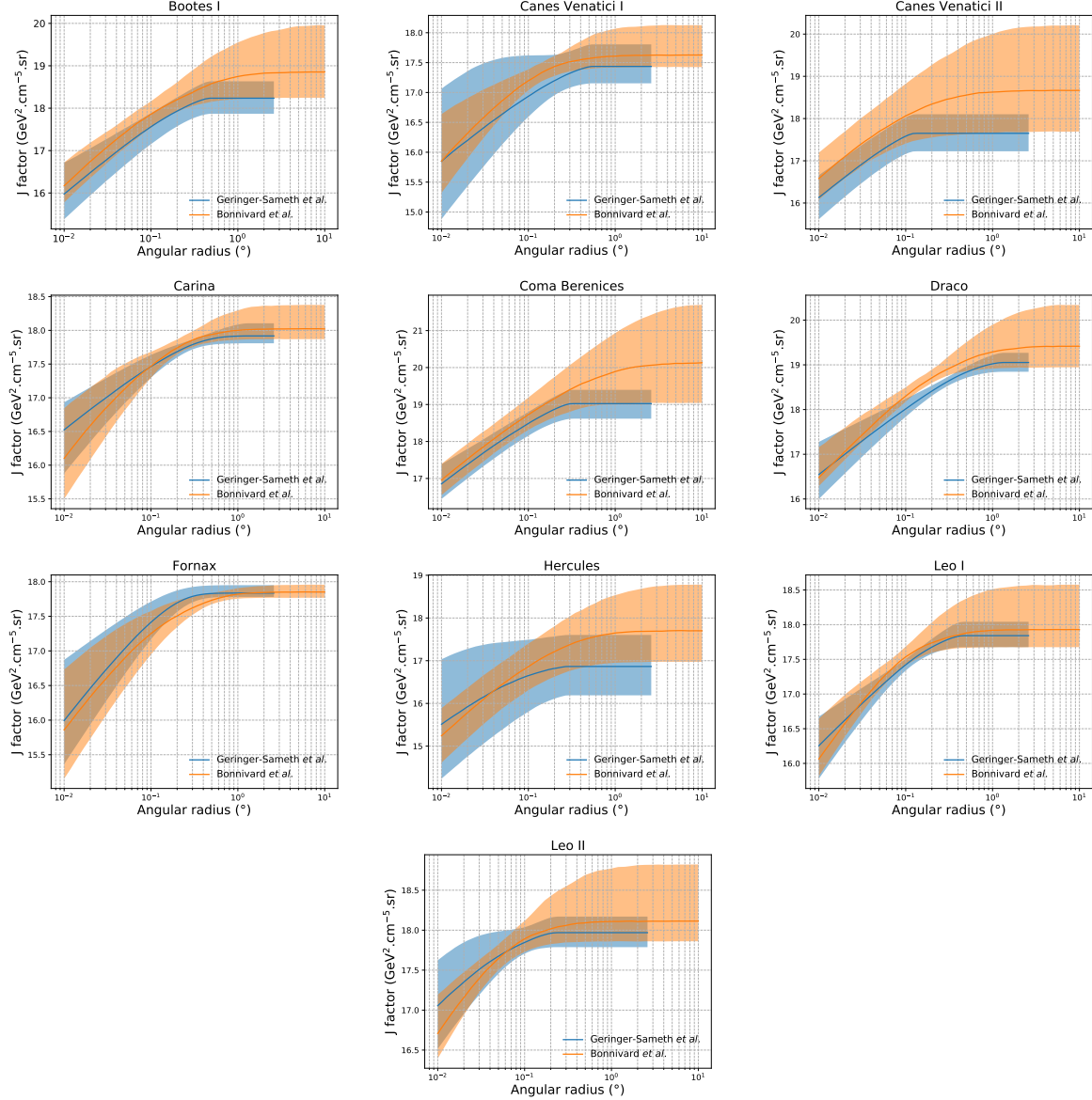


Figure 7.15 Comparisons between the  $J$ -factors versus the angular radius for the computation of  $J$  factors from Ref. [49] ( $\mathcal{GS}$  set in Table 7.1) in blue and for the computation from Ref. [46, 52] ( $\mathcal{B}$  set in Tab. 7.1) in orange. The solid lines represent the central value of the  $J$ -factors while the shaded regions correspond to the  $1\sigma$  standard deviation.

## 991 7.9 Discussion and Conclusions

992 In this multi-instrument analysis, we have used observations of 20 dSphs from the gamma-ray  
 993 telescopes Fermi-LAT, H.E.S.S., MAGIC, VERITAS, and HAWC to perform a collective DM  
 994 search annihilation signals. The data were combined across sources and detectors to significantly  
 995 increase the sensitivity of the search. We have observed no significant deviation from the null, no

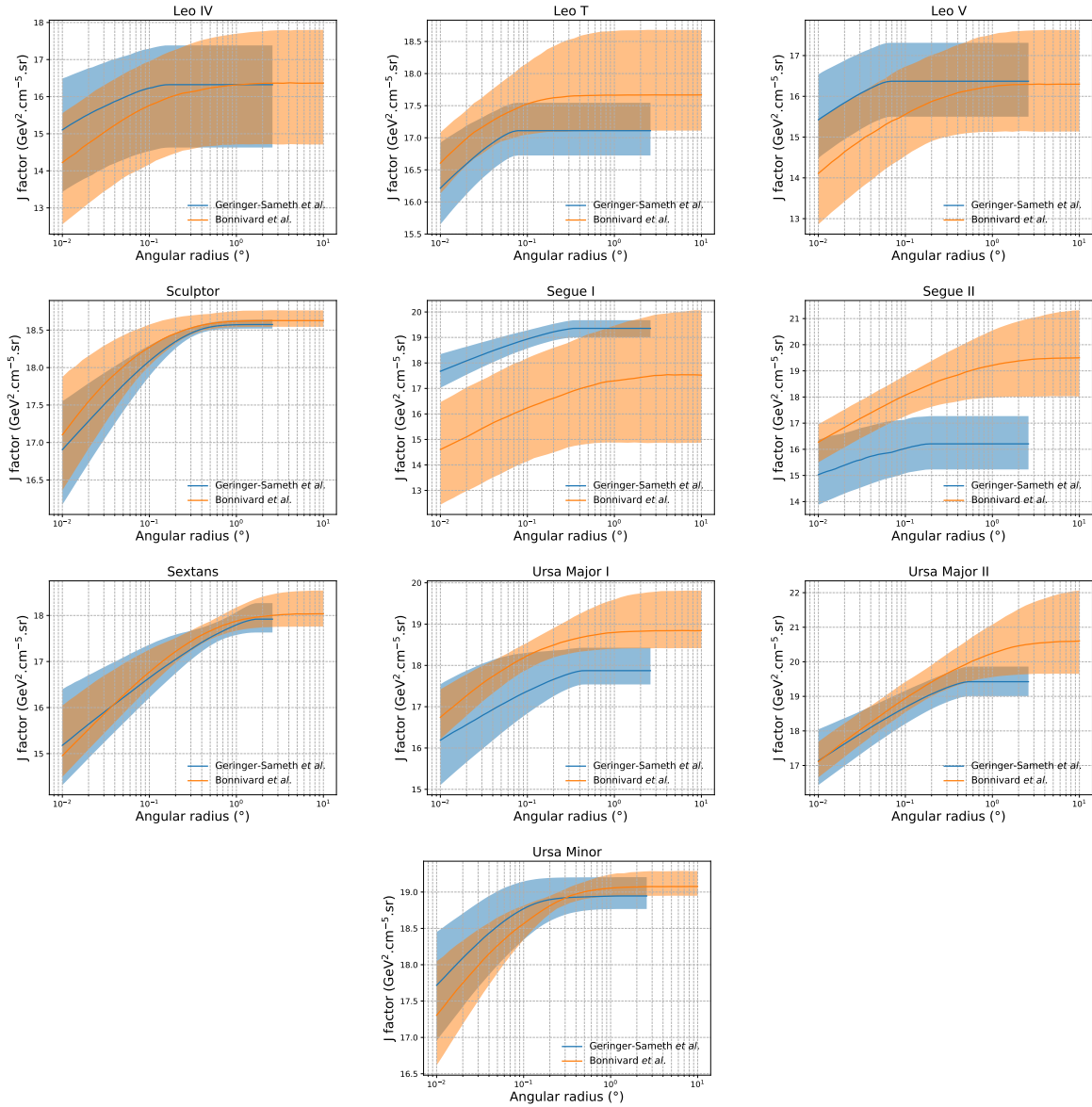


Figure 7.16 Comparisons between the  $J$ -factors versus the angular radius for the computation of  $J$  factors from Ref. [49] ( $\mathcal{GS}$  set in Tab. 7.1) in blue and for the computation from Ref. [46, 52] ( $\mathcal{B}$  set in Tab. 7.1) in orange. The solid lines represent the central value of the  $J$ -factors while the shaded regions correspond to the  $1\sigma$  standard deviation.

996 DM, hypothesis, and so present our results in terms of upper limits on the annihilation cross section  
997 for seven potential DM annihilation channels.  
998 Fermi-LAT brings the most stringent constraints for continuum channels below approximately  
999 1 TeV. the remaining detectors dominate at higher energies. Overall, for multi-TeV DM mass,  
1000 the combined DM constraints from all five telescopes are 2-3 times stronger than any individual

1001 telescope for multi-TeV DM.

1002     Derived from observations of many dSphs, our results produce robust limits given the DM  
1003 content of the dSphs is relatively well constrained. The obtained limits span the largest mass  
1004 range of any WIMP DM search. Our combined analysis improves the sensitivity over previously  
1005 published results from each detectors which produces the most stringent limits on DM annihilation  
1006 from dSphs. These results are based on deep exposures of the most promising known dSphs with  
1007 the currently most sensitive gamma-ray instruments. Therefore, our results constitute a legacy of  
1008 a generation of gamma-ray instruments on WIMP DM searches towards dSphs. Our results will  
1009 remain the reference in the field until a new generation of more sensitive gamma-ray instruments  
1010 begin operations, or until new dSphs with higher  $J$ -factors are discovered.

1011     This analysis serves as a proof of concept for future multi-instrument and multi-messenger  
1012 combination analyses. With this collaborative effort, we have managed to sample over four orders  
1013 in magnitude in gamma-ray energies with distinct observational techniques. Determining the nature  
1014 of DM continues to be an elusive and difficult problem. Larger datasets with diverse measurement  
1015 techniques could be essential to tackling the DM problem. A future collaboration using similar  
1016 techniques as the ones described in this paper could grow even beyond gamma rays. The models we  
1017 used for this study include annihilation channels with neutrinos in the final state. Advanced studies  
1018 could aim to merge our results with those from neutrino observatories with large data sets. Efforts  
1019 are already underway to add data from the IceCube, ANTARES, and KM3NeT observatories to  
1020 these gamma-ray results.

1021     From this work, a selection of the best candidates for observations, according to the latest  
1022 knowledge on stellar dynamics and modelling techniques for the derivation of the  $J$ -factors on the  
1023 potential dSphs targets, is highly desirable at the time that new experiments are starting their dark  
1024 matter programmes using dSphs. Given the systematic uncertainty inherent to the derivation of  
1025 the  $J$ -factors, an informed observational strategy would be to select both objects with the highest  
1026  $J$ -factors that could lead to DM signal detection, and objects with robust  $J$ -factor predictions, i.e.  
1027 with kinematic measurements on many bright stars, which would strengthen the DM interpretation

1028 reliability of the observation outcome.

1029 This analysis combines data from multiple telescopes to produce strong constraints on astro-  
1030 physical objects. From this perspective, these methods can be applied beyond just DM searches.

1031 Almost every astrophysical study can benefit from multi-telescope, multi-wavelength gamma-ray  
1032 studies. We have enabled these telescopes to study the cosmos with greater precision and detail.

1033 Many astrophysical searches can benefit from multi-instrument gamma-ray studies, for which our  
1034 analysis lays the foundation.

1035

## **CHAPTER 8**

### **NU DUCK**

## CHAPTER 9

### MULTITHREADING HAWC ANALYSES FOR DARK MATTER SEARCHES

**APPENDIX A**

**MULTI-EXPERIMENT SUPPLEMENTARY FIGURES**

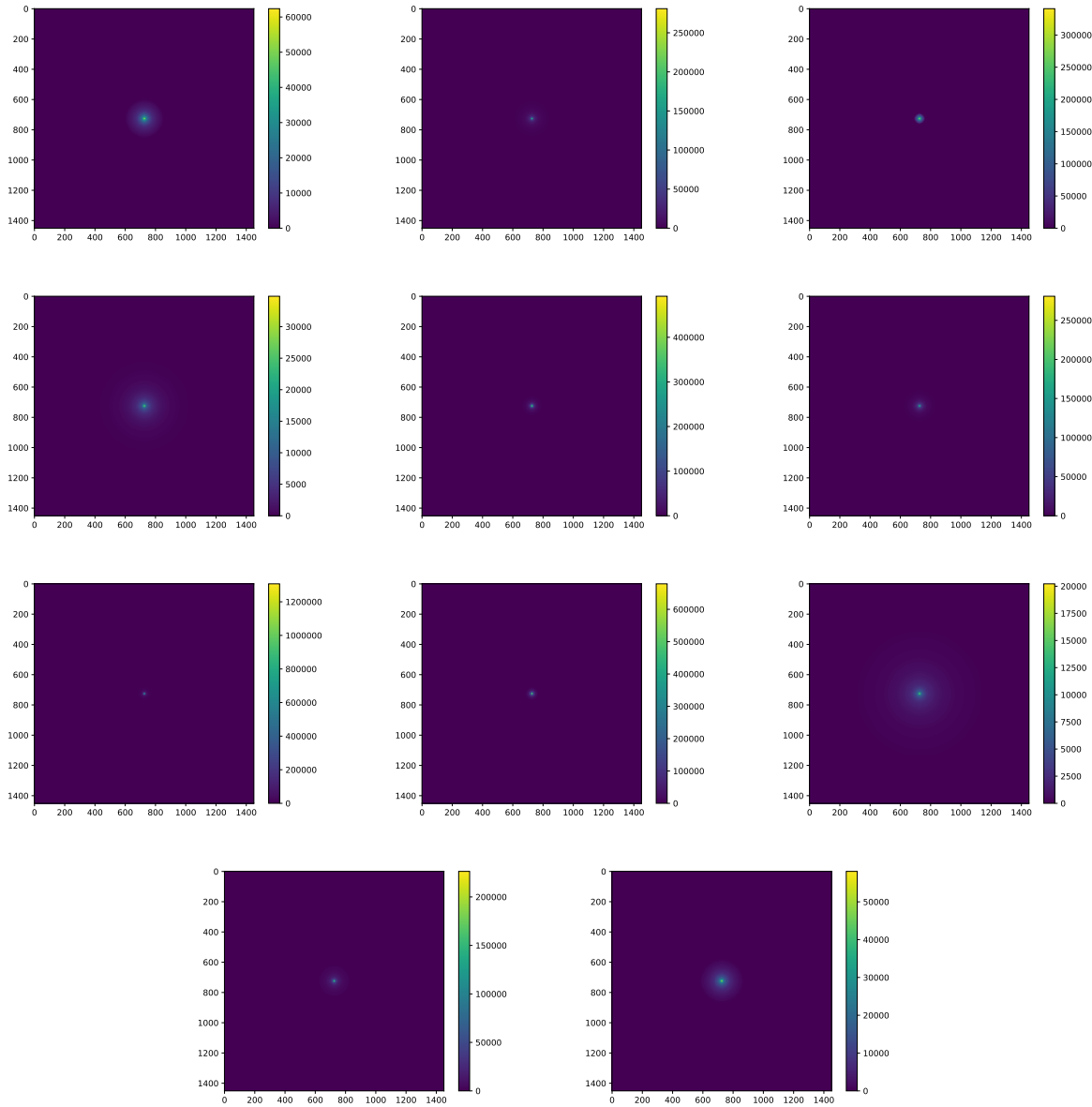


Figure A.1 Sister figure to Figure 7.3. Sources in the first row from left to right: Bootes I, Canes Venatici I, II. In second row: Draco, Hercules, Leo I. In the first row: Leo II, Leo IV, Sextans. In the final row: Ursa Major I, Ursa Major II.

## BIBLIOGRAPHY

- 1039 [1] Anne M. Green. “Dark matter in astrophysics/cosmology”. In: *SciPost Phys. Lect.*  
 1040 *Notes* (2022), p. 37. doi: [10.21468/SciPostPhysLectNotes.37](https://doi.org/10.21468/SciPostPhysLectNotes.37). URL: <https://scipost.org/10.21468/SciPostPhysLectNotes.37>.
- 1042 [2] Bing-Lin Young. “A survey of dark matter and related topics in cosmology”. In: *Frontiers*  
 1043 *of Physics* 12 (Oct. 2016). doi: <https://doi.org/10.1007/s11467-016-0583-4>.  
 1044 URL: <https://doi.org/10.1007/s11467-016-0583-4>.
- 1045 [3] Gianfranco Bertone, Dan Hooper, and Joseph Silk. “Particle dark matter: evidence,  
 1046 candidates and constraints”. In: *Physics Reports* 405.5 (2005), pp. 279–390. ISSN:  
 1047 0370-1573. doi: <https://doi.org/10.1016/j.physrep.2004.08.031>. URL:  
 1048 <https://www.sciencedirect.com/science/article/pii/S0370157304003515>.
- 1049 [4] Gianfranco Bertone and Dan Hooper. “History of dark matter”. In: *Rev. Mod. Phys.*  
 1050 90 (4 Aug. 2018), p. 045002. doi: [10.1103/RevModPhys.90.045002](https://doi.org/10.1103/RevModPhys.90.045002). URL: <https://link.aps.org/doi/10.1103/RevModPhys.90.045002>.
- 1052 [5] Fritz Zwicky. “The Redshift of Extragalactic Nebulae”. In: *Helvetica Physica Acta* 6.  
 1053 (1933), pp. 110–127. doi: [10.5169/seals-110267](https://doi.org/10.5169/seals-110267).
- 1054 [6] Vera C. Rubin and Jr. Ford W. Kent. “Rotation of the Andromeda Nebula from a  
 1055 Spectroscopic Survey of Emission Regions”. In: *ApJ* 159 (Feb. 1970), p. 379. doi:  
 1056 [10.1086/150317](https://doi.org/10.1086/150317).
- 1057 [7] K. G. Begeman, A. H. Broeils, and R. H. Sanders. “Extended rotation curves of spiral galax-  
 1058 ies: dark haloes and modified dynamics”. In: *Monthly Notices of the Royal Astronomical So-*  
 1059 *ciety* 249.3 (Apr. 1991), pp. 523–537. ISSN: 0035-8711. doi: [10.1093/mnras/249.3.523](https://doi.org/10.1093/mnras/249.3.523).  
 1060 eprint: <https://academic.oup.com/mnras/article-pdf/249/3/523/18160929/mnras249-0523.pdf>. URL: <https://doi.org/10.1093/mnras/249.3.523>.
- 1062 [8] *Different types of gravitational lenses*. website. Feb. 2004. URL: <https://esahubble.org/images/heic0404b/>.
- 1064 [9] Douglas Clowe et al. “A Direct Empirical Proof of the Existence of Dark Matter”. In: *apjl*  
 1065 648.2 (Sept. 2006), pp. L109–L113. doi: [10.1086/508162](https://doi.org/10.1086/508162). arXiv: [astro-ph/0608407](https://arxiv.org/abs/astro-ph/0608407)  
 1066 [[astro-ph](https://arxiv.org/abs/astro-ph/0608407)].
- 1067 [10] Planck Collaboration and N. et. al. Aghanim. “Planck 2018 results I. Overview and the  
 1068 cosmological legacy of Planck”. In: *A&A* 641 (2020). doi: [10.1051/0004-6361/201833880](https://doi.org/10.1051/0004-6361/201833880). URL: <https://doi.org/10.1051/0004-6361/201833880>.
- 1070 [11] Wayne Hu. *Matter Density Animation*. web. 2024. URL: <http://background.uchicago.edu/~whu/animbut/anim2.html>.

- 1072 [12] Wenlong Yuan et al. “A First Look at Cepheids in a Type Ia Supernova Host with JWST”. in:  
1073 *The Astrophysical Journal Letters* 940.1 (Nov. 2022). doi: [10.3847/2041-8213/ac9b27](https://doi.org/10.3847/2041-8213/ac9b27).  
1074 URL: <https://dx.doi.org/10.3847/2041-8213/ac9b27>.
- 1075 [13] Wendy L. Freedman. “Measurements of the Hubble Constant: Tensions in Perspective”. In:  
1076 *The Astrophysical Journal* 919.1 (Sept. 2021), p. 16. doi: [10.3847/1538-4357/ac0e95](https://doi.org/10.3847/1538-4357/ac0e95).  
1077 URL: <https://dx.doi.org/10.3847/1538-4357/ac0e95>.
- 1078 [14] Jodi Cooley. “Dark Matter direct detection of classical WIMPs”. In: *SciPost Phys. Lect.  
1079 Notes* (2022), p. 55. doi: [10.21468/SciPostPhysLectNotes.55](https://doi.org/10.21468/SciPostPhysLectNotes.55). URL: <https://scipost.org/10.21468/SciPostPhysLectNotes.55>.
- 1080  
1081 [15] “Search for new phenomena in events with an energetic jet and missing transverse momentum  
1082 in  $pp$  collisions at  $\sqrt{s} = 13$  TeV with the ATLAS detector”. In: *Phys. Rev. D* 103  
1083 (11 July 2021), p. 112006. doi: [10.1103/PhysRevD.103.112006](https://doi.org/10.1103/PhysRevD.103.112006). URL: <https://link.aps.org/doi/10.1103/PhysRevD.103.112006>.
- 1084  
1085 [16] *Jetting into the dark side: a precision search for dark matter*. website. July 2020. URL:  
1086 <https://atlas.cern/updates/briefing/precision-search-dark-matter>.
- 1087 [17] Celine Armand et. al. “Combined dark matter searches towards dwarf spheroidal galaxies  
1088 with Fermi-LAT, HAWC, H.E.S.S., MAGIC, and VERITAS”. in: *Proceedings of Science*.  
1089 Vol. 395. Mar. 2022. doi: <https://doi.org/10.22323/1.395.0528>.
- 1090 [18] Tracy R. Slatyer. “Les Houches Lectures on Indirect Detection of Dark Matter”. In: *SciPost  
1091 Phys. Lect. Notes* (2022), p. 53. doi: [10.21468/SciPostPhysLectNotes.53](https://doi.org/10.21468/SciPostPhysLectNotes.53). URL:  
1092 <https://scipost.org/10.21468/SciPostPhysLectNotes.53>.
- 1093 [19] Christian W Bauer, Nicholas L. Rodd, and Bryan R. Webber. “Dark matter spectra from  
1094 the electroweak to the Planck scale”. In: *Journal of High Energy Physics* 2021.1029-8479  
1095 (June 2021). doi: [https://doi.org/10.1007/JHEP06\(2021\)121](https://doi.org/10.1007/JHEP06(2021)121).
- 1096 [20] Riccardo Catena and Piero Ullio. “A novel determination of the local dark matter density”.  
1097 In: *Journal of Cosmology and Astroparticle Physics* 2010.08 (Aug. 2010), p. 004. doi:  
1098 [10.1088/1475-7516/2010/08/004](https://doi.org/10.1088/1475-7516/2010/08/004). URL: <https://dx.doi.org/10.1088/1475-7516/2010/08/004>.
- 1099  
1100 [21] B. P. Abbott et al. “Observation of Gravitational Waves from a Binary Black Hole Merger”.  
1101 In: *Phys. Rev. Lett.* 116 (6 Feb. 2016), p. 061102. doi: [10.1103/PhysRevLett.116.061102](https://doi.org/10.1103/PhysRevLett.116.061102). URL: <https://link.aps.org/doi/10.1103/PhysRevLett.116.061102>.
- 1102  
1103 [22] R. Abbasi et. al. “Observation of high-energy neutrinos from the Galactic plane”. In: *Science*  
1104 380.6652 (June 2023), pp. 1338–1343.
- 1105 [23] NASA Goddard Space Flight Center. *Fermi’s 12-year view of the gamma-ray sky*. website.

- 1106 2022. URL: <https://svs.gsfc.nasa.gov/14090>.
- 1107 [24] Marco Cirelli et al. “PPPC 4 DM ID: a poor particle physicist cookbook for dark matter  
1108 indirect detection”. In: *Journal of Cosmology and Astroparticle Physics* 2011.03 (Mar.  
1109 2011), p. 051. doi: [10.1088/1475-7516/2011/03/051](https://doi.org/10.1088/1475-7516/2011/03/051). URL: <https://dx.doi.org/10.1088/1475-7516/2011/03/051>.
- 1111 [25] W. B. Atwood et al. “The Large Area Telescope on the Fermi Gamma-Ray Space Telescope  
1112 Mission”. In: *apj* 697.2 (June 2009), pp. 1071–1102. doi: [10.1088/0004-637X/697/2/1071](https://doi.org/10.1088/0004-637X/697/2/1071). arXiv: [0902.1089 \[astro-ph.IM\]](https://arxiv.org/abs/0902.1089).
- 1114 [26] M. Ackermann et al. “Searching for Dark Matter Annihilation from Milky Way Dwarf  
1115 Spheroidal Galaxies with Six Years of Fermi Large Area Telescope Data”. In: *prl* 115.23,  
1116 231301 (Dec. 2015), p. 231301. doi: [10.1103/PhysRevLett.115.231301](https://doi.org/10.1103/PhysRevLett.115.231301). arXiv:  
1117 [1503.02641 \[astro-ph.HE\]](https://arxiv.org/abs/1503.02641).
- 1118 [27] Mattia Di Mauro, Martin Stref, and Francesca Calore. “Investigating the effect of Milky  
1119 Way dwarf spheroidal galaxies extension on dark matter searches with Fermi-LAT data”.  
1120 In: *Phys. Rev. D* 106 (12 Dec. 2022), p. 123032. doi: [10.1103/PhysRevD.106.123032](https://doi.org/10.1103/PhysRevD.106.123032).  
1121 URL: <https://link.aps.org/doi/10.1103/PhysRevD.106.123032>.
- 1122 [28] F. et al. Aharonian. “Observations of the Crab Nebula with H.E.S.S.”. In: *Astron. Astrophys.*  
1123 457 (2006), pp. 899–915. doi: [10.1051/0004-6361:20065351](https://doi.org/10.1051/0004-6361:20065351). arXiv: [astro-ph/0607333](https://arxiv.org/abs/astro-ph/0607333).
- 1125 [29] J. Albert et al. “VHE  $\gamma$ -Ray Observation of the Crab Nebula and its Pulsar with the MAGIC  
1126 Telescope”. In: *The Astrophysical Journal* 674.2 (Feb. 2008), p. 1037. doi: [10.1086/525270](https://doi.org/10.1086/525270). URL: <https://dx.doi.org/10.1086/525270>.
- 1128 [30] N. Park. “Performance of the VERITAS experiment”. In: *Proceedings, 34th International  
1129 Cosmic Ray Conference (ICRC2015): The Hague, The Netherlands, July, 30th July - 6th  
1130 August*. Vol. 34. 2015, p. 771. arXiv: [1508.07070 \[astro-ph.IM\]](https://arxiv.org/abs/1508.07070).
- 1131 [31] A. Abramowski et al. “H.E.S.S. constraints on Dark Matter annihilations towards the Sculptor  
1132 and Carina Dwarf Galaxies”. In: *Astropart. Phys.* 34 (2011), pp. 608–616. doi: [10.1016/j.astropartphys.2010.12.006](https://doi.org/10.1016/j.astropartphys.2010.12.006). arXiv: [1012.5602 \[astro-ph.HE\]](https://arxiv.org/abs/1012.5602).
- 1134 [32] A. Abramowski et al. “Search for dark matter annihilation signatures in H.E.S.S. observations  
1135 of Dwarf Spheroidal Galaxies”. In: *Phys. Rev. D* 90 (2014), p. 112012. doi: [10.1103/PhysRevD.90.112012](https://doi.org/10.1103/PhysRevD.90.112012). arXiv: [1410.2589 \[astro-ph.HE\]](https://arxiv.org/abs/1410.2589).
- 1137 [33] H. Abdalla et al. “Searches for gamma-ray lines and ‘pure WIMP’ spectra from Dark  
1138 Matter annihilations in dwarf galaxies with H.E.S.S”. in: *JCAP* 11 (2018), p. 037. doi:  
1139 [10.1088/1475-7516/2018/11/037](https://doi.org/10.1088/1475-7516/2018/11/037). arXiv: [1810.00995 \[astro-ph.HE\]](https://arxiv.org/abs/1810.00995).

- 1140 [34] J. Aleksić et al. “Optimized dark matter searches in deep observations of Segue 1 with  
1141 MAGIC”. in: *JCAP* 1402 (2014), p. 008. doi: [10.1088/1475-7516/2014/02/008](https://doi.org/10.1088/1475-7516/2014/02/008).  
1142 arXiv: [1312.1535 \[hep-ph\]](https://arxiv.org/abs/1312.1535).
- 1143 [35] V.A. Acciari et al. “Combined searches for dark matter in dwarf spheroidal galaxies observed  
1144 with the MAGIC telescopes, including new data from Coma Berenices and Draco”. In: *Physics of the Dark Universe* (2021), p. 100912. ISSN: 2212-6864. doi: <https://doi.org/10.1016/j.dark.2021.100912>. URL: <https://www.sciencedirect.com/science/article/pii/S2212686421001370>.
- 1148 [36] M. L. Ahnen et al. “Indirect dark matter searches in the dwarf satellite galaxy Ursa Major II  
1149 with the MAGIC Telescopes”. In: *JCAP* 1803.03 (2018), p. 009. doi: [10.1088/1475-7516/2018/03/009](https://doi.org/10.1088/1475-7516/2018/03/009). arXiv: [1712.03095 \[astro-ph.HE\]](https://arxiv.org/abs/1712.03095).
- 1151 [37] S. et al. Archambault. “Dark matter constraints from a joint analysis of dwarf Spheroidal  
1152 galaxy observations with VERITAS”. in: *prd* 95.8 (Apr. 2017). doi: [10.1103/PhysRevD.95.082001](https://doi.org/10.1103/PhysRevD.95.082001). arXiv: [1703.04937 \[astro-ph.HE\]](https://arxiv.org/abs/1703.04937).
- 1154 [38] Louise Oakes et al. “Combined Dark Matter searches towards dwarf spheroidal galaxies with  
1155 Fermi-LAT, HAWC, HESS, MAGIC and VERITAS”. in: *Proceedings of Science*. 2019.
- 1156 [39] Celine Armand et al. on behalf of the Fermi-LAT, HAWC, HESS, MAGIC, VERITAS.  
1157 “Combined Dark Matter searches towards dwarf spheroidal galaxies with Fermi-LAT,  
1158 HAWC, HESS, MAGIC and VERITAS”. in: *Proceedings of Science*. 2021.
- 1159 [40] Daniel Kerszberg et al. on behalf of the Fermi-LAT, HAWC, HESS, MAGIC, and VER-  
1160 TIAS collaborations. “Search for dark matter annihilation with a combined analysis of  
1161 dwarf spheroidal galaxies from Fermi-LAT, HAWC, H.E.S.S., MAGIC and VERITAS”. in:  
1162 *Proceedings of Science*. 2023.
- 1163 [41] A. U. Abeysekara et al. “Observation of the Crab Nebula with the HAWC Gamma-Ray  
1164 Observatory”. In: *The Astrophysical Journal* 843.1 (June 2017), p. 39. doi: [10.3847/1538-4357/aa7555](https://doi.org/10.3847/1538-4357/aa7555). URL: <https://doi.org/10.3847/1538-4357/aa7555>.
- 1166 [42] Giacomo Vianello et al. *The Multi-Mission Maximum Likelihood framework (3ML)*. 2015.  
1167 arXiv: [1507.08343 \[astro-ph.HE\]](https://arxiv.org/abs/1507.08343).
- 1168 [43] Marco Cirelli et al. “PPPC 4 DM ID: a poor particle physicist cookbook for dark matter  
1169 indirect detection”. In: *Journal of Cosmology and Astroparticle Physics* 2011.03 (Mar.  
1170 2011). ISSN: 1475-7516. doi: [10.1088/1475-7516/2011/03/051](https://doi.org/10.1088/1475-7516/2011/03/051). URL: <http://dx.doi.org/10.1088/1475-7516/2011/03/051>.
- 1172 [44] Alex Geringer-Sameth, Savvas M. Koushiappas, and Matthew Walker. “DWARF GALAXY  
1173 ANNIHILATION AND DECAY EMISSION PROFILES FOR DARK MATTER EXPERI-  
1174 MENTS”. in: *The Astrophysical Journal* 801.2 (Mar. 2015), p. 74. ISSN: 1538-4357. doi:

- 1175        10.1088/0004-637x/801/2/74. URL: <http://dx.doi.org/10.1088/0004-637X/80>  
1176        1/2/74.
- 1177 [45] A. Albert et al. “Dark Matter Limits from Dwarf Spheroidal Galaxies with the HAWC  
1178 Gamma-Ray Observatory”. In: *The Astrophysical Journal* 853.2 (Feb. 2018), p. 154. ISSN:  
1179 1538-4357. doi: 10.3847/1538-4357/aaa6d8. URL: <http://dx.doi.org/10.3847/1538-4357/aaa6d8>.
- 1181 [46] V. Bonnivard et al. “Spherical Jeans analysis for dark matter indirect detection in dwarf  
1182 spheroidal galaxies - Impact of physical parameters and triaxiality”. In: *Mon. Not. Roy.  
1183 Astron. Soc.* 446 (2015), pp. 3002–3021. doi: 10.1093/mnras/stu2296. arXiv:  
1184 1407.7822 [astro-ph.HE].
- 1185 [47] M. Ackermann et al. “Searching for Dark Matter Annihilation from Milky Way Dwarf  
1186 Spheroidal Galaxies with Six Years of Fermi Large Area Telescope Data”. In: *prl* 115.23,  
1187 231301 (Dec. 2015), p. 231301. doi: 10.1103/PhysRevLett.115.231301. arXiv:  
1188 1503.02641 [astro-ph.HE].
- 1189 [48] M. L. Ahnen et al. “Limits to Dark Matter Annihilation Cross-Section from a Combined  
1190 Analysis of MAGIC and Fermi-LAT Observations of Dwarf Satellite Galaxies”. In: *JCAP*  
1191 1602.02 (2016), p. 039. doi: 10.1088/1475-7516/2016/02/039. arXiv: 1601.06590  
1192 [astro-ph.HE].
- 1193 [49] Alex Geringer-Sameth and Matthew Koushiappas Savvas M. and Walker. “Dwarf galaxy  
1194 annihilation and decay emission profiles for dark matter experiments”. In: *Astrophys.  
1195 J.* 801.2 (2015), p. 74. doi: 10.1088/0004-637X/801/2/74. arXiv: 1408.0002  
1196 [astro-ph.CO].
- 1197 [50] A. et al. Albert. “Searching for Dark Matter Annihilation in Recently Discovered Milky Way  
1198 Satellites with Fermi-LAT”. in: *Astrophys. J.* 834.2 (2017), p. 110. doi: 10.3847/1538-4  
1199 357/834/2/110. arXiv: 1611.03184 [astro-ph.HE].
- 1200 [51] Mattia Di Mauro and Martin Wolfgang Winkler. “Multimessenger constraints on the dark  
1201 matter interpretation of the Fermi-LAT Galactic Center excess”. In: *prd* 103.12, 123005  
1202 (June 2021), p. 123005. doi: 10.1103/PhysRevD.103.123005. arXiv: 2101.11027  
1203 [astro-ph.HE].
- 1204 [52] V. Bonnivard et al. “Dark matter annihilation and decay in dwarf spheroidal galaxies: The  
1205 classical and ultrafaint dSphs”. In: *Mon. Not. Roy. Astron. Soc.* 453.1 (2015), pp. 849–867.  
1206 doi: 10.1093/mnras/stv1601. arXiv: 1504.02048 [astro-ph.HE].
- 1207 [53] Gianfranco Bertone, Dan Hooper, and Joseph Silk. “Particle dark matter: evidence, can-  
1208 didates and constraints”. In: *Physics Reports* 405.5-6 (Jan. 2005), pp. 279–390. ISSN:  
1209 0370-1573. doi: 10.1016/j.physrep.2004.08.031. URL: <http://dx.doi.org/10.1016/j.physrep.2004.08.031>.

- 1211 [54] HongSheng Zhao. “Analytical models for galactic nuclei”. In: *Mon. Not. Roy. Astron. Soc.*  
1212 278 (1996), pp. 488–496. doi: [10.1093/mnras/278.2.488](https://doi.org/10.1093/mnras/278.2.488). arXiv: [astro-ph/9509122](https://arxiv.org/abs/astro-ph/9509122)  
1213 [[astro-ph](#)].
- 1214 [55] H. C. Plummer. “On the Problem of Distribution in Globular Star Clusters: (Plate 8.)”  
1215 In: *Monthly Notices of the Royal Astronomical Society* 71.5 (Mar. 1911), pp. 460–470.  
1216 ISSN: 0035-8711. doi: [10.1093/mnras/71.5.460](https://doi.org/10.1093/mnras/71.5.460). eprint: <https://academic.oup.com/mnras/article-pdf/71/5/460/2937497/mnras71-0460.pdf>. URL:  
1217 <https://doi.org/10.1093/mnras/71.5.460>.
- 1219 [56] Daniel R. Hunter. “Derivation of the anisotropy profile, constraints on the local velocity  
1220 dispersion, and implications for direct detection”. In: *JCAP* 02 (2014), p. 023. doi:  
1221 [10.1088/1475-7516/2014/02/023](https://doi.org/10.1088/1475-7516/2014/02/023). arXiv: [1311.0256](https://arxiv.org/abs/1311.0256) [[astro-ph.CO](#)].
- 1222 [57] Barun Kumar Dhar and Liliya L. R. Williams. “Surface mass density of the Einasto family  
1223 of dark matter haloes: are they Sersic-like?” In: *Mon. Not. Roy. Astron. Soc.* (2010). doi:  
1224 [10.1111/j.1365-2966.2010.16446.x](https://doi.org/10.1111/j.1365-2966.2010.16446.x).
- 1225 [58] M. Baes and E. Van Hese. “Dynamical models with a general anisotropy profile”. In:  
1226 *Astron. Astrophys.* 471 (2007), p. 419. doi: [10.1051/0004-6361:20077672](https://doi.org/10.1051/0004-6361:20077672). arXiv:  
1227 [0705.4109](https://arxiv.org/abs/0705.4109) [[astro-ph](#)].
- 1228 [59] Matthew G. Walker, Edward W. Olszewski, and Mario Mateo. “Bayesian analysis of re-  
1229 solved stellar spectra: application to MMT/Hectochelle observations of the Draco dwarf  
1230 spheroidal”. In: *mnras* 448.3 (Apr. 2015), pp. 2717–2732. doi: [10.1093/mnras/stv099](https://doi.org/10.1093/mnras/stv099).  
1231 arXiv: [1503.02589](https://arxiv.org/abs/1503.02589) [[astro-ph.GA](#)].